

# Biomechanical Modeling and Failure Analysis in Total Knee Replacement:

Development and Implementation of  
the Isotropic Crushable Foam Model



Navid Soltanihafshejani

**RADBOD  
UNIVERSITY  
PRESS**

Radboud  
Dissertation  
Series

# **Biomechanical Modeling and Failure Analysis in Total Knee Replacement: Development and Implementation of the Isotropic Crushable Foam Model**

Navid Soltanihafshejani

**Biomechanical Modeling and Failure Analysis in Total Knee Replacement:  
Development and Implementation of the Isotropic Crushable Foam Model**

Navid Soltanihafshejani

**Radboud Dissertation Series**

ISSN: 2950-2772 (Online); 2950-2780 (Print)

Published by RADBOUD UNIVERSITY PRESS

Postbus 9100, 6500 HA Nijmegen, The Netherlands

[www.radbouduniversitypress.nl](http://www.radbouduniversitypress.nl)

Design: Proefschrift AIO | Annelies Lips

Cover: Navid Soltanihafshejani & Somayeh Rabbani Arshad

Printing: DPN Rikken/Pumbo

ISBN: 9789465150833

DOI: 10.54195/9789465150833

Free download at: <https://doi.org/10.54195/9789465150833>

© 2025 Navid Soltanihafshejani

**RADBOUD  
UNIVERSITY  
PRESS**

This is an Open Access book published under the terms of Creative Commons Attribution-Noncommercial-NoDerivatives International license (CC BY-NC-ND 4.0). This license allows reusers to copy and distribute the material in any medium or format in unadapted form only, for noncommercial purposes only, and only so long as attribution is given to the creator, see <http://creativecommons.org/licenses/by-nc-nd/4.0/>.

# **Biomechanical Modeling and Failure Analysis in Total Knee Replacement: Development and Implementation of the Isotropic Crushable Foam Model**

Proefschrift ter verkrijging van de graad van doctor  
aan de Radboud Universiteit Nijmegen  
op gezag van de rector magnificus prof. dr. J.M. Sanders,  
volgens besluit van het college voor promoties  
in het openbaar te verdedigen op

vrijdag 4 juli 2025  
om 10.30 uur precies

door

**Navid Soltanihafshejani**

geboren op 28 maart 1991  
te Shahrekord, Iran

**Promotor:**

Prof. dr. ir. N.J.J. Verdonschot

**Copromotor:**

Dr. D.W. Janssen

**Manuscriptcommissie:**

Prof. dr. N.L.W. Keijsers

Prof. dr. ir. A.H. van den Boogaard (Universiteit Twente)

Dr. ir. B. van Rietbergen (Technische Universiteit Eindhoven)

# **Biomechanical Modeling and Failure Analysis in Total Knee Replacement: Development and Implementation of the Isotropic Crushable Foam Model**

Dissertation to obtain the degree of doctor  
from Radboud University Nijmegen  
on the authority of the Rector Magnificus prof. dr. J.M. Sanders,  
according to the decision of the Doctorate Board  
to be defended in public on

Friday, July 4, 2025  
at 10:30 am

by

**Navid Soltanihafshejani**

born on March 28, 1991  
in Shahrekord, Iran

**PhD supervisor:**

Prof. dr. ir. N.J.J. Verdonshot

**PhD co-supervisor:**

Dr. D.W. Janssen

**Manuscript Committee:**

Prof. dr. N.L.W. Keijsers

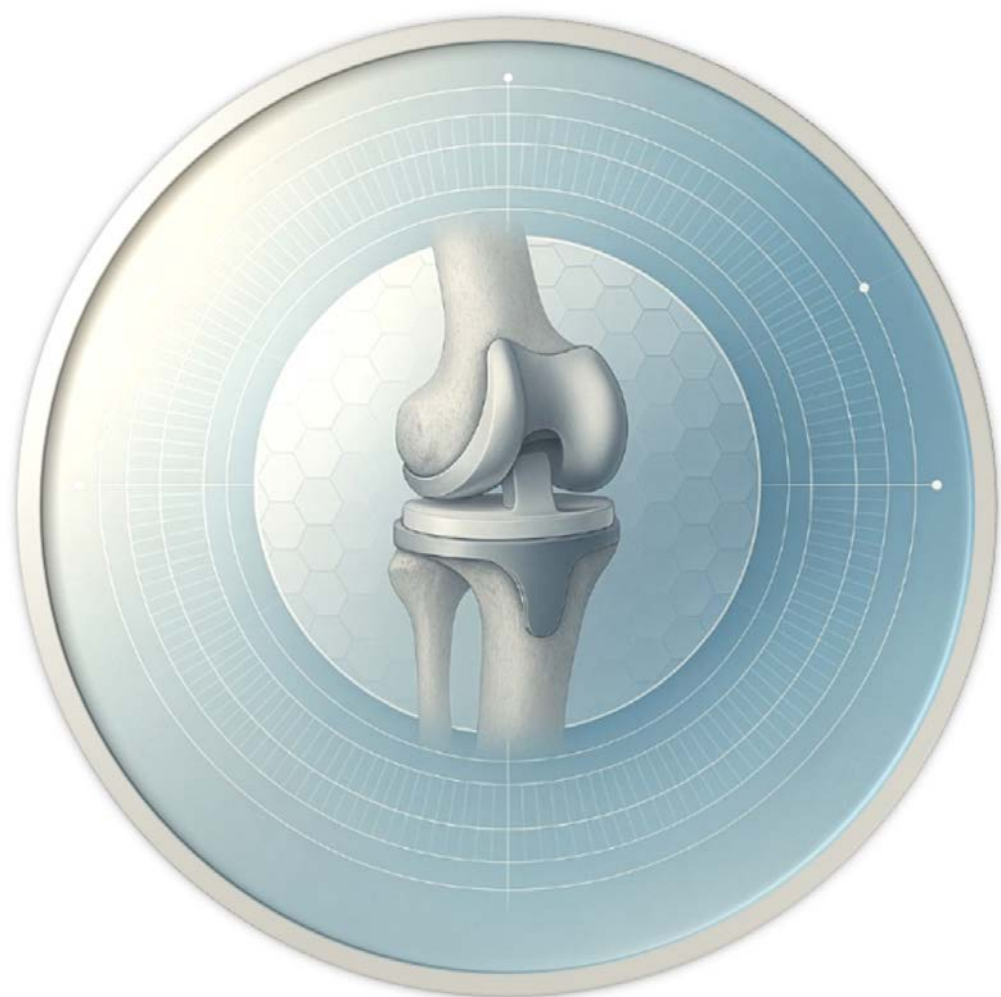
Prof. dr. ir. A.H. van den Boogaard (Twente University)

Dr. ir. B. van Rietbergen (Eindhoven University of Technology)

## Table of contents

<b>Chapter 1</b>	General Introduction	9
<b>Chapter 2</b>	Development of a Crushable Foam Model for Human Trabecular Bone	21
<b>Chapter 3</b>	The Application of an Isotropic Crushable Foam Model to Predict the Femoral Fracture Risk	49
<b>Chapter 4</b>	The Effect of Bone Plasticity Models on Simulations of Primary Fixation in Total Knee Arthroplasty	71
<b>Chapter 5</b>	The Effect of Periprosthetic Bone Loss on The Failure Risk of Tibial Total Knee Arthroplasty	101
<b>Chapter 6</b>	General Discussion	119
<b>Chapter 7</b>	Summary	133
<b>Chapter 8</b>	Samenvatting	141
<b>Chapter 9</b>	خلاصه	149
<b>Chapter 10</b>	Acknowledgments	158
	PhD portfolio	162
	List of publications	164
	Curriculum Vitae	166





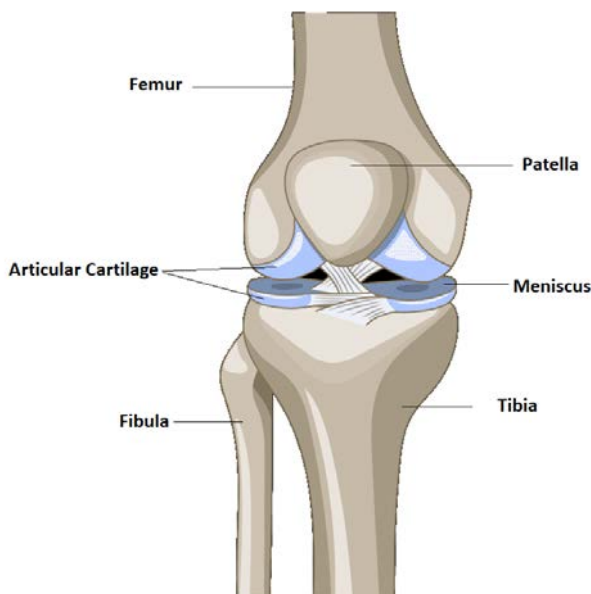
## Chapter 1

# General Introduction

---

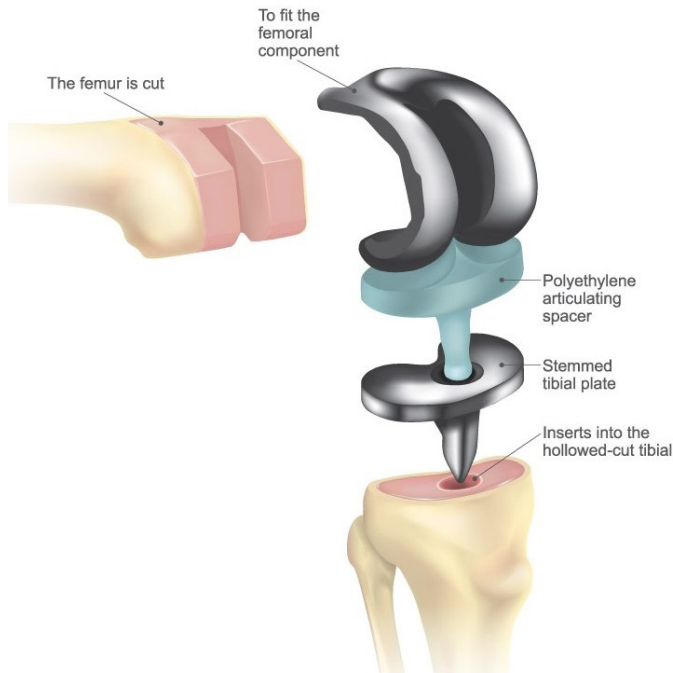
## Introduction

The knee is a synovial joint that is composed of three bony structures with two articulations: the tibiofemoral (TF) joint (articulation between the femur and tibia), and the patellofemoral (PF) joint (the articulation between the patella and the femur). The main degrees of freedom of the TF joint consist of three rotations (flexion-extension, internal-external rotation, varus-valgus rotation) and two translations (anteroposterior and mediolateral). The primary biomechanical roles of the knee joint are to facilitate motion with minimal energy requirements from the muscles while maintaining stability, and to transmit, absorb, and redistribute loads across the joint during daily activities [1]. Due to its distal location and the influence of muscles around the joint, the tibiofemoral joint is subject to large compressive loads, reaching up to 2-3 times body weight during walking and up to 4-7 times the body weight during activities such as running, or stairs ascent, and even greater loads during unexpected events like falling or jumping [2, 3]. The TF joint allows for up to 160° of flexion (rotation in the sagittal plane), with coupled rotations in the other two planes. The PF joint, on the other hand, involving the articulation between the patella and the femur, primarily facilitates the knee's extension mechanism and plays a crucial role in weight bearing activities like climbing stairs. It enhances the leverage of the quadriceps muscle, significantly reducing the force required from the muscle for knee extension [2, 3].



**Figure 1-1** An intact Knee

The function of the knee relies on the coordinated interaction of bones, ligaments, cartilage and other tissues such as tendons, muscles and meniscus. The femur, tibia, and patella articulate with support from articular cartilage, enabling smooth movement and absorbing mechanical stresses [4]. The articular cartilage, with its ability to minimize friction and absorb shocks, is crucial for joint functioning. However, osteoarthritis often leads to progressive cartilage degeneration, resulting in pain, stiffness, and compromised functionality. Although various factors contribute to the development of osteoarthritis, such as age, genetics, improper loading and joint instability, the consequences are universally impactful, leading to a reduced quality of life for those affected [5]. While there is currently no cure for osteoarthritis, a range of treatments, spanning from conservative measures like physical therapy and medication to surgical interventions such as joint replacement, aims to alleviate symptoms and enhance joint function [5].



**Figure 1-2** TKA and its component

Total knee arthroplasty (TKA) is a common intervention for patients with advanced knee osteoarthritis (OA) or rheumatoid arthritis. The primary objectives of TKA are to mitigate pain and restore normal knee function and kinematics [6]. The surgical procedure involves the replacement of the damaged knee surfaces of the

distal femur and proximal tibia with prosthetic femoral and tibial components, respectively. The prosthetic components used in TKA are made of metals, ceramics, and polymers that are biocompatible and can withstand the mechanical forces acting on the knee joint. The femoral and tibial components are fixed to the respective bones with bone cement (cemented TKA) or using a press-fit fixation (cementless TKA), depending on the surgeon's preference and the patient's bone quality [7]. The new knee joint is formed by a metal (mainly CoCr) or ceramic femoral component articulating against a plastic tibial insert placed on a metal (mainly Ti-alloy) tibial component. The plastic tibial insert is usually made of ultra-high molecular weight polyethylene (UHMWPE), which is known for its high wear resistance and biocompatibility [6, 7].

Although TKA is a highly effective procedure, it does not provide a life-long solution for all patients. Patients may experience complications including infection, dislocation, or implant loosening, which may ultimately lead to implant failure and revision surgery [8]. Since the failure process is often accompanied by significant bone loss in the peri-prosthetic regions, revision TKA is a complicated procedure [9, 10]. Thorough planning is required to restore the functionality and stability of the knee.

The etiology of TKA failure has been extensively studied, and aseptic loosening has been identified as one of the primary reasons for revision TKA in the literature [9, 10]. Various theories have been proposed to explain the underlying causes of aseptic loosening [9, 10], and it is widely accepted that implant fixation method plays a critical role in cases of aseptic loosening of the implant [10-12]. Despite the advantages and disadvantages of each fixation method, the risk of TKA failure can be significantly influenced by the quality of implantation which involves precise surgical techniques, accurate sizing and fitting of prosthetic components, and consideration of the patient's bone quality [8, 11]. The cemented TKA method, which uses polymethylmethacrylate (PMMA) or bone cement [8], is known for its immediate fixation, making it a reliable choice for older patients with poorer bone quality. On the other hand, cementless TKA relies on bone growth into a porous surface of the prosthesis for fixation, potentially leading to a more natural bone-prosthesis interface. This technique, often preferred for younger, more active patients with good bone quality, may offer better long-term implant integration but requires a longer time of osseointegration to obtain reliable fixation to the bone [13, 14].

The mechanics of failure in TKA differ between cemented and cementless fixation methods. In cemented TKA, loosening happens when the bond between the bone (or implant) and the cement deteriorates over time, potentially due to wear and tear or biological factors that affect the bone-cement interface. For cementless TKA, the failure process is different, as cementless fixation relies on bone ingrowth into the porous surface of the prosthesis for stability [9, 10]. Failure of cementless TKA occurs when there is inadequate bone growth into the prosthesis, which can lead to instability and loosening. This situation may arise due to factors like poor bone quality, incorrect implant sizing or placement, or the patient's biological response to the implant. While the underlying mechanics of failure may differ between the two methods, the overall risk of requiring a revision surgery is similar for both [13, 14]. In the clinical setting, TKA failure is assessed in clinical evaluations and radiographic analyses.

To evaluate implant fixation in the pre-clinical phase, various biomechanical methods, including physical testing of implants and reconstructions using synthetic or cadaveric bone specimens, have been proposed to ensure that only safe designs are approved for clinical use. In addition, computational analyses, such as Finite Element Analysis (FEA) offering a non-invasive, cost-effective, and highly detailed approach to understanding the biomechanics of knee implant fixation [15]. By simulating the complex interactions between the implant and surrounding tissues, researchers can predict the impact of different design and placement strategies on TKA longevity and performance. These advanced models, tailored to individual patient anatomy and movement, allow for a personalized assessment of implant behavior, identifying potential failure modes such as loosening or malalignment [15]. Additionally, computational modeling aids in testing new designs under varied conditions, reducing dependence on physical prototypes and clinical trials. Thus, computer simulation has a large potential to contribute to assess the biomechanical behavior of TKA reconstruction.

In predicting the long-term success and primary fixation of TKA, several factors emerge as central to understanding and forecasting outcomes which out of this three can be evaluated effectively using computational modelling: the effect of quality of the bone surrounding the implant, the biomechanical loading conditions during activities, and the interactions between the implant materials and bone tissue [16-19]. Firstly, the bone quality is crucial because variations in bone mineral density and structural integrity can significantly affect the mechanical stability and the risk of implant failure. Computational models allow for the simulation of bone behavior under varying conditions, thus providing insights into how weakened

bone may compromise implant integrity in crucial situation such as medial tibial collapse [16, 20]. Secondly, biomechanical loading conditions, which vary widely across daily and exceptional activities, directly influence the stress distribution and potential wear patterns on both the implant and the bone. Computational modeling enables the detailed analysis of these load conditions and their long-term impact on TKA outcomes [17, 20]. Lastly, the interaction between the implant materials and bone tissue involves complex biomechanical and biochemical processes that affect osseointegration and implant longevity. Using computational models, researchers can explore various material properties and their interactions with biological tissues, which are difficult to replicate in experimental settings.

For optimal FEA results, it is crucial to accurately incorporate realistic bone mechanics by developing and applying appropriate material models. Bone mechanics provide essential insights into the mechanical properties of bones, such as strength, elasticity, and resistance to fracture [21]. These properties are pivotal in determining how bones react to forces and stresses and how bone interacts with orthopedic implant. By incorporating detailed and realistic material models, FEA can simulate bone response with high fidelity, allowing for predictions of bone deformation, stress distribution, and potential failure points [22]. This level of detail is crucial for developing effective medical treatments, understanding pathological conditions, and designing implants and prosthetics that interact harmoniously with the human skeletal system. Thus, the integration of accurate bone mechanics and sophisticated material models in FEA is fundamental in advancing biomedical engineering, improving patient care, and enhancing the understanding of human biomechanics [15, 22].

To accurately predict mechanical failure of TKA reconstructions, an appropriate material model must be incorporated that replicates the nonlinear response of both trabecular and cortical bone [15, 23] [24, 25]. While the cortical bone response can be simulated quite realistically using elastoplastic material models [25], trabecular bone exhibits a more complex nonlinear behavior due to its cellular structure. It is therefore more challenging to simulate failure processes in trabecular bone in computational modeling, as it requires a quite sophisticated material model [26]. Consequently, there is a need for a material model that can effectively capture the combined interaction of cortical and trabecular bone. Research has demonstrated that pressure-dependent material models, such as the Isotropic Crushable Foam (ICF) or the Drucker-Prager model, may offer an improved representation of the mechanical response compared to elastoplastic models like softening von-Mises [22, 27]. However, accurately defining the actual bone properties within each material model poses a significant challenge.

In the context of TKA, employing a pressure-dependent material model is particularly advantageous due to its ability to realistically represent the bio-mechanical behavior of bone within the semi-confined environment of the knee, where cortical bone surrounds softer trabecular bone. Unlike simpler elastoplastic models, pressure-dependent models adjust their responses based on varying pressures and stresses, thereby providing more accurate simulations of the complex stress profiles experienced by trabecular bone under different loading conditions. This capability is crucial for predicting the mechanical interlock and stability of the implant immediately post-surgery and for assessing the long-term integrity and adaptation of the bone-implant interface, enhancing both immediate outcomes and the longevity of the implant. Thus, pressure-dependent models may offer significant improvements in patient-specific predictions in TKA.

This thesis aims to develop a pressure-dependent material model for accurately representing human bone response and evaluating mechanical interactions in TKA failure. The overarching goal is to provide a realistic examination of long-term outcomes and primary fixation. The dissertation is structured into four main parts to answer the following research questions (RQ's):

1. *How can the isotropic crushable foam model be characterized to improve the prediction of bone failure in orthopedic applications?*
2. *Does the isotropic crushable foam model improve the prediction of human bone mechanical failure?*
3. *How do the mechanical properties of bone influence the initial stability of TKA implants, and how do different constitutive models impact the prediction of this stability?*
4. *How can the isotropic crushable foam model assess the impact of bone mechanical properties on the long-term failure of TKA?*

**Chapter 2** details experimental investigations that were conducted on cadaveric tibial trabecular bones to determine their mechanical properties. It outlines how failure parameters were established through two primary loading configurations: uniaxial and confined. These properties were subsequently utilized to develop and validate an ICF Model, which is dependent on bone mineral density for FEA modeling.

**Chapter 3** aims to evaluate whether an ICF model can accurately simulate the mechanical failure of bone, critical for applications such as TKA, where both tibial and femoral bones are integral. This chapter details the experimental determination



of the mechanical properties of femoral trabecular bone. It then describes the development of an ICF model tailored for femoral bone, which is further extended to simulate the response of cortical bone. Finally, the ability of the model to replicate the entire mechanics of bone failure is validated against experimental data from femoral fractures.

In **Chapter 4** the primary fixation (initial stability) of the femoral component is investigated by examining the influence of plasticity models on the micromotion predictions in TKA. The study investigated the impact of two plasticity models on capturing the mechanical response of femoral bone, utilizing experimental testing and numerical simulations.

In **Chapter 5** the developed ICF model is employed to explore the long-term implications of TKA. Specifically, the investigation focuses on assessing the impact of periprosthetic bone loss and loading conditions on the risk of tibial TKA failure. Within this study a particular failure mode in TKA, namely tibial medial collapse, is simulated, both in the situation directly post-operatively and after a longer period during which periprosthetic bone loss has occurred.

**Chapter 6** serves as a general discussion where a critical assessment is conducted, relating the thesis's aims to the results obtained. This chapter also positions the thesis within a future context, offering suggestions for further research and potential applications.

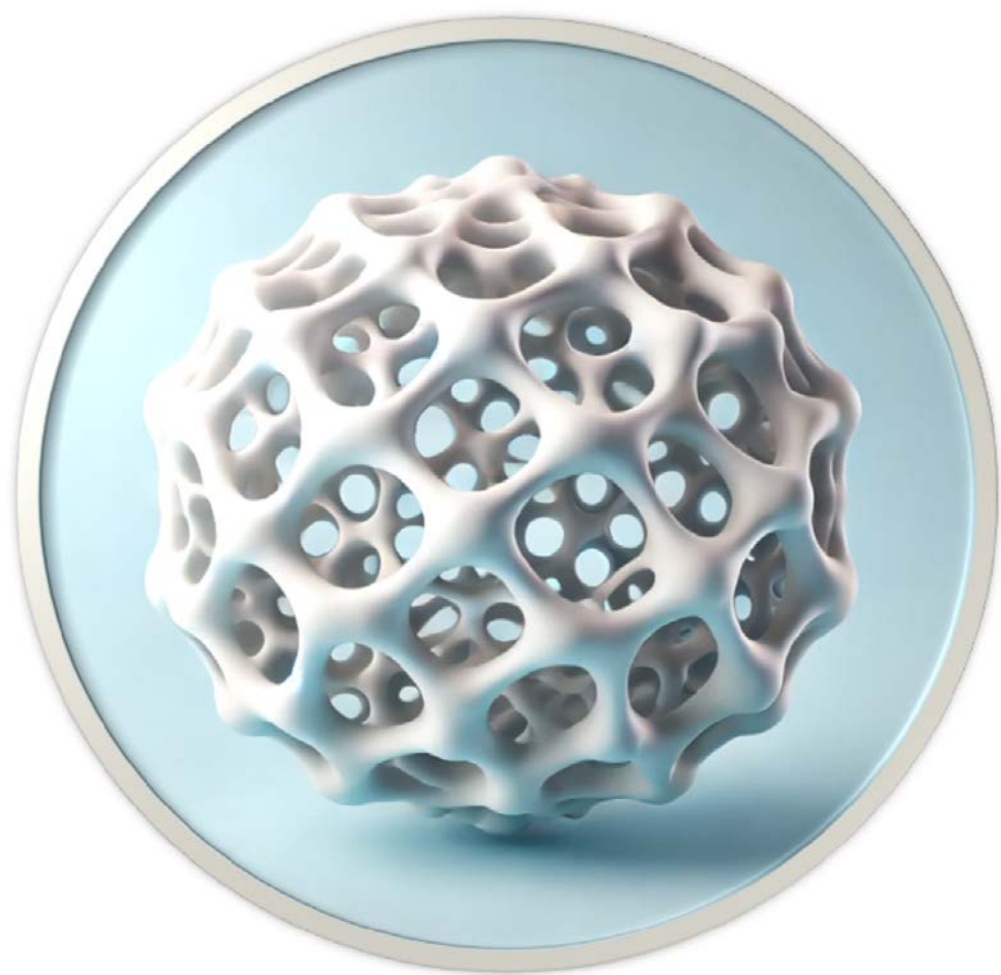
**Chapters 7 and 8** provide comprehensive English and Dutch summaries of the current thesis, respectively.

## References

1. Masouros, S., A. Bull, and A. Amis, (i) *Biomechanics of the knee joint*. Orthopaedics and Trauma, 2010. **24**(2): p. 84-91.
2. Fehring, T.K., et al., *Catastrophic varus collapse of the tibia in obese total knee arthroplasty*. The Journal of arthroplasty, 2017. **32**(5): p. 1625-1629.
3. Zimmerman, W.F., et al., *Damage in total knee replacements from mechanical overload*. Journal of biomechanics, 2016. **49**(10): p. 2068-2075.
4. Aweid, O., H. Osmani, and J. Melton, *Biomechanics of the knee*. Orthopaedics and Trauma, 2019. **33**(4): p. 224-230.
5. Thomsen, M.G., et al., *Indications for knee arthroplasty have remained consistent over time*. Dan Med J, 2012. **59**(8): p. A4492.
6. Taunton, M.J., *What's new in adult reconstructive knee surgery*. 2020, LWW. p. 91-100.
7. Varacallo, M., T.D. Luo, and N.A. Johanson, *Total knee arthroplasty techniques*. 2018.
8. Berahmani, S., *Press-fit stability of cementless femoral knee implants. A biomechanical evaluation*. 2017, [SI]: [Sn].
9. Sharkey, P.F., et al., *Why are total knee arthroplasties failing today—has anything changed after 10 years?* The Journal of arthroplasty, 2014. **29**(9): p. 1774-1778.
10. Sundfeldt, M., et al., *Aseptic loosening, not only a question of wear: a review of different theories*. Acta orthopaedica, 2006. **77**(2): p. 177-197.
11. Jones, L.C. and D.S. Hungerford, *Cement disease*. Clinical Orthopaedics and Related Research (1976-2007), 1987. **225**: p. 192-206.
12. Ryd, L. and L. Linder, *On the correlation between micromotion and histology of the bone-cement interface: report of three cases of knee arthroplasty followed by roentgen stereophotogrammetric analysis*. The Journal of arthroplasty, 1989. **4**(4): p. 303-309.
13. Papas, P.V., D. Congiusta, and F.D. Cushner, *Cementless versus cemented fixation in total knee arthroplasty*. The Journal of Knee Surgery, 2019. **32**(07): p. 596-599.
14. Prasad, A.K., et al., *Cemented vs. cementless fixation in primary total knee arthroplasty: a systematic review and meta-analysis*. EFORT open reviews, 2020. **5**(11): p. 793.
15. Herrera, A., et al., *Applications of finite element simulation in orthopedic and trauma surgery*. World journal of orthopedics, 2012. **3**(4): p. 25.
16. Graichen, H., *TKA revision—reasons, challenges and solutions*. Journal of orthopaedics, 2014. **11**(1): p. 1.
17. Nedopil, A.J., S.M. Howell, and M.L. Hull, *What mechanisms are associated with tibial component failure after kinematically-aligned total knee arthroplasty?* International Orthopaedics, 2017. **41**: p. 1561-1569.
18. TAHAROU, B., et al., *Biomechanical evaluation of bone quality effect on stresses at bone-implant interface: a finite element study*. Journal of Applied and Computational Mechanics, 2020.
19. Yang, H., et al., *Impact of patient, surgical, and implant design factors on predicted tray–bone interface micromotions in cementless total knee arthroplasty*. Journal of Orthopaedic Research®, 2023. **41**(1): p. 115-129.
20. Soltanihafshejani, N., et al., *The Effect of Periprosthetic Bone Loss on The Failure Risk of Tibial Total Knee Arthroplasty*. Journal of Orthopaedic Research®, 2023.

21. Engelke, K., B. van Rietbergen, and P. Zysset, *FEA to measure bone strength: a review*. Clinical reviews in bone and mineral metabolism, 2016. **14**: p. 26-37.
22. Soltanihafshejani, N., et al., *Development of a crushable foam model for human trabecular bone*. Medical engineering & physics, 2021. **96**: p. 53-63.
23. Soltanihafshejani, N., et al. *Experimental and Numerical Identification of Crushable Foam Model of Human Trabecular Bone*. in *Orthopaedic Proceedings*. 2021. The British Editorial Society of Bone & Joint Surgery.
24. Manske, S., et al., *Cortical and trabecular bone in the femoral neck both contribute to proximal femur failure load prediction*. Osteoporosis international, 2009. **20**(3): p. 445-453.
25. Schileo, E., et al., *Cortical bone mapping improves finite element strain prediction accuracy at the proximal femur*. Bone, 2020. **136**: p. 115348.
26. Lee, C.-S., et al., *A new constitutive model for simulation of softening, plateau, and densification phenomena for trabecular bone under compression*. Journal of the mechanical behavior of biomedical materials, 2017. **65**: p. 213-223.
27. Kelly, N., et al., *An experimental and computational investigation of the post-yield behaviour of trabecular bone during vertebral device subsidence*. Biomechanics and modeling in mechanobiology, 2013. **12**(4): p. 685-703.





## Chapter 2

# Development of a Crushable Foam Model for Human Trabecular Bone

---

Navid Soltanihafshejani<sup>a,\*</sup>, Thom Bitter<sup>a</sup>, Dennis Janssen<sup>a</sup>, Nico Verdonschot<sup>a,b</sup>

<sup>a</sup> Radboud University Medical Center, Radboud Institute for Health Sciences, Orthopaedic Research Laboratory, 6500 HB Nijmegen, the Netherlands.

<sup>b</sup> University of Twente, Laboratory for Biomechanical Engineering, Faculty of Engineering Technology, 7500 AE Enschede, the Netherlands.

*Published on October 2021 in Journal of Medical engineering and physics*

<https://doi.org/10.1016/j.medengphy.2021.08.009>

## Introduction

Trabecular bone is a spongy, porous material with a cellular structure. It is present at the end of all long bones, such as the femur, tibia, and humerus, in the vertebral bodies of the spine, and in flat and irregular bones such as the pelvic bones [1]. Bone mineral density (BMD), age, sex, geometry, and anatomical site all have an influence on the material properties of this type of bone [2]. Mechanical properties of trabecular bone play an essential role in the biomechanical response of the whole skeleton.

The prediction of the biomechanical response of trabecular bone can be used to study the fracture risk or bone collapse, but also the press-fit fixation of orthopaedic implants. The mechanical response of the peri-prosthetic bone has a direct effect on implant fixation [3]. Already during implantation, plastic deformation of trabecular bone may occur, but also due to local overload of implants, such as the collapse of a tibial tray or unilateral knee prosthesis [4, 5]. For the development and design of new devices, it is imperative to understand these nonlinear interactions between bone and implant. Nonlinear finite element (FE) analysis can be used to study the situations mentioned earlier. However, an adequate material model that captures the post-yield behavior of the trabecular bone is necessary for accurate results [6, 7].

Several material models have been used to replicate the biomechanical response of human bone. The post-yield behavior in these models mainly has been based either on a softening von Mises (sVM) criterion, a Drucker-Prager (DP) criterion, a Mohr-Coulomb (MC) criterion, or a crushable foam (CF) model [8].

An ideal plastic model based on a sVM yield criterion was developed by Keyak et al. (2001) [9] for femoral fracture prediction in case of metastatic lesions. This model was further improved by Keaveny et al. [10] by introducing tension-compression strength asymmetry in the elastic-perfectly-plastic material model. In 2006, a DP model was used to simulate the compression and tension behavior of cortical bone, which was later modified for trabecular bone compression [11]. Also, an extended DP model was calibrated in 2009 by Mullins et al. [12] to capture the post-yield behavior of the bone, considering a pressure-dependent yield effect. A MC criterion was used by Tai et al. (2006) [13] and Wang et al. (2008) [14] to investigate bone strength based on bovine cortical bone and canine cancellous bone, respectively.

A CF model with isotropic hardening was developed by Deshpande and Fleck (2000) [15]; they introduced and calibrated a hardening equation based on hydrostatic and uniaxial compression data, defining an elliptical yield surface for metallic foams.

Kelly and McGarry (2012) demonstrated the CF model's application for bovine trabecular bone and rigid polyurethane foams [16]. They showed that this type of continuum constitutive model could be implemented for the simulation of bone behavior. The CF model is better able to incorporate the effect of pressure dependency on the yield surface than the DP or MC criterion [16]. The identification of a CF parameters with constant values for human femoral bones and vertebral bodies was performed in a study by Kinzl et al. [17] based on the yield data of whole bones. They captured the mechanical response of the bones until the ultimate yield point. In 2019, Schulze et al. performed a study in which a CF model was calibrated for synthetic bones [18]. It was shown that the CF plasticity model provided accurate predictions of acetabular cup deformation.

To develop the CF models for trabecular bone, one needs to obtain the mechanical response in two loading configurations: uniaxial compression and confined compression. As Zhao et al. reported in 2018 [19], mechanical testing of human bone under uniaxial conditions has been widely investigated over the years by numerous authors. Keyak et al. and Keaveny et al. [6, 20-22] performed comprehensive studies on the prediction of post-failure behavior of bone in uniaxial configurations. In the study by Kelly and McGarry (2012) [16], the effect of hydrostatic pressure on post-failure behavior of bovine trabecular bone was investigated, which was demonstrated to be of importance under physiological loading conditions. However, there is a limited number of studies that focus on the effect of hydrostatic pressure on post-yield behavior of human trabecular bone. Therefore, the goal of this study was to determine the post-yield response of human trabecular bone under uniaxial and hydrostatic conditions.

The present study comprises an experimental and numerical evaluation of the mechanical response of human trabecular bone. In the first phase, through experimental investigations, we determined the required parameters for the CF model (Young's modulus, yield stress, and Poisson's ratio). We examined trabecular bone samples taken from human cadaveric tibias in two configurations, uniaxial and confined compression. In the second phase of the project, the CF model was implemented in FE analyses. A numerical simulation was performed to predict the mechanical behavior (elastic and plastic) of bone under both uniaxial and confined compression. Then, the FE results were assessed in comparison to the experimental data.



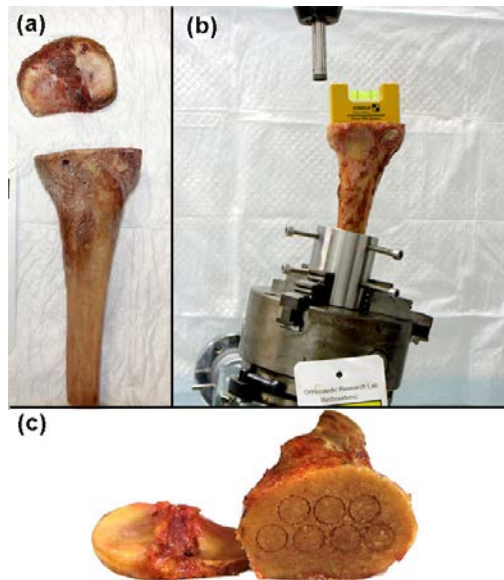
## Material and Methods

This study is divided into three main parts: 1-experimental testing of bone specimens under uniaxial and confined compression, 2-identification of material parameters for the CF model based on the mechanical testing data, and 3-FE simulations based on quantitative computed tomography (QCT) and comparison of the results with the experimental data.

### Experimental testing

#### *Specimen preparation*

Sixty-two cylindrical bone samples taken from the proximal site of 8 fresh-frozen human cadaveric tibias were examined. There were three female and five male bones, and the age range was from 62 to 93 years, with an average of 69 years. The proximal part of all tibias, including the menisci and condyles, were removed parallel to the plateau (**Figure 2-1a**). Cylindrical samples were taken from the trabecular bone sites (**Figure 2-1b**). QCT scans of the drilled bones were captured with a voxel size of  $0.4 \times 0.2 \times 0.2$  mm (Toshiba Medical Systems, Tokyo, Japan -120 kV 260mA) while a solid calibration phantom (Image Analysis, Columbia, KY) was placed under the samples in the scanner [23].



**Figure 2-1** Bone sample preparation: (a) Removal of the proximal part parallel to the tibial plateau; (b) A vertical hollow drill was used to cut the specimens in the loading direction of the tibiae; (c) Superior view of the tibia after drilling.

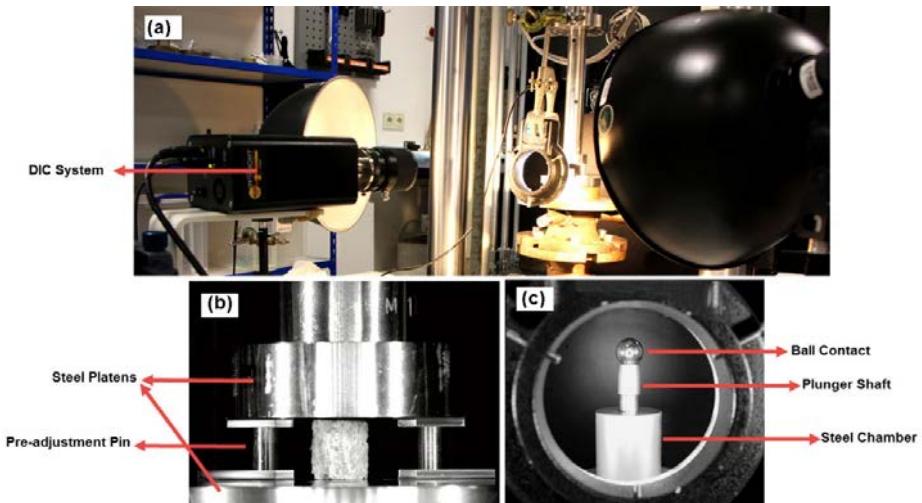
All samples were milled to the same height of 12 mm and a defined diameter of 11.6 mm, providing an aspect ratio (i.e., height to width ratio) of 1.03, avoiding buckling of the samples during the compression test [19].

To ensure fluids would not interfere with the digital image correlation (DIC) measurements, the bone marrow and other fluids were removed by centrifuging the specimens.

### ***Mechanical setup***

The specimens of each bone were divided into two equal groups, which were subjected to either uniaxial or confined compression. Uniaxial compression was performed by placing the specimens between two fixed custom-made parallel platens (**Figure 2-2b**).

The confined compression test was performed using a custom-made chamber and plunger. The inner diameter of the chamber was 11.60 mm and the plunger had an outer diameter of 11.58 mm. The measured diameters of the confined samples varied from 11.25 to 11.6 mm, which resulted in a mean tolerance of 0.10 mm ( $SD = 0.11$ ). The compressive load was applied through a plunger with a ball joint connection to the load cell (**Figure 2-2c**).



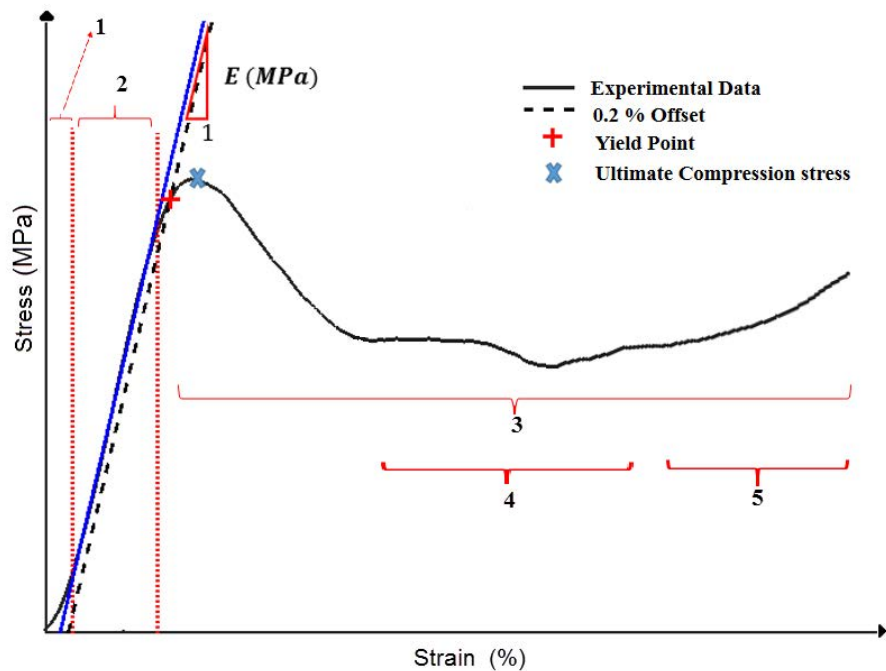
**Figure 2-2** Experimental test setup: (a) The whole setup including the DIC system; (b) Detailed view of the uniaxial configuration; (c) The confined compression setup

**Loading**

All specimens were subjected to a preload of 5-10 N to ensure uniform contact between bone and platens. Subsequently, the specimens were subjected to a destructive compression load at a constant velocity of 5 mm/min (strain rate of  $0.007\text{ s}^{-1}$ ) up to 58 % of strain.

**Data acquisition**

The DIC technique was used to measure bone strains in axial and transverse directions. The crosshead displacement of the testing machine was calibrated against the DIC displacement to account for machine compliance in the setup [24]. The deformations were obtained during the uniaxial compression test based on the DIC data to calculate the Poisson’s ratio. Images of the uniaxial compression test were continuously captured and deformations of the samples were calculated based on a custom-written Matlab script (Matlab 7.12.0 (R2018a), Mathworks, MA, USA) using automatic edge detection. It was assumed that the cylindrical bone samples deformed in an axisymmetric manner during the experiment.



**Figure 2-3** A typical uniaxial stress-strain curve of trabecular bone: 1-Toe region, 2-Elastic part, 3- Post-yield behavior, 4- plateau region, and 5-Hardening part

The force-displacement data of the compression test was converted to nominal stress-strain curves based on the original dimensions of the specimens. Three significant mechanical properties were measured (**Figure 2-3**): 1. uniaxial compressive stiffness of the elastic region (Young's modulus,  $E$ ) 2. the yield point, based on a 0.2% strain offset ( $\sigma$ ) (for both uniaxial and confined configurations) and, 3. the ultimate compressive stress. After omitting the initial toe region and the yielding region of the curve [6], the Young's modulus ( $E$ ) was computed based on the elastic portion of the stress-strain curve. The yield stress ( $\sigma$ ) was calculated using a 0.2 % offset from the elastic line, and the ultimate stress was defined as the peak of the stress-strain curve within the strain-range lower than 10%. Of these parameters, the Young's modulus, yield stress, and Poisson's ratio were applied to the FE model, while the ultimate stress was measured only for comparison and validation of the computational results.

### Material parameter identification

The Crushable Foam model with an isotropic hardening rule (ICF) [25] is governed by the von Mises equivalent stress ( $q$ ) and the hydrostatic pressure ( $p$ ). The yield surface is an ellipse centered at the origin in the  $p$ - $q$  stress plane. The yield surface extends along the pressure axis under the hydrostatic state (**Figure 2-4**).

The yield surface of the CF model with isotropic hardening ( $F_{ICF}$ ) is given by:

$$F_{ICF} = \sqrt{q^2 + a^2 p^2} - B; \quad (1) \quad B = ap_c = \sigma_{uc}^0 \sqrt{1 + \left(\frac{a}{3}\right)^2} \quad (2)$$

where  $B$  is the size of the  $q$ -axis of the yield ellipse,  $\sigma_{uc}^0$  is the absolute compressive strength under uniaxial loading and  $a$  is the shape factor of the yield ellipse and is defined as:

$$a = \frac{3K}{\sqrt{9-K^2}}; \quad (3) \quad K = \frac{\sigma_{uc}^0}{p_c^0} \quad (4)$$

In these equations  $K$  is the compression yield stress ratio, and  $p_c^0$  and  $\sigma_{uc}^0$  are the initial yield stress under hydrostatic and uniaxial compression, respectively. The shape factor  $a$  defines the relative magnitude of the axes of the yield ellipse in the  $p$ - $q$  stress plane. In the particular case when  $a=0$  the crushable foam model corresponds to the von Mises yield criterion. Moreover, the flow potential ( $G$ ) was chosen as [16, 26]:

$$G = \sqrt{q^2 + \beta^2 p^2} \quad (5)$$



Following the method implemented by Keyak et al. [6], the Young's modulus (in uniaxial compression) and yield stress (both for uniaxial and confined compression) of all samples were computed through linear regression of the experimental data. Subsequently, another regression analysis was performed to correlate the calculated model parameters with BMD using Power-law distributions. The obtained correlations were evaluated using Pearson's correlation coefficient ( $r$ ), and the standard error of the estimate ( $SEE$ ) was calculated to assess the accuracy of each prediction.

### Numerical Simulation

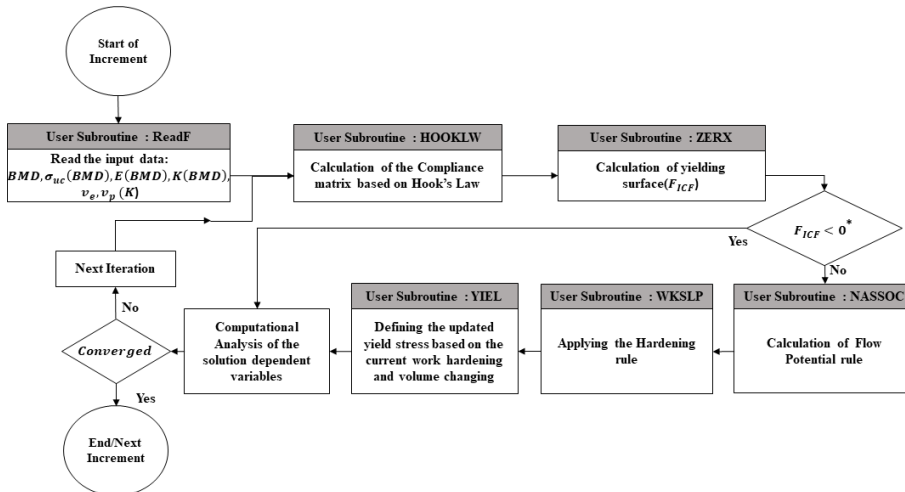
In order to assign BMD values to the specimens, a computer model of a cylinder with a diameter of 11.5 mm and a height of 12 mm was created. The cylinder was then virtually placed in the QCT images at the position of the drilled specimens to assign the local Hounsfield units (HU). The obtained values were then converted to BMD using a calibration phantom. The diameter of the cylinder was defined slightly smaller (0.1 mm) than the actual size to reduce the error of positioning.

FE analysis was performed to validate the outcomes of the numerical simulations against the experimental data for five specimens of each configuration. To accurately replicate the heterogeneous BMD distribution of the specimens, 3D models were created for these five specimens. The stress-strain response and yielding patterns of the samples in the simulation were selected to compare with the experimental results. The stress-strain response included compressive stiffness, yield stress, and post-yield behavior. The analysis was done in a displacement-controlled situation to mimic the experimental condition. A mesh convergence study was performed for a single BMD specimen with four different mesh sizes using 4-noded tetrahedral elements: 0.5, 1.0, 1.5, and 2 mm. The total strain energy of the model was selected as a target measure to determine the differences between mesh sizes. Convergence was assumed for a difference of less than 10% [27], which was achieved for the first three mesh sizes. Considering the mesh convergence results and the optimum mesh size for assigning the BMD values, the cylinder model with an element size of 1 mm was selected. Five specimens from each group with a different BMD, ranging from minimum to maximum values, were selected for the FE simulations, representing the whole BMD range of the specimens.

Simulations were performed in Marc-Mentat (MSC Software Corporation, Santa Ana, CA, USA) with a modified yield criterion for two loading conditions. The analysis was conducted in an implicit scheme with incremental loading and the large strain option was selected as the nonlinear procedure. The bone was considered as a

heterogeneous material, and the stiffness values were applied through a compliance matrix for each element. A FORTRAN routine was combined with available user-subroutines of the Marc-Mentat Libraries [28] to define the isotropic CF criterion that was dependent on the BMD values. The algorithm consisted of the definition of 1) the compliance matrix and Hooke's Law (HOOKLW), 2) the yield surface definition (ZERX), 3) the flow potential rule (NASSOC), and 4) the hardening rule (WKSPL).

Computational implementation included a yield stress update algorithm in combination with a hydrostatic pressure dependency (**Figure 2-5**). In this algorithm, first, the material parameters of the constitutive model were imported (ReadF). Next, the compliance matrix of stress-strain was defined based on Hooke's Law (HOOKLW). Then, the ZERX subroutine was used to apply the yield criterion based on the current total stress. In case the yield surface value was smaller than zero ( $F_{ICF} < 0$ ), the computation continued as elastic. In case of yielding, the algorithm would call a subroutine to define the flow direction for plasticity (NASSOC). Subsequently, the WKSPL was used to prescribe the corresponding hardening slope. Finally, the YIEL user subroutine was used to update the value of yield stress based on the current work hardening and the volume change. The analysis was continued iteratively until the solution converged. This approach allowed for considering the hardening-softening behavior of the trabecular bone structure, which led to a distinctive update of the yield surface.



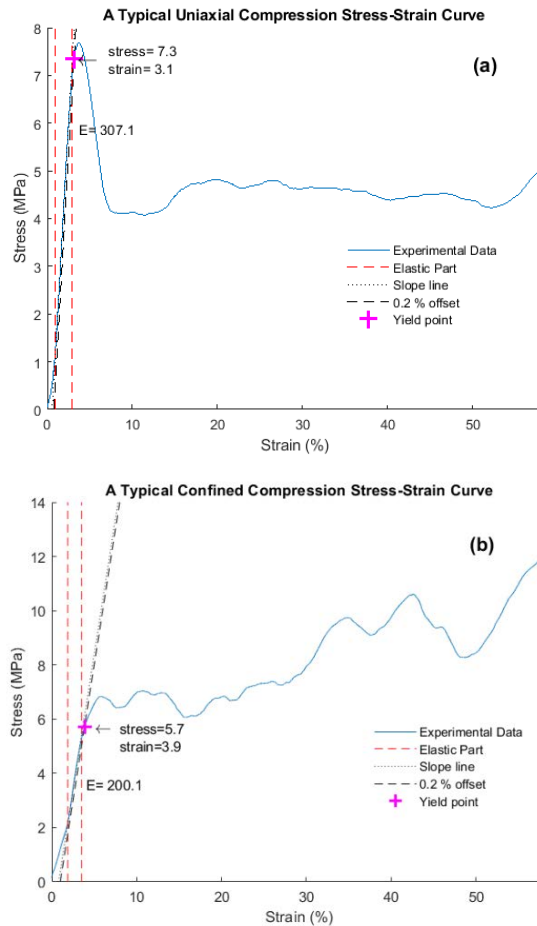
**Figure 2-5** Computational algorithm of numerical simulation, including all the necessary subroutines to be called from available Marc-Mentat routines.

## Results

### Experiment

The force-displacement data were collected for 59 of the 62 specimens; no data were obtained for three samples. Two specimens were excluded due to structural failure after centrifuging, and one was crushed under the preconditioning load. Thirty-one bone specimens were tested under uniaxial compression and twenty-eight under confined compression.

Typical diagrams of the stress-strain response of trabecular bone samples in the two configurations are shown in **Figure 2-6a-b**.

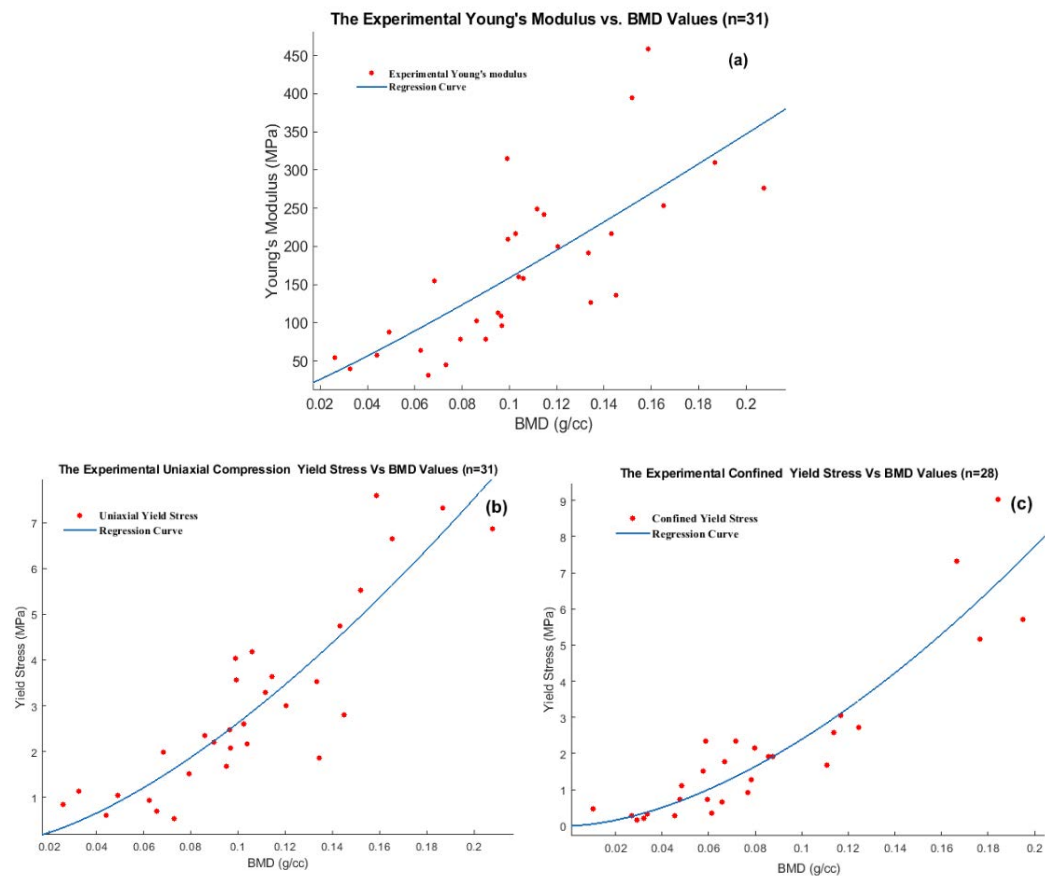


**Figure 2-6** Typical diagram of the nominal stress-strain response: **(a)** The uniaxial compression (BMD value of 187 mg/cc); **(b)** The confined compression (BMD value of 195 mg/cc).



Material parameters

Statistical analyses showed significant nonlinear correlations for the Young's modulus ( $E$ ) ( $r=0.748$ ,  $p<.001$  and  $SEE=72.17$ ) (**Figure 2-7a**), yielding stress in the uniaxial compression ( $r=0.883$ ,  $p<.001$  and  $SEE=0.951$ ) (**Figure 2-7b**) and yielding stress in the confined compression ( $r=0.921$ ,  $p<.001$  and  $SEE=0.872$ ) (**Figure 2-7c**) with the BMD values.



**Figure 2-7** The regression analyses of the measured experimental data: (a) The Youngs's modulus; (b) Yield stress in the uniaxial compression; (c) Yield stress in the confined compression.

The obtained power-law equations for the ICF constitutive model are reported in **Table 2-1**. The correlation between mechanical properties of the bone and BMD values have been characterized by the  $K$  parameter and it's corresponding plastic Poisson's ratio. Additionally, the experimental mean values of the measured parameters are also given in this table.

**Table 2-1** The empirical power relation of the material parameters based on the BMD value and, the experimental mean values of the measured parameters.

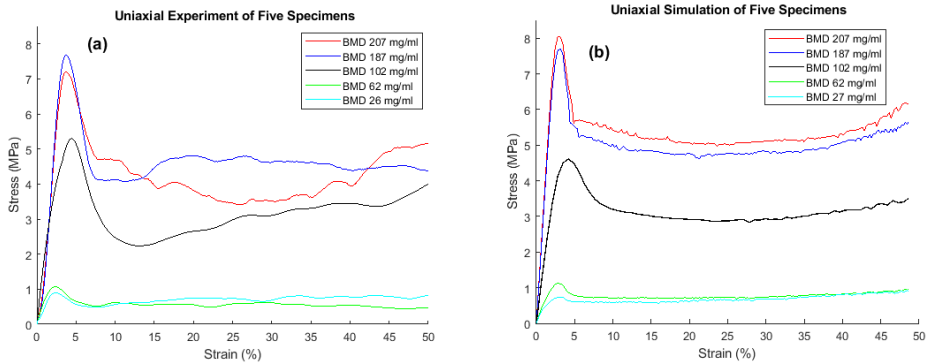
Mechanical Properties	Empirical Equation	BMD Value range g/cc	Experimental Mean value(max-min)
Compressive stiffness (E) (MPa)	$2131 \times \rho_{BMD}^{1.128}$	0.026-0.207	$168.61 \pm 104.35$ (31 – 458)
Yield Stress in uniaxial condition (MPa)	$86.73 \times \rho_{BMD}^{1.519}$	0.026-0.207	$3.01 \pm 2.05$ (0.53 – 7.59)
Yield Stress in confined condition(MPa)	$117.5 \times \rho_{BMD}^{1.691}$	0.027-0.195	$2.09 \pm 2.2$ (0.16 – 9.02)
K parameter	$1.63 \times \rho_{BMD}^{-0.162}$	>0.033	--
Elastic Poisson's ratio	Constant	0.026-0.207	$0.146 \pm 0.067$ (0.001 – 0.33)
Plastic Poisson's ratio	$\frac{3-K_{(BMD)}^2}{6}$ *	0.033-0.207	$0.133 \pm 0.055$ (0.016 – 0.27)

(\*) this equation was adapted from [15]

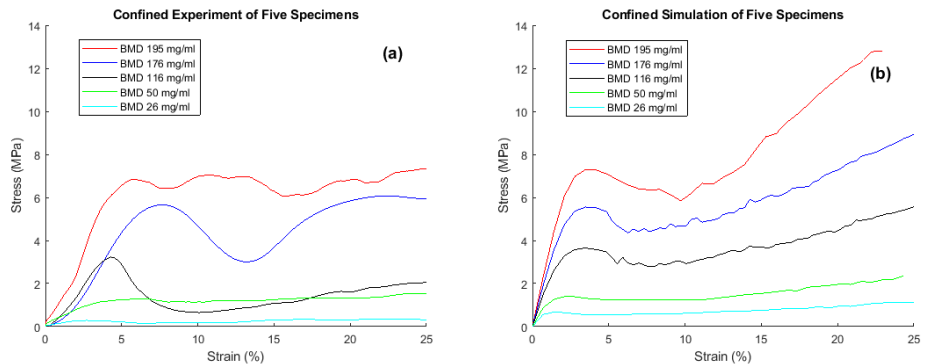
## Numerical Simulation

The calculated BMD values ranged from 26 mg/cc to 207 mg/cc for the uniaxial samples and 27 mg/cc to 195 mg/cc for the confined samples. The experimental data results, coupled with the numerical simulation outcomes of five selected samples are shown in **Figure 2-8a-b** and **Figure 2-9a-b** for uniaxial and confined configuration, respectively.

In the uniaxial configuration, the numerically obtained stress-strain curves were very similar to the experimental data. The model accurately replicated the post-yield trend of the specimens in uniaxial compression. In the confined configuration, as can be seen in **Figure 2-9**, the first part of the stress-strain curve, including the yield and ultimate stress, was consistently simulated in the FE analysis. For three specimens, the experimental results showed a plateau region in the stress-strain curve after 15% strain and started to increase, while in the other two curves, the ultimate stress was followed by a drop and then an increase in stress. The numerical simulations could capture the stress drops of the two specified samples; however, the amount of this drop was underestimated compared to the experimental results.



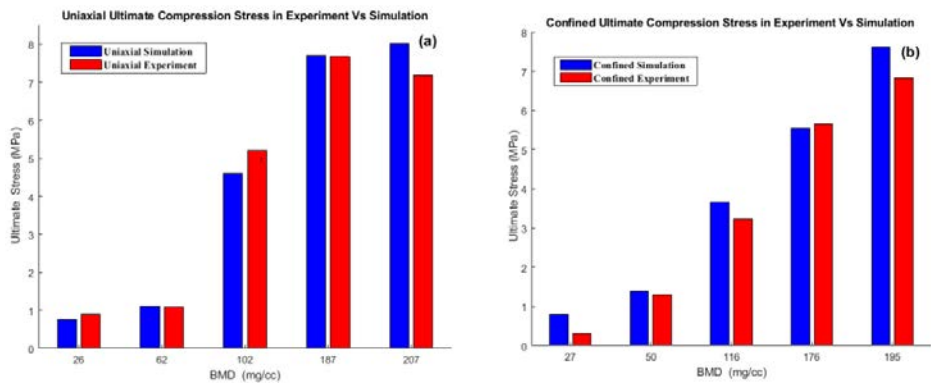
**Figure 2-8** The results of the uniaxial compression: **(a)** The experimental results; **(b)** The simulation results with the ICF model.



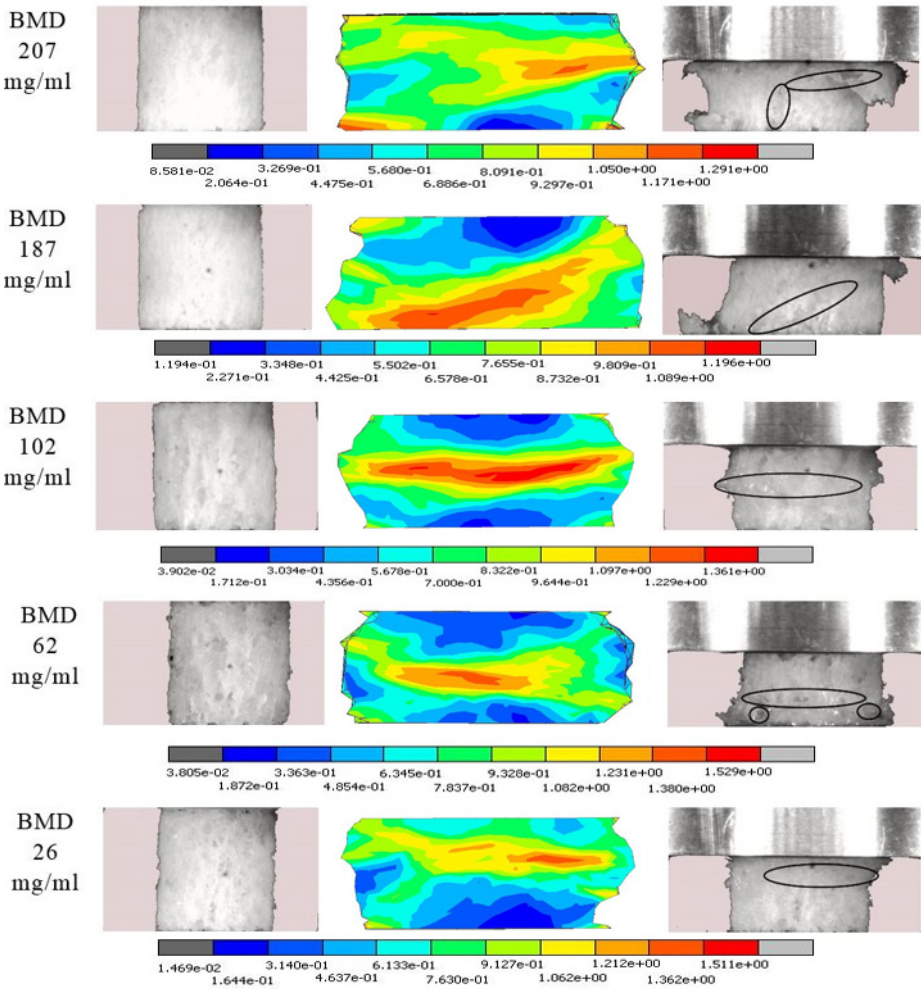
**Figure 2-9** The results of the confined compression: **(a)** The experimental results; **(b)** The simulation results with the CF model.

Numerically determined, the ultimate compressive stress of the uniaxial and confined configuration was highly accurate compared to the experimental values (**Figure 2-10a-b**). Note that the ultimate stress of the experimental data was not included as input for the CF material model and was computed based on the FE algorithm as a post-yield response.

The distribution of the equivalent plastic strain (EPS) in the uniaxial configuration is illustrated in **Figure 2-11** as a representation of plastic yielding. This computed distribution of plastic strain in the FE analysis compares relatively well with the deformations observed in the experiments.



**Figure 2-10** comparison of independent value of the ultimate stress in simulations with experimental results: **(a)** The uniaxial compression; **(b)** the confined Compression.



**Figure 2-11** Undeformed (left) and deformed (right) images of the uniaxial compression experiments for five different specimens. The black circles show the regions of large deformation in the experimental samples. The simulated equivalent plastic strain (EPS) is shown in the center. The location of the maximum values of EPS in the numerical samples was seen at the locations where large deformations occurred in the experimental samples. Note: positioning of the cutting plane (in the numerical results) can differ from the actual orientation of the specimen images.

## Discussion

In this study, we assessed the mechanical response of human trabecular bone under compressive loading conditions through experimental and numerical simulations. The load was applied in uniaxial and confined configurations to characterize the parameters of a constitutive crushable foam model that was dependent on BMD. QCT-based FE simulations of trabecular bone specimens were compared against experimental results.

The Young's modulus and yield stress measured in the uniaxial configuration of the tibial trabecular bone varied from 31 MPa to 458 MPa and 0.53 MPa to 7.59 MPa, respectively. These values are comparable to Young's modulus (8-1310 MPa) and yield stress (0.83-24 MPa) reported in previous studies [20, 29-31]. The measured values of the yield stress under confined compression in the current study (0.16-9.02 MPa) were within the range of 0.24-31.59 MPa reported by Carter et al.[32] and Charleroi et al. [33].

Regression analysis showed a strong correlation ( $p < .001$ ) of three measured parameters (compressive stiffness, uniaxial yield stress, and confined yield stress) with BMD values. The values derived here (**Table 2-1**) had a good agreement with reported values of the mechanical properties of proximal tibial specimens in the review study by Keaveny et al. (2001)[1]. However, our results were quite different from those of Keyak et al. (1996)[6], who found a Young modulus ranging from 135 MPa to 1200 MPa, and yield stress ranging from 1.36 to 9.8 MPa. This difference may be due to several factors. First, the average stiffness of the cadaveric bone samples in the study by Keyak et al. (1996) [6] was much higher compared to our samples, which may lead to different regression results. The second factor may be related to differences in the experimental setup. In the study of Ketak et al., the displacement was applied at a rate of 9 mm/min (strain rate of  $0.01 \text{ s}^{-1}$ ) on wet bone samples (including bone marrow), while in the current study, the displacement velocity was 5 mm/min (strain rate of  $0.007 \text{ s}^{-1}$ ), and liquids (bone marrow and fat) were removed from the samples before testing. However, it has been stated that a strain rate of less than  $10 \text{ s}^{-1}$  should not affect the measured stiffness of the samples, with or without the bone marrow [32, 34].

Applying the material models to FE simulations of trabecular bone in an accurate manner is a challenging procedure [8]. Many attempts have been made to apply constitutive continuum models to trabecular bone, including softening Von Mises (sVM), Drucker-Prager (DP), Extended Drucker-Prager (EDP), Mohr-Coulomb (MC),

and Crushable Foam (CF) models [9-14, 16, 17]. For constitutive modeling of cellular structures, it has been stated that the hydrostatic and deviatoric stresses should be considered together in FE analysis to have an accurate response [8, 16]. However, among the models mentioned above, only the CF and EDP are functions of hydrostatic and deviatoric stress.

The present study is the first attempt to characterize the material parameters of the ICF model dependent on the BMD. Several attempts have been made previously to calibrate the CF model for human [7, 17] and for synthetic [18, 35] bone, using a single value for the  $K$  parameter. A simplified form of a calibrated CF model (with a constant value for the corresponding parameters) was applied to femoral bones and vertebral bodies by Kinzl et al. [17]. They showed accurate results for the prediction of ultimate strength, as well as the damage distribution. In contrast to the current study, they did not include hardening-softening equations in their CF model. Therefore, the computed load-displacement curves in their study were only valid until the ultimate force. The CF model that was used in the study of Kelly et al. [7] to investigate the behavior of vertebral bodies showed a good agreement with experimental results. However, the  $\mu$ CT model in their study did not allow for using a realistic 3D geometry in a macroscale analysis. The values for the  $K$  parameter reported in these previous studies were in the range of 0.85 to 1.33, which is comparable with the values in the current study.

As shown in **Figure 2-8**, using the ICF model, the mechanical behavior of trabecular bone was adequately reproduced in numerical simulations and captured the crucial points of the stress-strain curve under compression. The measured initial yield stress and Young's modulus were already applied to the FE model as input data and had a strong correlation with the numerical outcomes. Interestingly, although no parameters from the post-yield region of the experiment were considered as input data, the numerical simulation could accurately replicate the plastic behavior of the specimens (**Figure 2-8b**). The post-yield region of the stress-strain response (ultimate stress point, softening part, plateau region, and the hardening part) could be quantified well in the simulation results. Given the three mechanical parameters as the initial input for the simulations, the ultimate stress was computed in FE simulations, which were very similar to the experimental results (**Figure 2-10**).

Considering the confined compression, Kelly and McGarry (2012) [16] showed a decreasing stress after the peak point in their bovine CF model, while their experimental results showed an increasing stress after the peak point. In the current study, the numerical outcomes of the confined simulations showed

a good agreement with the experimental results up to 15 % strain (**Figure 2-9**). After this strain level, the computed stress increased relative to experimental values due to the overestimated hardening rule. According to the study of Yu et al. [36], for a realistic FE simulation of confined compression, it is necessary to obtain sufficient modifications for the constitutive formulation. They state the hardening-softening rule must be dependent on the confined pressure, and the flow rule must be dependent on confinement level and increment rate. Therefore, in order to apply these modifications to a FE analysis, a considerable amount of experimental data under different levels of confinement is required. If these data are not included in the plasticity model, the simulations of confined configurations lead to an overestimation of the hardening rule (as is the case in the current study) or softening rule (e.g. the study of Kelly and McGrey (2012) [16]).

Since the material properties in the models were based on the actual BMD, the localized plastic behavior resulted in a good prediction of the yielding pattern. The deformations of the experimental specimens under uniaxial compression were qualitatively similar to the plastic strain distributions seen in the simulations (**Figure 2-11**). By considering the flow potential rule of the CF plasticity model (Equation (5)), the direction of the plastic strain rate vector was updated independently of the yield surface. Describing the differential changes of the plastic strain component based on the flow potential rule allowed for realistic deformations of the trabecular bone. Therefore, identifying the plastic zones with the maximum values of the equivalent plastic strain in numerical simulations could indicate the failure pattern of the experimental specimens.

Kelly and McGarry (2012) [16] applied the DP, MC, sVM, and CF model to simulate the compression situation of bovine trabecular bone. They demonstrated that none of these constitutive models could capture the confined compression response of trabecular bone, except for the CF model. The parameters  $K$  and  $v_p$  in their study were calibrated against the average stress-strain curve of the experimental results. Therefore, these parameters are only dependent on one specific BMD value of bovine bone and not on the entire range. In the study of Schulze et al. [18], it was shown that the CF plasticity model with an isotropic hardening rule resulted in an accurate prediction of deformations in synthetic bone. Considering the fact that the CF model mainly depends on the  $K$  parameter (the ratio of uniaxial yield over hydrostatic yield), they calibrated their model by assuming equality of all the yield ratios and set this parameter equal to 1. However, the current study shows that a variable value of the parameter results in a more accurate response of the cellular structure of trabecular bone.



Although this study shows good agreement between the experiments and the numerical simulations, there are some limitations. Minor experimental errors are difficult to avoid. These errors may be related to the end effects of the platens, machine compliance, sample preparation, structural damage of specimen, and the aspect ratio of the specimen's geometry, which have been reported previously as standard experimental errors [19]. Also, the perfect alignment of the bone samples with the cutting direction and axial loading remains challenging due to the complex structure of the trabecular bone. Regarding the numerical simulation, in the uniaxial configuration, the model could accurately predict the mechanical response of the trabecular bone. However, in the confined configuration, the stress was overestimated after 15 % strain. The isotropic hardening rule of the CF model contained pressure-dependent parameters. However, according to Yu et al. [36], to simulate pure confinement in FE analysis, the hardening-softening rule should be dependent on the confining pressure and requires sufficient experimental input, which was lacking in the current study. Further experimental tests and simulations of the confined situation are required to further improve the CF model. Although it is fundamental to perform hydrostatic tests (or confined tests in this study) to obtain the CF parameters, the confinement boundary condition in this level is not necessarily a correct representation of the physiological conditions in human bone. In reality, collapsing bone is surrounded by other deformable bone (both trabecular and cortical bone). Hence, a realistic mechanical response of the post-yield behavior (and its modeling) will probably be somewhere between the uniaxial and confined conditions where the confining level depends on the stiffness properties of the surrounding bone.

## Conclusion

In the present study, mechanical properties of human trabecular bone were experimentally determined dependent on BMD. Using these properties, an isotropic crushable foam model was developed. This model realistically predicted the post-yield behavior of trabecular bone under uniaxial conditions. Also, it could reproduce the pure confined compression until 15% of strain. The CF model can properly simulate orthopaedic device performance, particularly focusing on bone collapse due to the local overload around orthopaedic implants.

## Declaration of Competing Interest

None declared.

## Funding

This research did not receive any specific grant from funding agencies in the public, commercial, or not-for-profit sectors.

## Ethical approval

Not required.

## References

1. Keaveny, T.M., et al., *Biomechanics of trabecular bone*. Annual review of biomedical engineering, 2001. **3**(1): p. 307-333.
2. Keaveny, T.M., et al., *Trabecular bone modulus and strength can depend on specimen geometry*. Journal of Biomechanics, 1993. **26**(8): p. 991-1000.
3. Berahmani, S., et al., *An experimental study to investigate biomechanical aspects of the initial stability of press-fit implants*. Journal of the mechanical behavior of biomedical materials, 2015. **42**: p. 177-185.
4. Berahmani, S., et al., *Evaluation of interference fit and bone damage of an uncemented femoral knee implant*. Clinical biomechanics, 2018. **51**: p. 1-9.
5. Zimmerman, W.F., et al., *Damage in total knee replacements from mechanical overload*. Journal of biomechanics, 2016. **49**(10): p. 2068-2075.
6. Keyak, J., et al., *Postfailure compressive behavior of tibial trabecular bone in three anatomic directions*. Journal of Biomedical Materials Research: An Official Journal of The Society for Biomaterials and The Japanese Society for Biomaterials, 1996. **31**(3): p. 373-378.
7. Kelly, N., et al., *An experimental and computational investigation of the post-yield behaviour of trabecular bone during vertebral device subsidence*. Biomechanics and modeling in mechanobiology, 2013. **12**(4): p. 685-703.
8. Lee, C.-S., et al., *A new constitutive model for simulation of softening, plateau, and densification phenomena for trabecular bone under compression*. Journal of the mechanical behavior of biomedical materials, 2017. **65**: p. 213-223.
9. Keyak, J.H., *Improved prediction of proximal femoral fracture load using nonlinear finite element models*. Medical engineering & physics, 2001. **23**(3): p. 165-173.
10. Keaveny, T.M., et al., *Femoral bone strength and its relation to cortical and trabecular changes after treatment with PTH, alendronate, and their combination as assessed by finite element analysis of quantitative CT scans*. Journal of Bone and Mineral Research, 2008. **23**(12): p. 1974-1982.
11. Mercer, C., et al., *Mechanisms governing the inelastic deformation of cortical bone and application to trabecular bone*. Acta Biomaterialia, 2006. **2**(1): p. 59-68.
12. Mullins, L., M. Bruzzi, and P. McHugh, *Calibration of a constitutive model for the post-yield behaviour of cortical bone*. Journal of the mechanical behavior of biomedical materials, 2009. **2**(5): p. 460-470.
13. Tai, K., F.-J. Ulm, and C. Ortiz, *Nanogranular origins of the strength of bone*. Nano letters, 2006. **6**(11): p. 2520-2525.
14. Wang, X., et al., *Identification of material parameters based on Mohr–Coulomb failure criterion for bisphosphonate treated canine vertebral cancellous bone*. Bone, 2008. **43**(4): p. 775-780.
15. Deshpande, V. and N. Fleck, *Isotropic constitutive models for metallic foams*. Journal of the Mechanics and Physics of Solids, 2000. **48**(6-7): p. 1253-1283.
16. Kelly, N. and J.P. McGarry, *Experimental and numerical characterisation of the elasto-plastic properties of bovine trabecular bone and a trabecular bone analogue*. Journal of the mechanical behavior of biomedical materials, 2012. **9**: p. 184-197.
17. Kinzl, M., U. Wolfram, and D.H. Pahr, *Identification of a crushable foam material model and application to strength and damage prediction of human femur and vertebral body*. Journal of the mechanical behavior of biomedical materials, 2013. **26**: p. 136-147.

18. Schulze, C., et al., *Calibration of crushable foam plasticity models for synthetic bone material for use in finite element analysis of acetabular cup deformation and primary stability*. Computer Methods in Biomechanics and Biomedical Engineering, 2019. **22**(1): p. 25-37.
19. Zhao, S., et al., *Standardizing compression testing for measuring the stiffness of human bone*. Bone & joint research, 2018. **7**(8): p. 524-538.
20. Kopperdahl, D.L. and T.M. Keaveny, *Yield strain behavior of trabecular bone*. Journal of biomechanics, 1998. **31**(7): p. 601-608.
21. Keaveny, T.M., E.F. Wachtel, and D.L. Kopperdahl, *Mechanical behavior of human trabecular bone after overloading*. Journal of Orthopaedic Research, 1999. **17**(3): p. 346-353.
22. Kaneko, T.S., et al., *Mechanical properties, density and quantitative CT scan data of trabecular bone with and without metastases*. Journal of biomechanics, 2004. **37**(4): p. 523-530.
23. Eggermont, F., et al., *Calibration with or without phantom for fracture risk prediction in cancer patients with femoral bone metastases using CT-based finite element models*. PloS one, 2019. **14**(7): p. e0220564.
24. Kalidindi, S.R., A. Abusafieh, and E. El-Danaf, *Accurate characterization of machine compliance for simple compression testing*. Experimental Mechanics, 1997. **37**(2): p. 210-215.
25. Deshpande, V.S. and N.A. Fleck, *Isotropic constitutive models for metallic foams*. Journal of the Mechanics and Physics of Solids, 2000. **48**(6-7): p. 1253-1283.
26. Dassault-Systèmes, A., *Standard analysis user's manual*. Dassault Systèmes Simulia Corp., Providence, RI, USA, 2011.
27. Costa, M., et al., *Biomechanical assessment of vertebrae with lytic metastases with subject-specific finite element models*. Journal of the mechanical behavior of biomedical materials, 2019. **98**: p. 268-290.
28. Marc, M., *Volume D (User Subroutines and Special Routines)*, MSC. Software Corporation, 2012.
29. Williams, J. and J. Lewis, *Properties and an anisotropic model of cancellous bone from the proximal tibial epiphysis*. 1982.
30. Goldstein, S.A., et al., *The mechanical properties of human tibial trabecular bone as a function of metaphyseal location*. Journal of biomechanics, 1983. **16**(12): p. 965-969.
31. Rincón-Kohli, L. and P.K. Zysset, *Multi-axial mechanical properties of human trabecular bone*. Biomechanics and modeling in mechanobiology, 2009. **8**(3): p. 195-208.
32. Carter, D.R. and W.C. Hayes, *The compressive behavior of bone as a two-phase porous structure*. JBJS, 1977. **59**(7): p. 954-962.
33. Charlebois, M., M. Pretterklieber, and P.K. Zysset, *The role of fabric in the large strain compressive behavior of human trabecular bone*. Journal of biomechanical engineering, 2010. **132**(12).
34. Linde, F., et al., *Mechanical properties of trabecular bone. Dependency on strain rate*. Journal of Biomechanics, 1991. **24**(9): p. 803-809.
35. Souffrant, R., et al. *Numerical modelling of artificial bone material using crushable foam plasticity*. in *World Congress on Medical Physics and Biomedical Engineering, September 7-12, 2009, Munich, Germany*. 2009. Springer.
36. Yu, T., et al., *Finite element modeling of confined concrete-I: Drucker-Prager type plasticity model*. Engineering structures, 2010. **32**(3): p. 665-679.

## Appendix

The Crushable Foam model with isotropic hardening is a constitutive model designed to simulate the mechanical behavior of crushable, porous, or cellular materials under various loading conditions. Crushable Foam refers to materials that undergo large volumetric deformations when subjected to compressive stresses, such as metal foams, polymer foams, or trabecular bone. These materials exhibit significant plastic deformation without substantial elastic recovery.

Isotropic hardening in this context implies that as the material undergoes plastic deformation, the yield surface expands uniformly in all directions in the stress space. This means the material's strength increases equally under all stress states as plastic strain accumulates. Isotropic hardening captures the densification process where the foam structure becomes more resistant to deformation with increasing strain due to cell wall collapse and compaction.

The CF model is characterized by several key parameters that define the material's yield surface, plastic flow, and hardening/softening behavior:

1. **Mean Stress  $p$**  : Represents the hydrostatic component of the stress tensor, calculated as the average of the principal stresses. It governs the volumetric deformation of the material and is critical in materials susceptible to densification, such as foams.
2. **Deviatoric Stress  $q$**  : Describes the distortion or shape-changing component of the stress tensor, influencing the material's shear behavior. It is calculated from the second invariant of the deviatoric stress tensor.
3. **Yield Surface Size  $B$**  : Defines the boundary between elastic and plastic regions in stress space. It is directly related to the material's compressive strength and evolves with plastic deformation.
4. **Shape Factor  $a$**  : Determines the ellipticity of the yield surface in the  $p$ - $q$  plane. It controls the ratio between hydrostatic and deviatoric stress responses, influencing the transition between shear-dominated and pressure-dominated yield behavior.
5. **Flow Potential Parameter  $\beta$**  : the principal axis lengths of the flow potential ellipse in the  $p - q$  plane and is correlated by the plastic Poisson's ratio. It governs the dilation behavior during plastic deformation.
6. **Work Hardening Slope  $H$**  : Represents the rate of evolution of yield stress with plastic strain, indicating either hardening (increasing resistance to deformation) or softening (decreasing resistance).

The slope of the total (universal) stress versus the plastic strain is defined as the work hardening slope ( $H$ ) of the material. It is required to calculate the current true stress-strain curve in the plastic region to obtain the hardening slope. By assuming a direct connection between the material density change and the volumetric plastic strain,  $h_\sigma$  and  $h_p$  were specified. This specification allowed for providing the work-hardening slope as a function of the equivalent stress vs. equivalent plastic strain. The coefficient  $h_\sigma$  can be defined as the slope of the Cauchy stress versus logarithmic plastic strain ( $\epsilon^p$ ) curve in uniaxial compression ( $\frac{\partial \sigma_{uc}}{\partial \epsilon^p}$ ). Volumetric plastic strain ( $\epsilon_{vol}^p$ ) indicates the permanent change in the volume of an element and can be used to describe the yield stress, which directly defines the yield surface (Equation (1) and (2)).

$$\sigma_{uc} = c(\rho_{BMD})^d = c \left( \frac{M}{V_0(1 + \epsilon_{vol}^p)} \right)^d = \frac{c(\rho_{BMD0})^d}{(1 + \epsilon_{vol}^p)^b} = \frac{\sigma_{uc}^0}{(1 + \epsilon_{vol}^p)^b} \quad (8)$$

where  $c$  and  $d$  are experimental constants,  $\rho_{BMD}$  is the density of an element,  $M$  is the total mass and  $V_0$  is the primary volume. The relation between  $\epsilon^p$  and  $\epsilon_{vol}^p$  can be derived based on the reported equations in Deshpande and Fleck (2000)[15], by defining the ratio of  $q$  over  $p$  as  $R$ :

$$\epsilon^p = \frac{R}{\alpha^2} \epsilon_{vol}^p \quad (9) \quad \sigma_{uc} = \frac{\sigma_{uc}^0}{(1 + \frac{\alpha^2}{R} \epsilon^p)^b} \quad (10)$$

consequently, the following is obtained:

$$\frac{\partial \sigma_{uc}}{\partial \epsilon^p} = \frac{-\alpha^2 c d (\rho_{BMD0})^d}{(R + \alpha^2 \epsilon^p)^{d+1}} \quad (11)$$

in which  $\epsilon^p$  is calculated each increment, and other parameters are given as input data. The same procedure was carried out for  $h_p$  by converting the confined compression stress ( $\sigma_{cc}$ ) to the hydrostatic stress ( $p$ ) using Hooke's Law for isotropic material:

$$p = -\frac{\sigma_{cc}}{3} \left( \frac{1+\nu_e}{1-\nu_e} \right). \quad (12)$$

Substituting the derived formulations for  $h_\sigma$  and  $h_p$  from above equations the Hardening slope can be rewrite as it follows:

$$H = \left[ \frac{\sigma_e}{\hat{\sigma}} \cdot \frac{-\alpha^2 c d (\rho_{BMD0})^d}{(R + \alpha^2 \varepsilon^p)^{d+1}} + \left(1 - \frac{\sigma_e}{\hat{\sigma}}\right) \cdot \frac{(1 + \nu_e) b \sigma_{cc}^0}{3(1 - \nu_e)(1 + \varepsilon_{vol}^p)^{b+1}} \right] \quad (7a)$$

Which represent equation 7:

$$H = \left[ \frac{\sigma_e}{\hat{\sigma}} h_\sigma + \left(1 - \frac{\sigma_e}{\hat{\sigma}}\right) h_p \right] \quad (13)$$

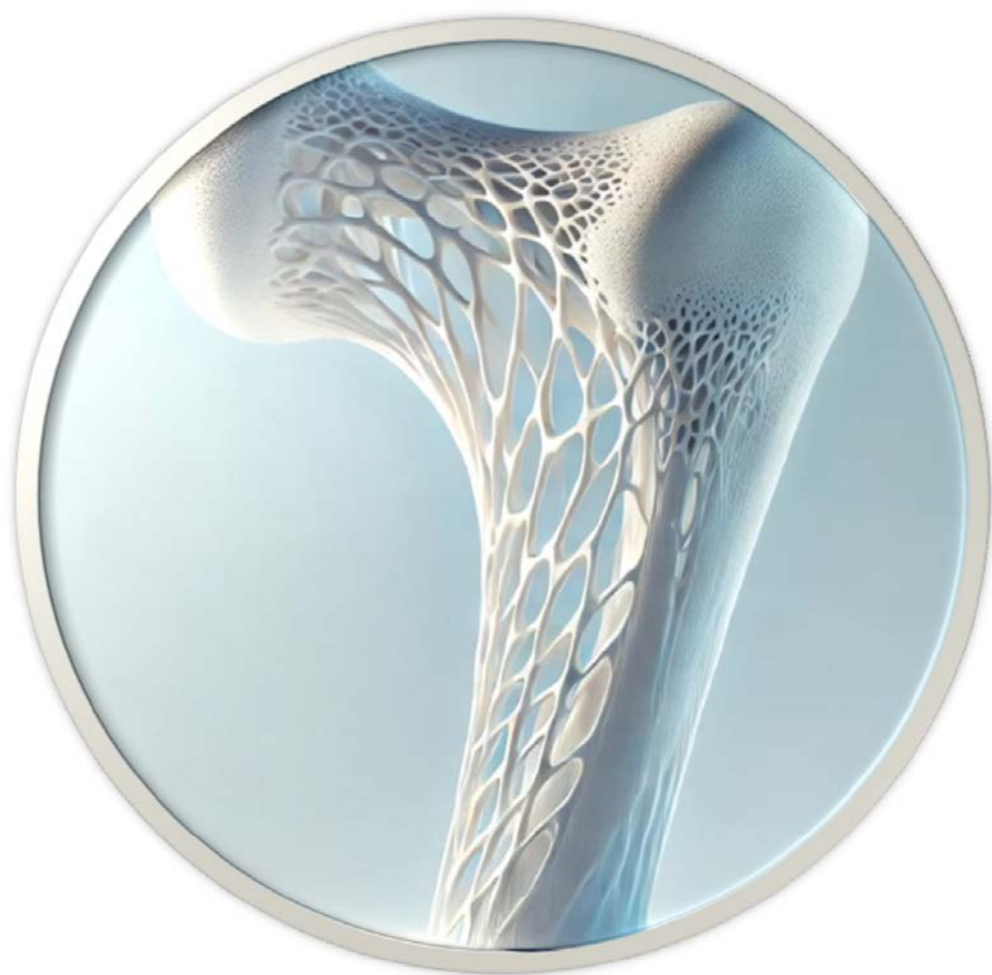
Empirical observations indicate that  $h_\sigma < 0$  signifying post-yield softening behavior typically observed in foams under uniaxial compression. This is consistent with the negative slope of the stress-strain response during plastic deformation.

Conversely,  $h_p > 0$  is observed due to the positive slope of the stress versus the logarithmic plastic strain curve under hydrostatic compression associated with volumetric compaction. This positive hardening behavior arises from foam densification, which increases the hydrostatic pressure required to sustain further volumetric collapse.

The overall hardening response,  $H$ , can exhibit either hardening ( $H > 0$ ) or softening ( $H < 0$ ) behavior, depending on the relative dominance of deviatoric and volumetric deformation modes. This variability is physically meaningful for cellular solids, as different stress states or strain levels can lead to either cell-wall collapse (associated with softening) or cell densification (associated with hardening). The ability of  $H$  to change sign captures the transition between these two distinct deformation mechanisms, providing a comprehensive framework for modeling the mechanical behavior of foams and similar materials.







## Chapter 3

# The Application of an Isotropic Crushable Foam Model to Predict the Femoral Fracture Risk

---

Navid Soltanihafshejani <sup>1\*</sup>, Federica Peroni <sup>2</sup>, Sara Toniutti <sup>2</sup>, Thom Bitter <sup>1</sup>,  
Esther Tanck <sup>1</sup>, Florieke Eggermont <sup>1</sup>, Nico Verdonschot <sup>1,3</sup>, Dennis Janssen <sup>1</sup>

<sup>1</sup>Radboud University Medical Center, Radboud Institute for Health Sciences, Orthopaedic Research Laboratory, 6500 HB Nijmegen, the Netherlands.

<sup>2</sup>Polytechnic University of Milan, Department of Biomedical Engineering, Milan, Italy

<sup>3</sup>University of Twente, Laboratory for Biomechanical Engineering, Faculty of Engineering Technology, 7500 AE Enschede, the Netherlands.

*Published in Journal of PLOS ONE on July 2023*  
<https://doi.org/10.1371/journal.pone.0288776>

## Introduction

For biomechanical simulations of orthopaedic interventions, it is imperative to implement a realistic mechanical response of the bone [1, 2]. Particularly in cases with excessive loading or weak bone strength, the plastic behavior of bone plays a significant role in the mechanical response [3]. Examples of such cases include bone fractures, collapses resulting from mechanical overload, or press-fit fixation of an implant. Finite element analysis (FEA) has proven to be a powerful tool for assessing these types of permanent deformations [4-9].

To capture the failure mechanics, it is crucial to apply an appropriate material model to predict the nonlinear response of trabecular and cortical bone [10, 11], as both can contribute significantly to bone strength [12, 13]. While the cortical bone response can be simulated quite accurately using elastoplastic material models [13], trabecular bone exhibits a more complex nonlinear behavior due to its cellular structure, which is more challenging to simulate in computational modeling [14].

In situations where the trabecular bone plays a more important role, for instance when analyzing the fixation of tibial implants in total knee arthroplasty (TKA) or intervertebral disc arthroplasty, material models such as the isotropic crushable foam (ICF) model can better represent the mechanical response of bone [15, 16]. In situations where the cortex is mainly responsible for the structural function (e.g., in the case of femoral fractures), elastoplastic material models such as the softening Von-Mises (sVM) criterion are very suitable [17, 18]. However, in most cases, both the trabecular and cortical bone simultaneously influence the mechanical response. Unfortunately, using multiple plasticity models in a single FEA simulation is complicated and may cause an undesired interference of the material models, such as inconsistent material behavior at material interfaces, complications in accurately capturing the deformation behavior of the structure, and increased computational costs. This interference may be prevented by combining the mechanical properties of trabecular and cortical bone in a single material model that incorporates the pressure dependency and deviatoric stress in the yield criterion [11, 15, 19].

Our previous study showed that the pressure-dependent ICF model can accurately capture the pre- and post-failure response of trabecular bone [11]. Kinzel et al. [19] demonstrated the possibility of using a volumetric crushable foam model to predict the strength of whole bones (femur and vertebrae). As their FEA model did not include a softening or hardening rule, it was unable to capture the post-yield behavior of the bone. However, the post-yield behavior is particularly of

importance when analyzing implant fixation and has a significant effect on the mechanics of the bone-implant interface [14]. An ICF model that combines cortical and trabecular bone and includes hardening-softening rules may therefore present a solution for various orthopaedic applications.

The current paper aims to investigate the possibility of using a crushable foam model dependent on bone mineral density (BMD) for simulating both trabecular and cortical bone. For this purpose, the elastoplastic properties of femoral trabecular bone will be determined through experimental examination of eight cadaveric bones, after which these will be combined with existing cortical bone properties reported in the literature[20]. Subsequently, the appropriateness of this combined material model will be evaluated by simulating femoral fracture experiments that were performed previously [18, 21] and by making a comparison with the results of simulations incorporating the sVM material model.

## Materials and methods

### Experimental testing

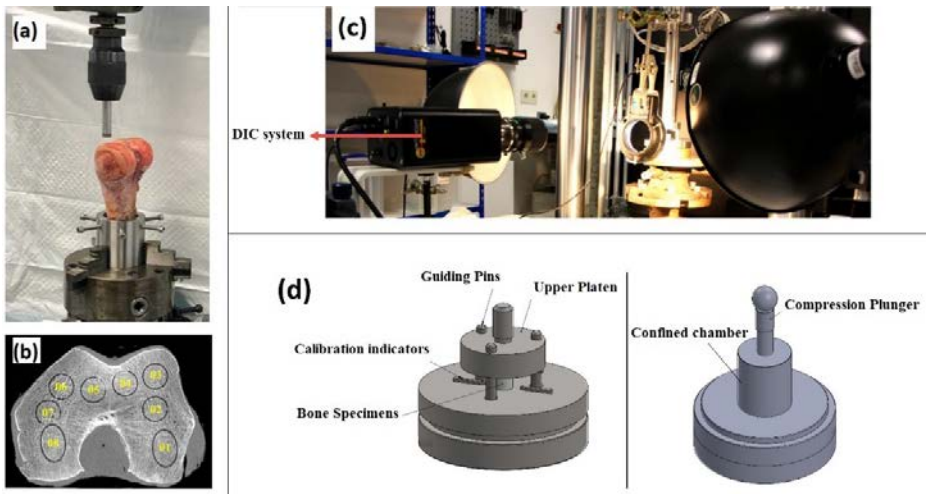
Experimental testing consisted of mechanical experiments to determine the BMD-dependent parameters for the ICF material model. In addition, proximal femoral fracture experiments were simulated to evaluate the material model. A brief description of these experiments is given here.

### *Obtaining mechanical properties of the femoral trabecular bone*

Sixty-four cylindrical samples with a height of 12 mm and a diameter of 11.65 mm were harvested from eight fresh-frozen cadaveric femurs (all male, mean age 72 years, range 60-90 years). Cadaveric Bone are obtained based on Dutch regulation from the Anatomy Department of the Radboud university medical center according to the Dutch Body Donation Program for Science and Education (Wet op de lijkbezorging, hoofdstuk V, artikel 67; 1991)[22]. Body donation of humans aged 60 years and older with a valid hand-written testament was accepted and written consent was obtained from the Head of the Anatomy Department of Radboud university medical center for the use of the cadaveric material in the current study. In order to harvest the cylindrical specimens aligned with the major trabecular orientation, the femora were positioned based on CT scans to adjust the cutting angles in the femoral condyles. Eight samples were taken from the distal part of each femur (**Figure 3-1a** and **b**). QCT scans of the drilled bones were made prior to removal of the specimens from the distal femur. The scans were captured

with a voxel size of 0.4\*0.2\*0.2 mm (Toshiba Medical Systems, Tokyo, Japan -120 kV-260mA) along with a calibration phantom (0, 50, 100, and 200 mg/ml calcium hydroxyapatite, Image Analysis, Columbia, KY, USA) placed under the bones [23] to obtain Hounsfield Units (HU) of the images. The element-specific HU densities were assigned to the geometrical mesh of each cylinder with a constrained element size of 0.4mm, which were later used in the FEA simulations. As a general representation of the bone density of the full specimen, the HU values of all elements were converted to equivalent BMD values, after which the BMD value was averaged over the elemental values for each cylinder. These average values were used for the definition or the material model.

Following our previously published methods [16], the specimens were divided into two equal groups to perform mechanical testing under uniaxial and confined compression conditions. Bone samples were placed between two parallel custom-made steel platens in uniaxial testing. In confined compression, the test was performed using a plunger and chamber to mimic a hydrostatic state (**Figure 3-1d**). The compressive load was applied through a ball-joint connection. All samples were subjected to a displacement control force, with a low strain rate of 0.007 s<sup>-1</sup>, approaching quasi-static loading, up to a strain of 0.58 to ensure substantial post-yield deformation.



**Figure 3-1** The mechanical experiment of the femoral trabecular bone, (a) Harvesting the specimens (b) Positioning of 8 samples in each bone (c) Experimental setup including DIC system (d) Loading configurations, left is the uniaxial and right is confined setup.

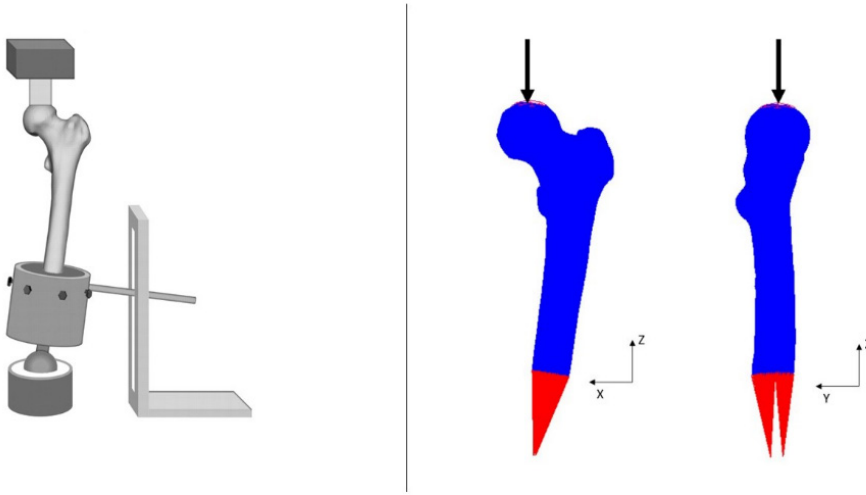
The bone strains in axial and transverse directions were measured using digital image correlation (DIC) to calculate the Poisson's ratio in uniaxial compression (**Figure 3-1c**). As the transverse strains in the confined configuration were equal to zero, only the axial strains were captured to convert the confined principal stresses to a hydrostatic state based on Hooke's Law. It was assumed that the cylindrical sample deformed axisymmetric before the yielding point (for more details, refer to [11]).

The nominal stress-strain curves of each specimen were created based on the force-displacement data. The linear elastic part of each diagram was identified to calculate the compressive modulus, the Poisson's ratio in the uniaxial compression, and the yield stress in both the uniaxial and confined conditions. The yield point was based on a 0.2% strain offset. Using Hooke's law, the confined compression yield stress was converted to hydrostatic stress. Regression analysis was then performed to correlate the mechanical parameters with the average specimen-specific BMD as a power-law equation. The correlations were evaluated using the Pearson's determination coefficient ( $r^2$ ).

### ***Proximal femoral fracture***

Five fresh-frozen human cadaveric femora, aged from 63 to 96 years old (4 male and one female), were examined previously [18, 21] to assess the failure load and fracture patterns of the proximal femur. Prior to mechanical testing, QCT scan of all femora were captured (ACQSim, Philips, Eindhoven, The Netherlands-120 kVp, 220mAs) with a slice thickness of 3.0 mm and an in-plane resolution of 0.9375 mm. A calibration phantom of hydroxyapatite (Image Analysis, Columbia, Kentucky) was placed under the bones while the images were taken.

During testing, the femora were placed in a custom-made setup (**Figure 3-2**) to restrict all the movements except rotation around the anteroposterior axis [21]. Additionally, to virtually position the femora in the FEA model, 3D coordinate information of the femora were obtained using roentgen stereophotogrammetry analysis (RSA) before loading. The goal of the experiments was to obtain an objective reproducible measurement of the strength of the femur. The orientation of single leg stance was chosen as it was easy to reproduce without a large influence of the anatomical variation between the femurs, and it represents a major loading direction of the femur. In this orientation, an axial force with a rate of 10 N/s was applied on the femoral head until failure.



**Figure 3-2** The configuration of the femora in experimental set-up [21] (left) and FEA simulation (right).

### Material model definition

For the definition of the ICF model, the Young's modulus, yield stress (both in the uniaxial and the hydrostatic compression), and the elastoplastic Poisson's ratio need to be determined. The ratio of the uniaxial and the hydrostatic yield stress defines the parameter (strength ratio) of the ICF model. Also, the plastic Poisson's ratio is dependent on this parameter [24] (**Appendix**).

Similar to our previous study [16], the ICF parameters of the trabecular bone were defined as being dependent on the average specimen-specific BMD. For the solid structure of the cortical bone, on the other hand, it was assumed that the strength ratio remained constant. Therefore, the ICF parameters for cortical bone could be characterized using the values of Young's modulus and yield stress in the uniaxial compression and a constant value of the parameter. The BMD threshold for cortical bone varied from 400 mg/ml to 1200 mg/ml [25-28]; setting this value to 950 mg/ml satisfied the continuity of the distinctive yield surfaces in the ICF model (**Eq.A1**).

Consequently, as it was assumed that the strength ratio of the cortical structure remained constant, the material properties of the femoral cortical bone reported in previous studies [20, 25, 27] could be used and combined with the trabecular data of the current study. Kaneko et al. [20] provided sufficient details for the experimental samples, and their reported data has been widely used in simulations of femoral fracture [17, 18, 23, 29]. The reported mechanical properties of the cortical bone by Kaneko et al. were obtained from the femoral diaphysis of two male donors.

## Numerical simulations

### ***FEA of materials testing with femoral trabecular bone***

FEA models were made of the cylindrical femoral trabecular bone specimens to simulate the uniaxial and confined compression experiments for comparison against the experimental results. The FEA models were assigned with the ICF model material properties based on the local element-specific HU values, using the femoral bone parameters. For comparative purposes, simulations were also performed using the sVM criterion. The FEA models were taken from our previous study [16]; for completeness, we here present the most important model features. The FEA models were created based on CT-scans of the trabecular bone specimens. To evaluate the precision of the results, a convergence analysis was performed on a sample with single BMD value using four mesh sizes (0.4, 1, 1.5, and 2 mm). The total strain energy was adopted as the criterion, and convergence was achieved for the first three mesh sizes with differences of less than 10% [11]. After evaluating the mesh convergence results and determining the ideal mesh size for assigning BMD values, a cylindrical model was selected with an element size of 1 mm. The uniaxial loading conditions were simulated through rigid plates at the top and bottom of the specimen, with frictionless contact conditions between the bone and the plates. The experimental displacements were applied to the upper plate, while the bottom plate was fixed in all directions. In the confined condition, in addition, radial expansion was restricted at the outer nodes of the cylindrical specimens to simulate the interaction between the bone and compression chamber. All simulations were performed in MSC.MARC2021 (MSC Software Corporation, Santa Ana, California).

### ***FEA of proximal femoral fracture experiments***

The FEA models of five proximal femurs were taken from our previous study [21]; the most important features are given here. FEA models of the femurs were created based on QCT scans that were used to extract the geometry and bone density. The models were created using four-noded tetrahedral elements with an element size of 2 mm in correspondence with our previous work [21]. To replicate the experimental boundary conditions, each femur model was aligned with the experimental setup based on RSA measurements. The distal part of the femur was represented by two sets of high-stiffness springs that were fixed distally. The femoral head was subjected to a displacement-controlled compressive load of 5 mm at 0.1 mm displacement increments. The compressive load was applied using a rigid cup that mimicking the experimental load applicator, which was in frictionless contact with the proximal femoral head. To prevent discretization errors leading to excessive plastic deformations, the layer of bone in direct contact with the load applicator was assigned



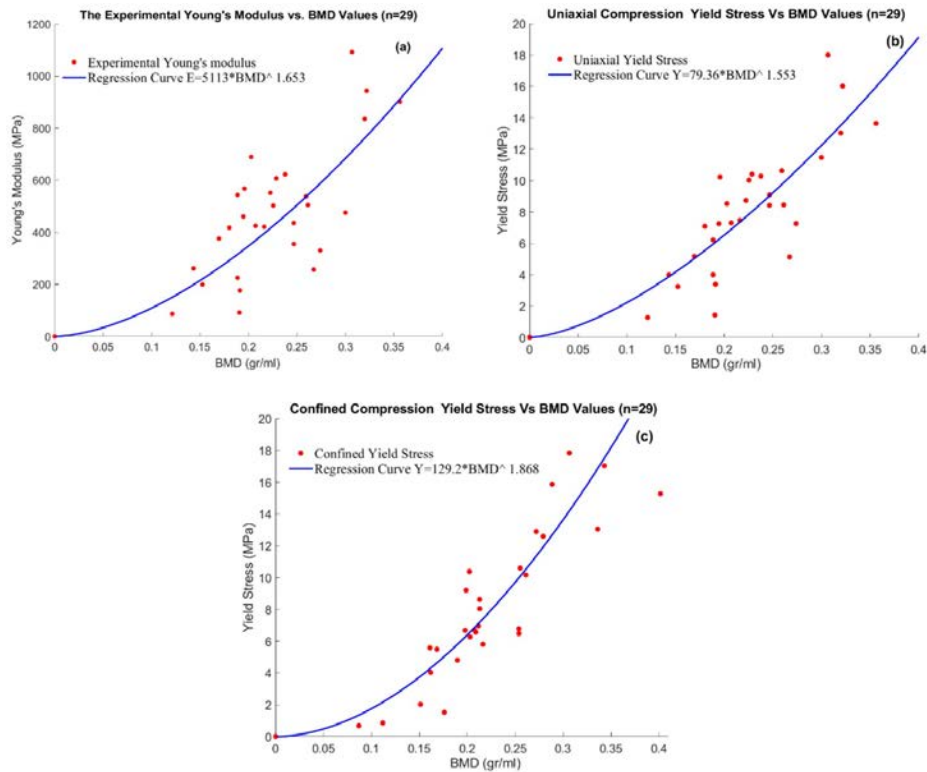
with elastic bone properties. MSC.MARC2021 (MSC Software Corporation, Santa Ana, California) was used to perform the simulations. A FORTRAN subprogram that integrated user-subroutines of the FEA software was utilized to apply heterogeneous material behavior on the model [30]. Two different constitutive material models were implemented for the assessment of the yielding (and post-yielding) behavior: the sVM and the ICF model. The ultimate failure load and yielding pattern of the proximal femurs were compared in the FEA models against experimental results. A more detailed description of the proximal femur experiments, FEA simulations, and FORTRAN subroutine can be found in previous literature [11, 18, 21].

## Results

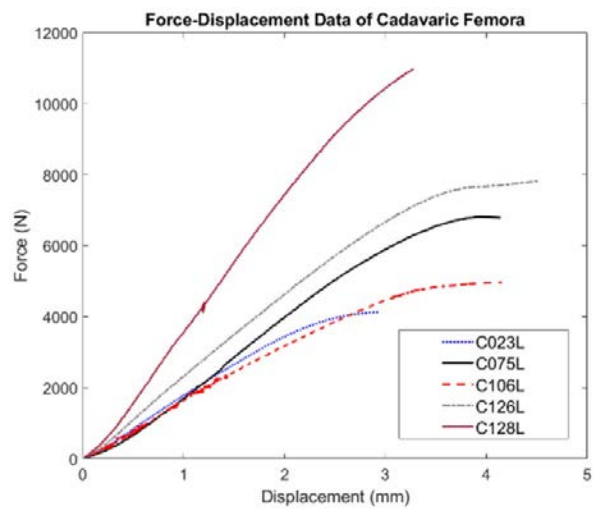
### Experimental results

Force-displacement data were collected for 58 out of the 64 cylindrical bone specimens (29 uniaxial and 29 confined tests). No data were obtained for six specimens due to structural failure during the preparation phase. The data was converted to normal stress-strain curves, and the mechanical properties were calculated dependent on BMD. Statistical Analyses showed significant nonlinear correlations for Young's modulus ( ) ( $r=0.768$ ,  $p<.001$  and  $SEE=46.76$ ) (**Figure 3-3a**) yield stress in uniaxial compression ( $r=0.836$ ,  $p<.001$  and  $SEE=0.742$ ) (**Figure-33b**) and yield stress in confined compression ( $r=0.894$ ,  $p<.001$  and  $SEE=0.873$ ) (**Figure 3-3c**) with the BMD values. The power-law correlations of each parameter are shown in Figure 3-3.

The results of the femoral fracture experiments indicate the bone stiffness, maximum compressive force, and displacement at failure (**Figure 3-4** [18]). The maximum failure force ranged from 4,137 N to 10,970 N.



**Figure 3-3** The regression analyses of the measured experimental data for femoral trabecular bone: **(a)** Young's modulus; **(b)** Yield stress in the uniaxial compression; **(c)** Yield stress in the confined compression



**Figure 3-4** Force-displacement data of five cadaveric femora [18]. Crushable foam model parameters

As mentioned before, the parameter of the ICF model was defined based on the yield stress in uniaxial and hydrostatic compression, dependent on the BMD. The power-law equation for the  $K$  parameter was defined as follows:

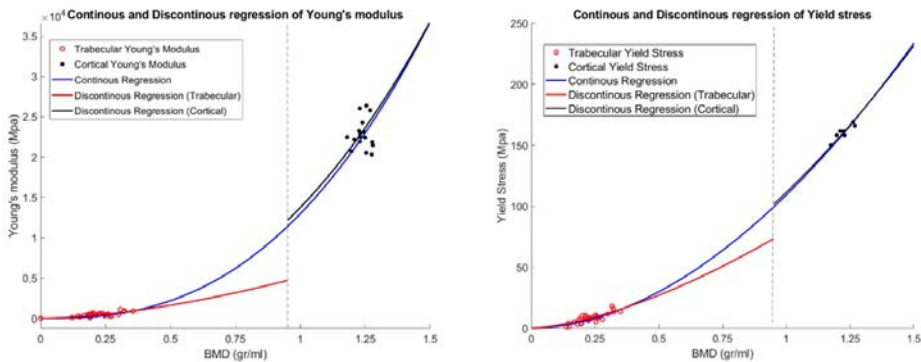
$$K = a * BMD^b$$

with  $a=1.361$  and  $b=-0.312$ . When the BMD value was above 0.400 gr/ml, the yield surface with a BMD-dependent  $K$  parameter showed minimal variation from the yield surface with a constant  $K$  parameter. This suggests that assuming an unchanged strength ratio ( $K$  parameter) for cortical bone has no significant impact on the yield surface since the BMD threshold for solid structure of cortical bone is set at a high value of 0.950 gr/ml. According to the physical definition of a cellular structure, the  $K$  parameter must adhere to  $0 < K < 3$ . Applying the upper border's limit and considering the constant value for cortical bone, equation 1 shows the whole range of the  $K$  parameter for the ICF model:

$$K = \begin{cases} 2.993 & , BMD < 0.08 \\ 1.361 \times BMD^{-0.312} & , 0.08 < BMD < 0.950 \\ 1.383 & , BMD > 0.950 \end{cases} \quad (\text{Eq. 1})$$

In Eq1,  $K$  is a dimensionless constant, and BMD represents the bone mineral density in gr/ml.

Considering the differences in BMD between trabecular and cortical bone, various regression fits were possible on the data, either in a continuous or discontinuous manner. **Figure 3-5** illustrates the two fits that were further explored in the simulations of the femoral fracture experiments. In this figure, the trabecular bone properties were obtained in the current study and the cortical data was adapted from Kaneko et al. [20].



**Figure 3-5** Continuous and Discontinuous regression of Young's modulus (left) and Yield stress (right). Cortical data was adapted from [20].

The empirical power relation of the material parameters based on the BMD value concerning **Figure 3-5** is as follows in **Table 3-1**:

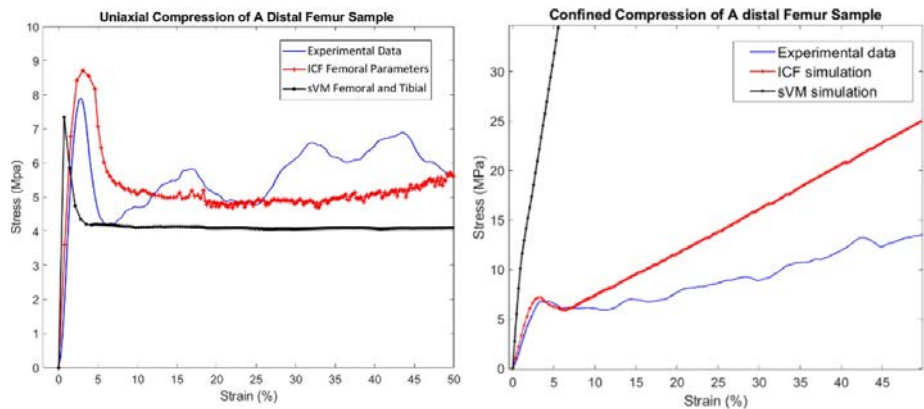
**Table 3-1** Power-Law equations of the material parameters in continuous and discontinuous approaches (BMD [gr/ml])

Mechanical Parameters	Continuous	Discontinuous
Compressive stiffness (E) (MPa)	$12980 \times \rho_{BMD}^{2.567}$ ( $r=.745, p<.001$ and $SEE=59.24$ )	$5113 \times \rho_{BMD}^{1.653}, \rho_{BMD} \leq 0.950$ ( $r=.768, p<.001$ and $SEE=46.76$ )
		$13750 \times \rho_{BMD}^{2.429}, \rho_{BMD} > 0.950$ ( $r=.725, p<.001$ and $SEE=67.43$ )
Yield Stress in uniaxial condition (MPa)	$109.3 \times \rho_{BMD}^{1.872}$ ( $r=.881, p<.001$ and $SEE=0.450$ )	$79.36 \times \rho_{BMD}^{1.553}, \rho_{BMD} \leq 0.950$ ( $r=.836, p<.001$ and $SEE=0.742$ )
		$111.5 \times \rho_{BMD}^{1.800}, \rho_{BMD} > 0.950$ ( $r=.887, p<.001$ and $SEE=0.361$ )
Elastic Poisson's ratio		0.16
Plastic Poisson's ratio		$\frac{3 - K_{(BMD)}^2}{6}$

r = Spearman's rho; p = probability; SEE = Standard Error of the Estimation

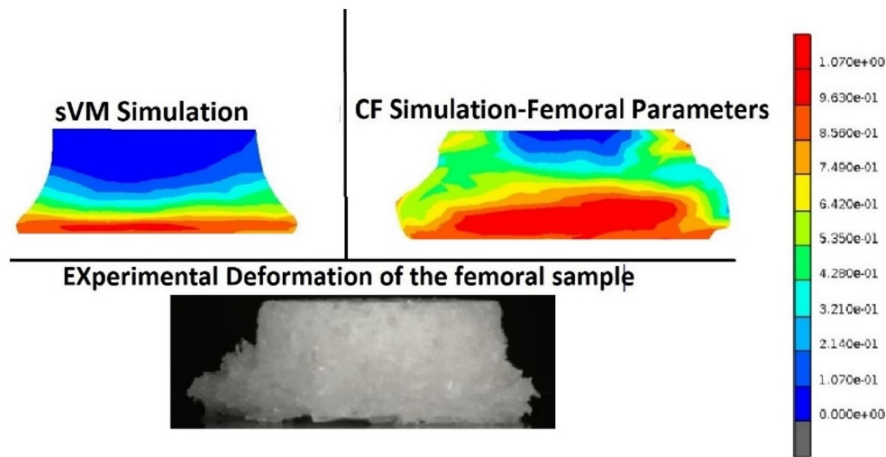
**Numerical simulation**

The ICF model and sVM material models were applied to the FEA simulation of the cylindrical bone specimens in uniaxial and confined compression. In uniaxial compression, the numerical stress-strain curves from the ICF model were very similar to the experimental data. However, in the sVM simulations, the stiffness was overestimated, resulting in an underestimation of the yield strain. In the simulations of confined compression, the stiffness, yield stress, and ultimate stress were accurately simulated with the ICF model. The sVM overpredicted the stiffness and could not reproduce the yield point. **Figure 3-6** shows the experimental and computational stress-strain curves for two typical samples tested under uniaxial (BMD of 207.5 mg/ml) and confined conditions (BMD of 208.3 mg/ml). The maximum stress value at the end of the confined simulation (50% of strain) with the sVM criterion was 280 MPa, while this value was 25 MPa for the ICF model and 14 MPa in the experimental data.







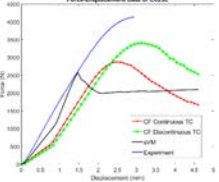
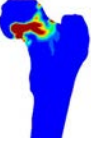
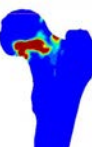
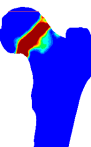

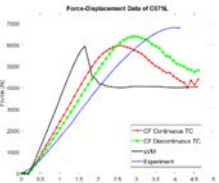
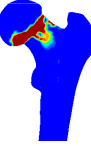
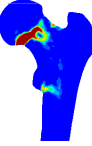


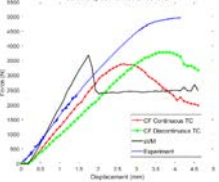
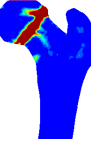
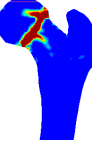


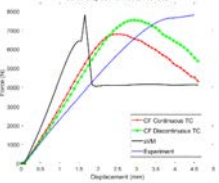
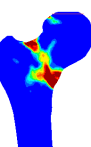
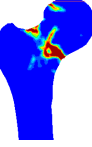
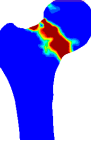

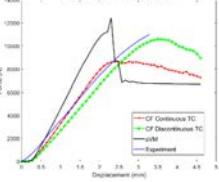
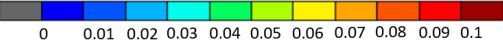
**Figure 3-6** Stress-strain data of a sample with BMD of 207.5 mg/ml in uniaxial simulation (left) and a BMD of 208.3 mg/ml in confined simulation (right) with two different material models versus experimental results.

The equivalent plastic strain (EPS) distribution of a bone sample (BMD 207.5 mg/ml) under uniaxial compression is shown in **Figure 3-7**. In contrast with the sVM model, the distribution of plastic deformation in the ICF simulation compared relatively well with the deformations observed in the experiments.



**Figure 3-7** The equivalent plastic strain represents permanent deformation of a femoral sample with a BMD of 207.5 mg/ml.

**Table 3-2** Comparison between the distributions of the equivalent plastic strain, indicating the fracture locations of the FEA models and the actual fracture location in experiment. The graphs on the right show the force-displacement data of the FEA models and physical experiments.

CF Continuous	CF Discontinuous	sVM	Experiment	Force-Displacement
				
			 *	
				
				
				
				Equivalent of Plastic Strain

\*Images of cadaveric specimens were adapted from [18].

The ICF (with continuous and discontinuous fits) and the sVM material models were subsequently applied in FEA simulations of the fracture experiments. **Table 3-2** lists the distributions of EPS, indicating the fracture locations of the FEA models, and the force-displacement data, representing the mechanical response of the bones in the simulations and experiments. The ICF model with the continuous and discontinuous fits predicted experimental failure load with an average accuracy (percentage of estimated failure load to the experimentally measured failure load) of 79% and 90%, respectively, while the sVM criterion predicted the ultimate failure load with an accuracy of 82%. Although both ICF models demonstrated a comparable stiffness of the proximal femur, the sVM resulted in a stiffer bone behavior. The sVM model provided an average accuracy of 5% for the predicted stiffness compared to the experimental values, with an over-prediction factor of 2. However, the ICF model exhibited a higher average accuracy in predicting stiffness, with 80.5% and 85.5% accuracy for the continuous and discontinuous models, respectively.

## Discussion

In the current study, we investigated the feasibility of using an ICF model that combines human trabecular and cortical bone properties to predict the mechanical response of the femur. For this purpose, data from material tests with trabecular bone were combined with cortical bone properties taken from the literature. For validation purposes, the characterized ICF model was subsequently used to simulate fracture tests of five cadaveric proximal femurs from a previous study.

The mechanical properties of the trabecular bone specimens were comparable to previous findings [16]. The compressive stiffness of current specimens was in the range of 100-1100 MPa, similar to values reported by Rho et al. (150-300 MPa) and Goldstein (7.6-1516 MPa) [31, 32]. The uniaxial yield stress of the current samples varied from 1 MPa to 18 MPa, which was within the range of 1.64-15.3 MPa measured by Kaneko et al. [33]. The compressive strength of 0.16-18 MPa for confined compression was consistent with the values reported by Carter et al. [34] and Charleroi et al. [35] (0.24-31.59 MPa). In uniaxial and confined compression, the Young's modulus and yield stress were very similar to the values for the tibial trabecular bone that we found previously [16]. However, due to the different BMD ranges, the regression analysis showed different power-law equations, leading to a different value for the parameter. Consequently, simulations with tibial and femoral ICF parameters would lead to different but yet comparable results.

Simulations of the trabecular bone experiments demonstrated that, although both material models provided a reasonable prediction for the uniaxial compression tests, the sVM model resulted in a significant overestimation of the stiffness and yield stress under confined compression, likely due to the different properties used in the sVM criterion [17]. In the sVM model, the material properties of femoral trabecular and cortical bone were based on values reported by Kaneko et al. [33],[20], with the trabecular properties being determined at a higher strain rate compared to the current study. On the other hand, another cause for the overprediction of stiffness and yield strength in the confined configuration may be that the sVM model does not consider hydrostatic stress in the yield criterion as opposed to the ICF model that was able to capture partial softening in the confined simulations.

A truly rigid confinement hardly occurs during physiological loading in human bone [16]. However, the trabecular bone is surrounded by the much stiffer cortical bone, which in some situations can result in a low-level confinement [5, 15]. For instance, during press-fit implantation of TKA the trabecular bone in the distal femur or the proximal tibia are confined by stiff cortical bone and the stiff implants, resulting in large compressive stresses [5]. A constitutive law that neglects the pressure dependency in the yield criterion may not be suitable for such situations [5, 15]. Obviously, additional research is required to investigate whether the current ICF model would provide a better representation of the bone response in such cases.

The ultimate failure load predicted by the simulations of the femoral fractures was on average 79% (3400- 8550 N) and 90% (3810-10831 N) for the continuous and discontinuous ICF material models and 82% (3700-12370 N) of the experimental value for the sVM model. The differences between the continuous and discontinuous ICF models were likely due to the differences in material mapping; in the range from 0-350 mg/ml the yield stress was higher in the continuous than in the discontinuous fit, while this was opposite in the 350-950 mg/ml BMD range. The similarity of the failure loads predicted by the ICF and sVM material models indicates that although the level of the failure load is dependent on the yield criterion, the actual yield stress value has a significant impact on the overall strength.

Fracture locations in the experiments varied and included the femoral neck (sub-capital), transcervical, and vertical femoral-neck fracture [37, 38]. The fracture locations predicted by the two ICF models were similar and comparable to the experiments, while several other FEA studies tend to predict sub-capital fractures only [13, 17, 29, 36, 37]. Likely, the pressure-dependent yield criterion and updating



of the distinctive yield surface facilitated the prediction of these various fracture locations in ICF models. In contrast to the ICF models, the sVM predicted a subcapital fracture in all cases, which was in line with previous studies in which a yield criterion without pressure dependency was used [17, 29]. This difference may result from the fact that plastic behavior in the constitutive formulation of sVM model is dependent on the constant yield criterion, which is not updated after the softening part of the plastic region. However, the mechanism for the prediction of plastic deformation in different constitutive laws is complex and cannot be identified easily.

Kinzel et al. [19] performed a similar study in which femoral fracture was simulated in a stance loading configuration. They demonstrated that a volumetric CF model could predict bone strength and deformation. Also, they compared the volumetric CF model with a sophisticated elastoplastic damage model developed by Garcia et al. [38]. The fracture area predicted in their FEA model was comparable to the experiment, both for the CF model and the sophisticated constitutive law. However, both models could only predict the failure load up to an accuracy of 59%. Kinzel et al. did not include hardening or softening parameters in their FEA models, and the CF model was applied with a constant parameter independent of bone density. The current study illustrates the importance of these factors when simulating femoral fractures.

Limitations of the current study include minor errors in the experiments such as sample preparation, end effects of the platens, and the assumption of axisymmetric deformation of the sample prior to the yielding, as explained previously [16]. Our modeling approach assumed an isotropic bone response, ignoring anisotropy due to the trabecular bone architecture and collagen fibers in the cortical bone, which may have influenced the fracture predictions. Moreover, while several studies have reported mechanical testing results of the femoral bone, the cortical bone properties used in the current ICF models were based on the study by Kaneko et al. [20, 33]. This dataset was chosen as it is the basis of the sVM model by Keyak et al. [17], which is also used at our lab for assessing the femoral fracture risk in patients suffering from metastatic lesions [17, 18, 21]. Using the same dataset for both models ensured a clean comparison of the material models. However, it is likely that using a different source for the cortical bone properties would have affected the outcome of the femoral fracture simulations. Combining multiple datasets may therefore increase the robustness of the material model.

Similarly, in the femoral fracture experiments, the measured displacements likely included some laxity in the experimental setup, which may have resulted in an

overestimation of the deformation of the femur, and as a result, underestimation of the structural stiffness [18]. Great care was taken to reproduce the experimental boundary conditions as closely as possible. The femur alignment in the experimental set-up was therefore reproduced in the FEA models based on 3D RSA measurements of the orientation of the femur relative to the loading set-up. The load applicator was represented by a rigid cup, while the distal fixation was applied to springs that were used to artificially elongate the model while reducing the actual number of elements. The boundary conditions applied distally to the springs represented the rotational degrees of freedom in the experimental set-up. Moreover, tests were performed with cadaveric bone, which may behave differently from *in vivo* bone [39]. To ensure an approximation as close as possible to *in vivo* situation, we only used fresh-frozen cadaveric samples, and minimized the number of thawing-freezing cycles and the time the tissue was exposed to room temperature.

## Conclusion

The current study aimed to develop an ICF model that combines trabecular and cortical bone properties, and to investigate whether it can predict the mechanical response of a whole femur. Simulations of compressive tests with trabecular bone specimens indicated the ICF model could accurately reproduce experimental results, even in the case of confined compression. The ICF model was able to predict the femoral bone strength similar to the previously used sVM criterion. Moreover, the ICF model was able to reproduce various fracture locations and orientations observed in the experiments. As such, the ICF model is a promising tool for the evaluation of the femoral fracture risk, but also potentially for applications such as press-fit fixation of TKA components, peri-prosthetic fractures, and collapse of joint reconstructions.

## Declaration of Competing Interest

None declared.

## Funding

This research did not receive any specific grant from funding agencies in the public, commercial, or not-for-profit sectors.

## Ethical approval

Not required.

## References

1. Anez-Bustillos, L., et al., *Finite element analysis and CT-based structural rigidity analysis to assess failure load in bones with simulated lytic defects*. Bone, 2014. **58**: p. 160-167.
2. Ovesy, M., M. Aeschlimann, and P.K. Zysset, *Explicit finite element analysis can predict the mechanical response of conical implant press-fit in homogenized trabecular bone*. Journal of biomechanics, 2020. **107**: p. 109844.
3. Zimmermann, E.A., B. Busse, and R.O. Ritchie, *The fracture mechanics of human bone: influence of disease and treatment*. BoneKey reports, 2015. **4**.
4. Wong, J., et al., *Predicting the effect of tray malalignment on risk for bone damage and implant subsidence after total knee arthroplasty*. Journal of Orthopaedic Research, 2011. **29**(3): p. 347-353.
5. Kelly, N., et al., *An investigation of the inelastic behaviour of trabecular bone during the press-fit implantation of a tibial component in total knee arthroplasty*. Medical engineering & physics, 2013. **35**(11): p. 1599-1606.
6. Thompson, S., et al., *Finite element analysis: a comparison of an all-polyethylene tibial implant and its metal-backed equivalent*. Knee Surgery, Sports Traumatology, Arthroscopy, 2016. **24**(8): p. 2560-2566.
7. Berahmani, S., et al., *Evaluation of interference fit and bone damage of an uncemented femoral knee implant*. Clinical biomechanics, 2018. **51**: p. 1-9.
8. Sasatani, K., et al., *Three-dimensional finite analysis of the optimal alignment of the tibial implant in unicompartmental knee arthroplasty*. Journal of Nippon Medical School, 2020. **87**(2): p. 60-65.
9. Eggermont, F., et al., *Can patient-specific finite element models better predict fractures in metastatic bone disease than experienced clinicians? Towards computational modelling in daily clinical practice*. Bone & joint research, 2018. **7**(6): p. 430-439.
10. Herrera, A., et al., *Applications of finite element simulation in orthopedic and trauma surgery*. World journal of orthopedics, 2012. **3**(4): p. 25.
11. Soltanihafshejani, N., et al. *Experimental and Numerical Identification of Crushable Foam Model of Human Trabecular Bone*. in *Orthopaedic Proceedings*. 2021. The British Editorial Society of Bone & Joint Surgery.
12. Manske, S., et al., *Cortical and trabecular bone in the femoral neck both contribute to proximal femur failure load prediction*. Osteoporosis international, 2009. **20**(3): p. 445-453.
13. Schileo, E., et al., *Cortical bone mapping improves finite element strain prediction accuracy at the proximal femur*. Bone, 2020. **136**: p. 115348.
14. Lee, C.-S., et al., *A new constitutive model for simulation of softening, plateau, and densification phenomena for trabecular bone under compression*. Journal of the mechanical behavior of biomedical materials, 2017. **65**: p. 213-223.
15. Kelly, N., et al., *An experimental and computational investigation of the post-yield behaviour of trabecular bone during vertebral device subsidence*. Biomechanics and modeling in mechanobiology, 2013. **12**(4): p. 685-703.
16. Soltanihafshejani, N., et al., *Development of a crushable foam model for human trabecular bone*. Medical Engineering & Physics, 2021. **96**: p. 53-63.
17. Keyak, J.H., et al., *Predicting proximal femoral strength using structural engineering models*. Clinical Orthopaedics and Related Research®, 2005. **437**: p. 219-228.
18. Tanck, E., et al., *Pathological fracture prediction in patients with metastatic lesions can be improved with quantitative computed tomography based computer models*. Bone, 2009. **45**(4): p. 777-783.

19. Kinzl, M., U. Wolfram, and D.H. Pahr, *Identification of a crushable foam material model and application to strength and damage prediction of human femur and vertebral body*. Journal of the mechanical behavior of biomedical materials, 2013. **26**: p. 136-147.
20. Kaneko, T.S., et al., *Relationships between material properties and CT scan data of cortical bone with and without metastatic lesions*. Medical engineering & physics, 2003. **25**(6): p. 445-454.
21. Derikx, L.C., et al., *The assessment of the risk of fracture in femora with metastatic lesions: comparing case-specific finite element analyses with predictions by clinical experts*. The Journal of bone and joint surgery. British volume, 2012. **94**(8): p. 1135-1142.
22. van de Volksgezondheid, G.H., *Informatie voor artsen met betrekking tot de Wet op de lijkbezorging 1991*. GHI-bulletin. Rijswijk: Staatstoezicht op de Volksgezondheid, 1991.
23. Eggermont, F., et al., *Effect of different CT scanners and settings on femoral failure loads calculated by finite element models*. Journal of Orthopaedic Research®, 2018. **36**(8): p. 2288-2295.
24. Deshpande, V.S. and N.A. Fleck, *Isotropic constitutive models for metallic foams*. Journal of the Mechanics and Physics of Solids, 2000. **48**(6-7): p. 1253-1283.
25. Öhman, C., et al., *Compressive behaviour of child and adult cortical bone*. Bone, 2011. **49**(4): p. 769-776.
26. Meema, H. and S. MEEMA, *Cortical bone mineral density versus cortical thickness in the diagnosis of osteoporosis: a roentgenologic-densitometric study*. Journal of the American Geriatrics Society, 1969. **17**(2): p. 120-141.
27. Duchemin, L., et al., *Prediction of mechanical properties of cortical bone by quantitative computed tomography*. Medical engineering & physics, 2008. **30**(3): p. 321-328.
28. Ward, K., J. Adams, and T.N. Hangartner, *Recommendations for thresholds for cortical bone geometry and density measurement by peripheral quantitative computed tomography*. Calcified tissue international, 2005. **77**(5): p. 275-280.
29. Derikx, L.C., et al., *Implementation of asymmetric yielding in case-specific finite element models improves the prediction of femoral fractures*. Computer methods in biomechanics and biomedical engineering, 2011. **14**(02): p. 183-193.
30. Marc, M., *Volume D (User Subroutines and Special Routines)*, MSC. Software Corporation, 2012.
31. Goldstein, S.A., *The mechanical properties of trabecular bone: dependence on anatomic location and function*. Journal of biomechanics, 1987. **20**(11-12): p. 1055-1061.
32. Rho, J.-Y., M. Hobatho, and R. Ashman, *Relations of mechanical properties to density and CT numbers in human bone*. Medical engineering & physics, 1995. **17**(5): p. 347-355.
33. Kaneko, T.S., et al., *Mechanical properties, density and quantitative CT scan data of trabecular bone with and without metastases*. Journal of biomechanics, 2004. **37**(4): p. 523-530.
34. Carter, D.R. and W.C. Hayes, *The compressive behavior of bone as a two-phase porous structure*. JBJS, 1977. **59**(7): p. 954-962.
35. Charlebois, M., M. Pretterklieber, and P.K. Zysset, *The Role of Fabric in the Large Strain Compressive Behavior of Human Trabecular Bone*. Journal of Biomechanical Engineering, 2010. **132**(12).
36. Keyak, J.H., *Improved prediction of proximal femoral fracture load using nonlinear finite element models*. Medical engineering & physics, 2001. **23**(3): p. 165-173.
37. Hambli, R. and S. Allaoui, *A robust 3D finite element simulation of human proximal femur progressive fracture under stance load with experimental validation*. Annals of biomedical engineering, 2013. **41**(12): p. 2515-2527.

38. Garcia, D., et al., *A three-dimensional elastic plastic damage constitutive law for bone tissue*. Biomechanics and modeling in mechanobiology, 2009. **8**(2): p. 149-165.
39. Olson, S.A., et al., *Designing a biomechanics investigation: choosing the right model*. Journal of orthopaedic trauma, 2012. **26**(12): p. 672-677.

## Appendix

The elliptical yield surface of the CF model with isotropic hardening ( $F_{ICF}$ ), which extends alongside the axes of the  $p - q$  plane, is given by:

$$F_{ICF} = \sqrt{q^2 + a^2 p^2} - B; \quad (A.1) \quad B = ap_c = \sigma_{uc} \sqrt{1 + \left(\frac{a}{3}\right)^2} \quad (A.2)$$

where  $B$  is the size of the  $q$ -axis of the yield ellipse,  $\sigma_{uc}$  is the absolute compressive strength under uniaxial loading and  $a$  is the shape factor of the yield ellipse and is defined as:

$$a = \frac{3K}{\sqrt{9-K^2}}; \quad (A.3) \quad K = \frac{\sigma_{uc}^0}{p_c^0} \quad (A.4)$$

In these equations  $K$  is the compressive yield stress ratio, and  $p_c^0$  and  $\sigma_{uc}^0$  are the initial yield stress under hydrostatic and uniaxial compression conditions, respectively. The plastic Poisson's ratio can be defined as follows:

$$\nu_p = \frac{3-K^2}{6}; \quad (A.5)$$



## Chapter 4

# The Effect of Bone Plasticity Models on Simulations of Primary Fixation in Total Knee Arthroplasty

---

Navid Soltanihafshejani<sup>a,\*</sup>, Thom Bitter<sup>a</sup>, Dennis Janssen<sup>a</sup>, Nico Verdonshot<sup>a,b</sup>

<sup>a</sup> Radboud University Medical Center, Radboud Institute for Health Sciences, Orthopaedic Research Laboratory, 6500 HB Nijmegen, the Netherlands.

<sup>b</sup> University of Twente, Laboratory for Biomechanical Engineering, Faculty of Engineering Technology, 7500 AE Enschede, the Netherlands.

*Published on March 2025 in Journal of Medical engineering and physics*

<https://doi.org/10.1016/j.medengphy.2025.104329>



## Introduction

The primary fixation of cementless total knee arthroplasty (TKA) implants depends on the press-fit conditions between the implant and the bone [1, 2]. The press-fit fixation is achieved during surgery, when the implants are impacted onto the bone that is cut with an additional interference fit relative to the implant dimensions. During impaction the bone is compressed, leading to elastic and plastic deformations that affect primary fixation [1, 3]. In preclinical evaluations primary stability is often quantified by measuring the relative displacement between the implant and the bone under physiological loads, also referred to as implant-bone interface micromotions [2, 4]. Studies have shown that long-term fixation of implants can be achieved when the micromotions remain smaller than 40–50  $\mu\text{m}$ , while values higher than 150 result in the formation of a fibrotic layer that may lead to gross loosening of an implant [2, 5, 6].

Finite Element (FE) modeling is a useful tool to simulate micromotions and to evaluate primary fixation of TKA [1, 3, 4, 7]. However, it is challenging to fully capture the complex interactions of material and contact properties of the bone-implant system. To obtain more realistic predictions it is essential to incorporate the non-linear (plastic) bone behavior in FE material models [1, 3], which requires further improvement of these models. Berahmani et al. [1] showed that the softening von Mises (sVM) plasticity model can improve prediction of micromotions compared to an elastic bone material model. Although the predictions of primary fixation improved, that study suggested utilizing a damage material model such as the Crushable Foam Model, could further improve the simulations.

A limitation of the sVM model was the amount and localization of plastic deformation that was simulated in the periprosthetic bone. Using digital volume correlation (DVC) in micro computed tomography data of distal femur before and after implantation, Rapagna et al. [8] demonstrated that permanent deformation in the periprosthetic bone is quite localized, reaching until a depth of  $2.6 \pm 0.8$  mm under the bone surface. In the simulations of Berahmani et al. [1], however, typically a significantly larger volume of plastic deformation was observed despite using the same implant and interference fit. In the past decade, a pressure-dependent Isotropic Crushable Foam (ICF) model was developed that offers advantages such as better replication of pressure-dependent plastic behavior, localized deformation patterns, and progressing yielding pattern,, particularly in simulating the post-yield behavior of human bone [9, 10]. It is, however, unknown how this post-yield behavior will affect the prediction of implant-bone interface micromotions.

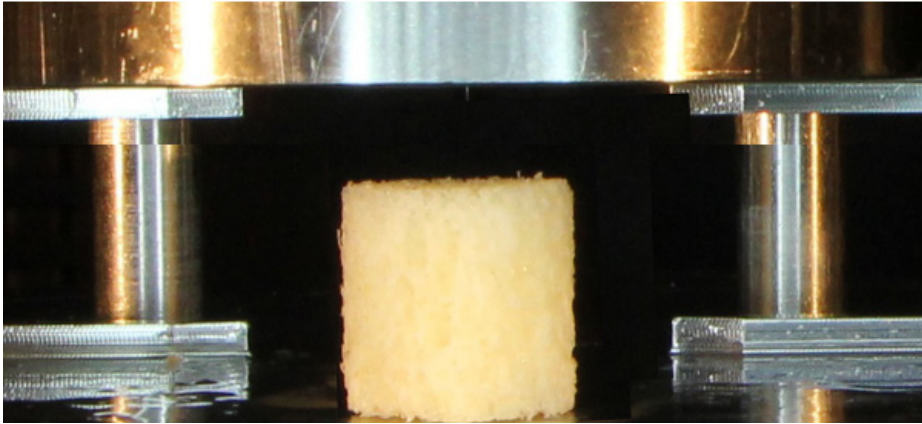
An additional aspect of micromotion simulations relates to the manner in which joint loading is represented. Typically, a limited number of loading cycles is applied to determine micromotions, while the non-linear bone response at the interface may change, particularly during the first loading cycles after implant placement. Different material models may respond differently to such loading conditions. Although the difference in response to cyclic loading between the ICF and sVM models has not specifically been investigated, plastic models with pressure-dependency (such as the ICF model) may provide a more realistic biomechanical response to cyclic loading [11-14]. Physically, this implies that multiple loading cycles may be required before the implant-bone interface reaches a steady state [15-17], which may be captured differently by the sVM and CF models. An additional response of cyclically loaded materials is the phenomenon of energy dissipation. Understanding how bone dissipates energy provides valuable insights into the reliability of a material model under cyclic loading [17-19].

In the current study we therefore aim to compare the performance of the ICF and sVM model in the simulation of primary fixation of a femoral TKA reconstruction. For this purpose, we first examined the response of human femoral trabecular bone under cyclic loading in experimental testing conditions, and compared these findings against FE simulations with the sVM and ICF material models. Next, we incorporated the ICF and sVM material models in FE models of three femoral TKA reconstructions to investigate the effect on the prediction of implant-bone interface micromotions.

## Methods

### Experiment: Cyclic loading human bone

We previously developed a pressure-dependent ICF model based on quasi-static experiments with human trabecular bone [10, 20]. In the current study we performed a limited number of additional experiments with trabecular bone specimens, which were subjected to cyclic loading to determine the effect on permanent deformation and energy dissipation. Three cylindrical samples (height 12mm, diameter 11.65mm) were harvested from the distal femur of a 70 year old male donor with good bone quality. QCT scans of the drilled bones were captured with a voxel size of 0.4\*0.2\*0.2 mm (Toshiba Medical Systems, Tokyo, Japan -120 kV-260mA) along with a calibration phantom (0, 50, 100, and 200 mg/cm<sup>3</sup> calcium hydroxyapatite, Image Analysis, Columbia, KY, USA) [21] to obtain Hounsfield Units (HU) of the images. The HU values were converted to bone mineral density (BMD) values to be used in in specimen-specific FEA simulations.



**Figure 4-1** Human bone sample in uniaxial testing configuration

Using the uniaxial loading set-up from our previous publication [10], the samples were loaded cyclically with an axial displacement of 0.5 mm (strain level of 0.04) with a sinusoidal strain rate of  $0.007 \text{ s}^{-1}$  for 100 cycles. A preload of 10 N was applied to achieve uniform contact between the bone and load applicator. The experimental set-up parameters were carefully chosen based on established methods [22, 23] to align with physiological loading conditions while avoiding strain-rate-dependent or large compressive failure to the bone structure. To minimize variability in test results due to fluid flow, fluid and marrow was removed from the samples prior to loading, using our previously established method [10]. This involved immersing the samples in a saline solution for 6 hours with shaking at 80 RPM, followed by centrifugation at 4000 RPM for 90 seconds. During loading the reaction force and the displacement were monitored to determine the permanent deformation and energy dissipation that occurred in the specimens.

## Numerical Simulations

### ***Simulation of trabecular bone experiments***

Specimen-specific FEA models were generated based on the QCT scans, which were loaded according to the experimental loading configuration. The FE models of bone specimens were identical to the experiment with a height of 12 mm and diameter of 11.65 mm. The models were analyzed with the two different material models (ICF and sVM), with material properties assigned using the local BMD values. Our previous study describes the validation of the FE methodology against experimental data and the mesh convergence study that was performed [10]. A brief description of the methods is provided here. Convergence analysis was

performed on a single-sample model meshed with 4-node tetrahedral elements at sizes of 2.0 mm, 1.5 mm, 1.0 mm, and 0.4 mm. Convergence was achieved for mesh sizes of 1.5 mm, 1.0 mm, and 0.4 mm based on the total strain energy criterion. After assessing the outcomes, a cylindrical model with a 1.0 mm element size was selected. The simulation replicated the uniaxial loading condition by employing rigid plates at the top and bottom of the specimen, with frictionless contact with the bone, and replicating the experimental displacements of the upper plate, while the lower plate was fixed in all directions. The simulations were performed in MSC software (MSC.MARC2021; MSC Software Corporation, Santa Ana, California). The simulated force-displacement curves were compared against the experimental curves to verify the results of the cyclic bone response. The energy dissipation pattern observed in the experimental samples served as the desired outcome, and a qualitative comparison was made between the results obtained from the two material models and the experimental data.

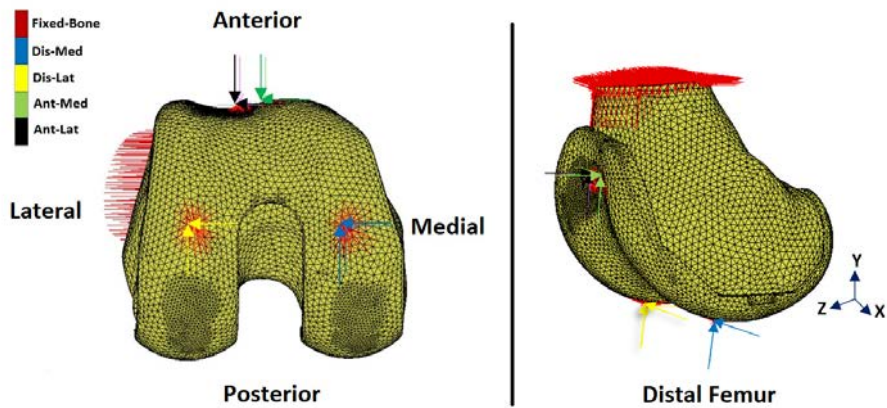
### ***Simulations of femoral total knee arthroplasty***

To study the effect of the material models on primary fixation of TKA, models were created of femoral reconstructions based on QCT scans (Toshiba Medical Systems, Tokyo, Japan; voxel size 0.6×0.4×0.4 mm, 120 kV, 260 mA) of three cadaveric femurs (all males; 57, 73 and 90 years old). A solid calibration phantom (Image Analysis, Columbia, KY) was scanned along with the femurs to compute the local BMD [24]. Three-dimensional models of the distal femur were created in 3D Slicer [25]. CAD files of the uncemented PFC Sigma Cruciate retaining (CR) femoral knee implant were kindly provided by the manufacturer (DePuy Synthes Joint Reconstruction, Warsaw, IN). The appropriate implant size was based on anthropometric measures (size 5 for each femur). Subsequently, the distal femurs were resected based on the surgical guidelines. The FE meshes of the femur and implant were created from linear four-noded tetrahedral elements with an average edge length of 2.5mm, based on a previous mesh convergence study [7]. To determine average BMD, rectangular regions of interest (ROIs) were identified in the anterior and posterior condylar regions, with a size of 35×18×5 mm and 24×18×5 mm (width×height×depth), respectively. The average BMD of the three ROIs was used to quantify BMD for each specimen (while each element of the mesh had its own individual BMD and corresponding mechanical properties).

Prior to simulating micromotions during activities of daily living, the femoral components were virtually implanted onto the resected femurs. Implantation was simulated using the interference fit option of the contact algorithm that represented the implant-bone interface [7, 26]. During the implantation phase, the

contact surface of the implant remained stationary, while the bone elements were deformed plastically to achieve the full interference fit (250  $\mu\text{m}$ ).". The coefficient of friction was set to 0.4 [1, 7]. During implantation the bone was allowed to deform plastically (see section 2.2.3).

During the micromotion analyses the models were subjected to loading profiles simulating the peak tibiofemoral and patellofemoral contact forces occurring during the stance phase of walking, derived in a previous study [7] . The joint contact forces were distributed over a small patch around the four centers of pressure (**Table 4-1, Figure 4-2**) to avoid local artefacts. The femurs were fully constrained at the proximal end. Table 1 quantifies the applied loads driven from implant-specific data.



**Figure 4-2** The loading and constraints configuration on the distal femur

The bone was simulated as a heterogeneous elastoplastic material, with mechanical properties determined from calibrated BMD values, using two constitutive material models: the ICF and the sVM model (**Table 2**). The CoCr implant was assigned with elastic material properties.

**Table 4-1** The quantification of the applied loads [7].

Sigma Implant-specific force			
Load	$F_x$ (N)	$F_y$ (N)	$F_z$ (N)
Dis-Medial	-38.1	1218.1	218
Dis-Lateral	-30.1	1053	277.4
Ant-Medial	39.1	17.3	-311
Ant-Lateral	-0.5	0.5	-60.2

**Table 4-2** Mechanical properties of the materials used in the FEA models [10, 27]

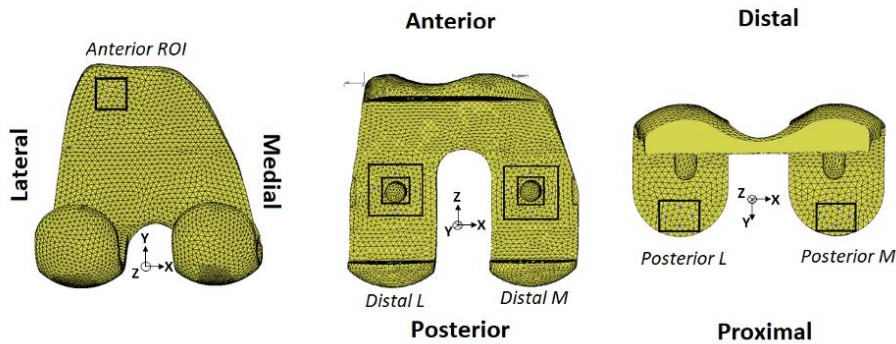
Non-linear elastoplastic behavior dependent on BMD([mg/cm3]) :			
Material	ICF		
	Young's modulus (MPa)	Yield Stress (MPa)	K parameter (strength ratio)
Trabecular bone (BMD≤0.95)	5113ρ <sup>1.654</sup> <sub>BMD</sub>	79.36ρ <sup>1.553</sup> <sub>BMD</sub>	K = 2.993, BMD ≤ 0.08
			K = 1.361ρ <sup>-0.312</sup> <sub>BMD</sub> , 0.08 < BMD ≤ 0.95
Cortical bone (BMD>0.95)	13750ρ <sup>2.429</sup> <sub>BMD</sub>	111.5ρ <sup>1.800</sup> <sub>BMD</sub>	K = 1.383
sVM			
			ρ <sub>Ash</sub> = 0.877ρ <sub>BMD</sub> + 0.0633
	Young's modulus (E; MPa)	Yield Stress (S; MPa)	Softening Parameters
Trabecular bone (BMD≤0.25)	14900ρ <sup>1.654</sup> <sub>Ash</sub>	102ρ <sup>1.80</sup> <sub>Ash</sub>	ε <sub>soft</sub> = 0.00189 + 0.0241ρ <sub>Ash</sub>
			E <sub>soft</sub> = −2080ρ <sup>1.45</sup> <sub>Ash</sub>
			S <sub>min</sub> = 43.1ρ <sup>1.81</sup> <sub>Ash</sub>
Cortical bone (BMD>0.25)			ε <sub>soft</sub> = 0.0184 + 0.0100ρ <sub>Ash</sub>
			E <sub>soft</sub> = −1000
			S <sub>min</sub> = 43.1ρ <sup>1.81</sup> <sub>Ash</sub>
Linear elastic behavior			
Material	Young modulus (MPa)		Poisson's ratio
CoCr	210,000		0.3

**Plastic deformation during implantation and cyclic loading**

The femoral TKA models were subjected to cyclic gait to investigate plastic deformation in the bone, and its subsequent effect on implant-bone micromotions. The cyclic loading was continued for 100 cycles to investigate energy dissipation in the ICF and sVM models, and to determine if a stable state of plastic deformation was achieved. A deviation of less than 1% in the number of yielded integration points was used as a criterion to determine a stabilized state [28]. In addition, the distribution of plastic deformation was compared between the two material models.

**Micromotion evaluation**

Five specific ROIs were carefully selected for each implant to measure micromotion (**Figure 4-3**), representing crucial parts of the bone-implant interface. These five specific ROIs were selected based on their biomechanical relevance and potential to exhibit significant micromotion at the implant-bone interface and were identified as critical for micromotion measurement in previous studies [1, 2]. Micromotions were determined by calculating the relative displacements at the bone-implant contact interface. Contact nodes on the implant surface were matched with the nearest bone contact faces, with the largest shear distance between these points defining the micromotion value during the loading cycle. Micromotions were initially determined after numerical settling of the simulations (at the end of fourth loading cycles), representing the situation directly post-operatively. To investigate the effect of cyclic loading and further plastic deformation, the micromotions were determined again at the end of cycle where the steady-state of plastic deformation was reached.



**Figure 4-3** The selected five ROIs on the femoral implant

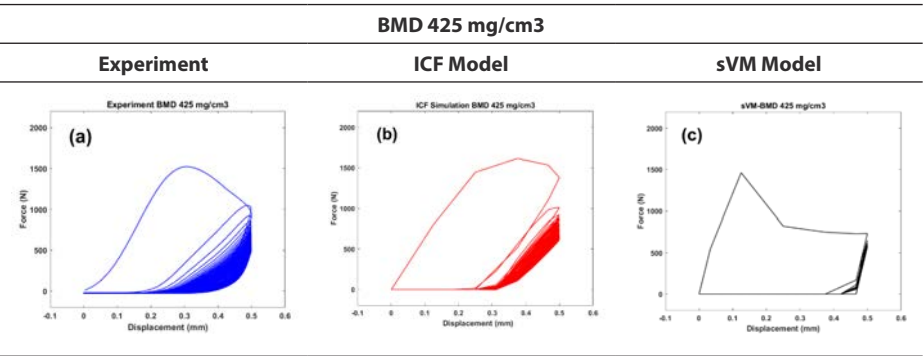
Results

Cyclic loading human bone: experimental and computational results

Force-displacement data was collected for the three samples and replicated in simulations with the ICF and sVM material models. **Figure 4-4** displays the cyclic force-displacement curves for a sample with a BMD value of 425 mg/cm<sup>3</sup> (for data on other samples, please refer to the supplementary materials, **Figure S 4-1 - Figure S 4-5**). These curves demonstrated a gradual energy dissipation pattern after the initial cycle, culminating in a point where no further energy dissipation occurred.

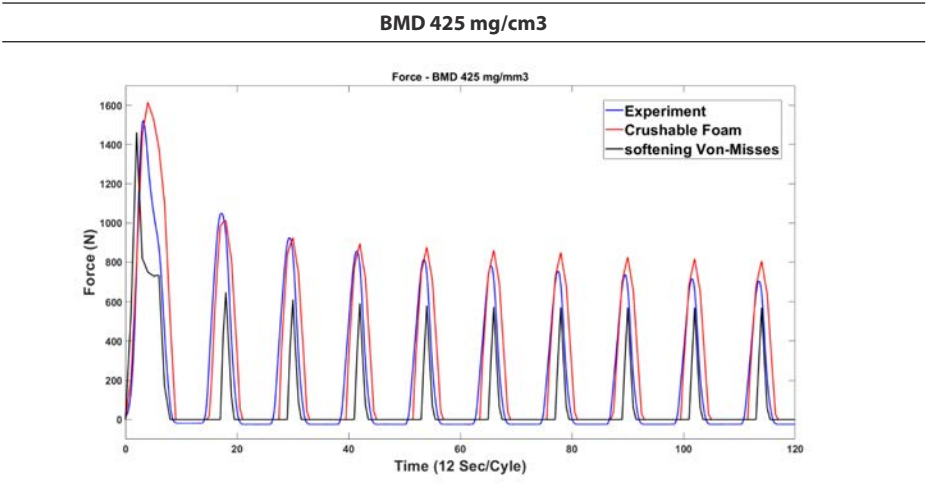
Simulations with the ICF model demonstrated data with a similar response, capturing the gradual energy dissipation with a similar force profile. In contrast, the sVM simulations only displayed energy dissipation in the first cycle, with only the initial reaction force (first loading cycle) aligning with experimental data.

During the experiments the reaction force gradually decreased with increasing number of loading cycles, up to cycle 10 (**Figure 4-5**). After that point, the reaction force remained relatively constant, with no significant deviation until 100 cycles. This gradual reduction in the reaction force corresponded with the gradual decrease in work, representing the gradual dissipation of energy. The ICF model exhibited a similar response, closely resembling the experimental cyclic forces. Conversely, the sVM simulations displayed a significant decrease of reaction force by the second loading cycle.



**Figure 4-4** Force-displacement data of the sample with BMD value of 425 mg/cm<sup>3</sup>, both in experiment and in numerical simulations. The cyclic diagram of the work done by upper platen demonstrates a representation of the dissipated energy by bone samples.





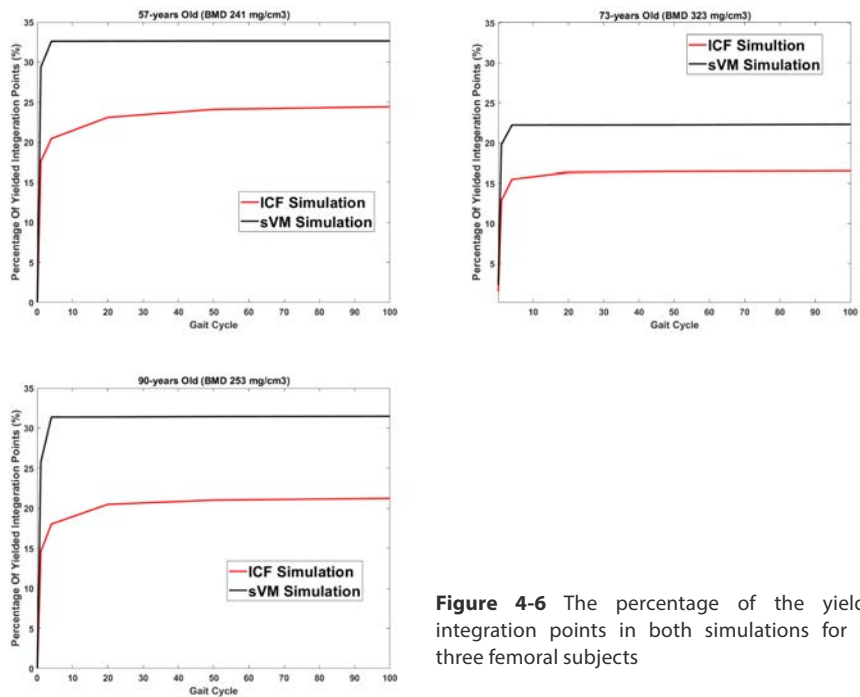
**Figure 4-5** The Force-Time diagram displays the first 10 cycles for experiment and simulations.

### Femoral TKA simulations

#### *Steady state of plasticity*

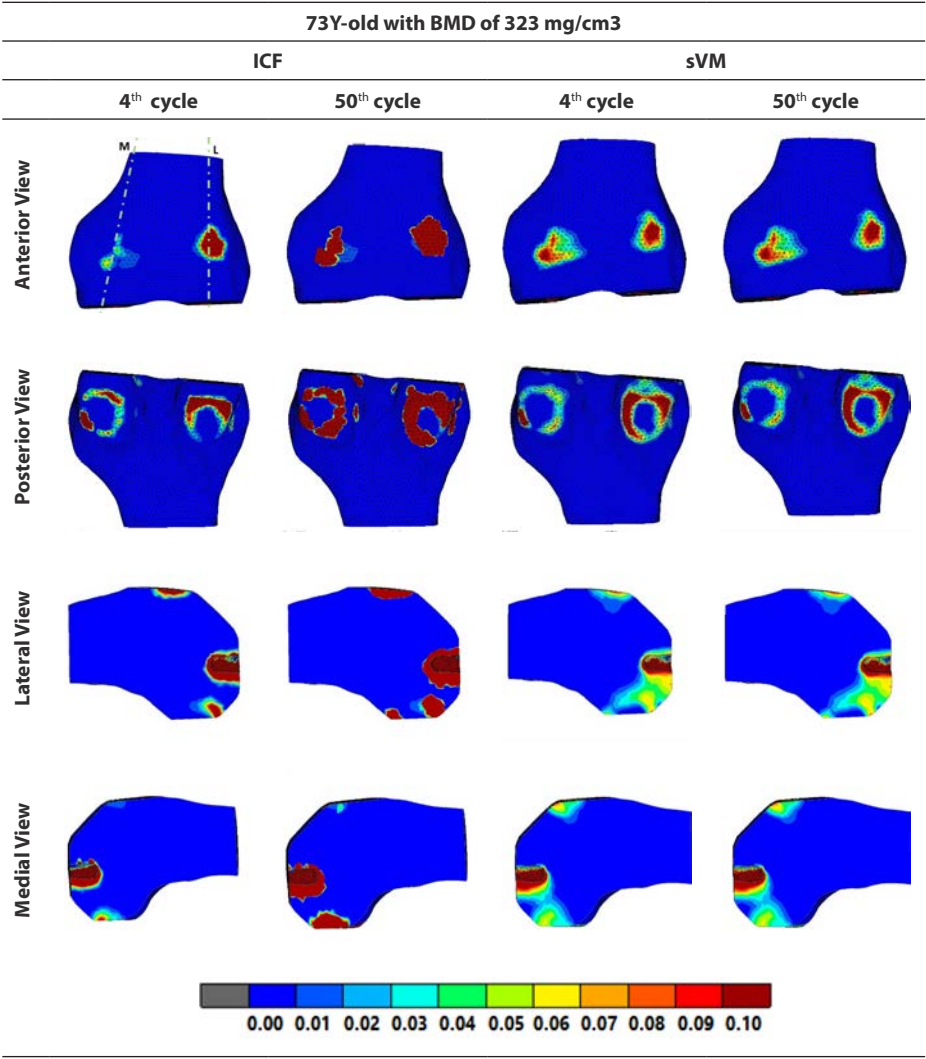
The FE models of the TKA reconstructions were used to investigate the plastic deformation that occurred under cyclic loading, and to determine whether a steady state was achieved. The steady state was defined as the loading cycle at which the increase in the number of yielded integration points was lower than 1%. For the ICF model a steady state was achieved after 20 (73-year-old specimen; 323 mg/mm<sup>3</sup>) to 50 cycles (57 year old specimen, 241 mg/mm<sup>3</sup>). Conversely, in the simulations with the sVM model the number of yielded integration points increased only up to the 4th cycle and remained constant after. Based on the results of both material models the 50th cycle was selected for further analysis of micromotions and plasticity.

The total equivalent plastic strain (TEPS) distribution at bone-implant interface (**Table 4-3**) was investigated in the initial phase (4<sup>th</sup> loading cycle) and in the steady-state phase (50<sup>th</sup> loading cycles). The TEPS distribution in the ICF models displayed a marked increase from the 4<sup>th</sup> to the 50<sup>th</sup> cycle. The majority of plastic deformation occurred at the anterior flange and posterior condyles. In simulations with the sVM model the plastic strain distribution did hardly change from 4 to 50 cycles. In both models plastic deformation was mainly concentrated around the pegs, at the anterior flange, and at the posterior condyles. In the sVM model the plastic region expanded deeper into the bone, while in the ICF model the plastic strains were more localized near the implant surface.



**Figure 4-6** The percentage of the yielded integration points in both simulations for the three femoral subjects

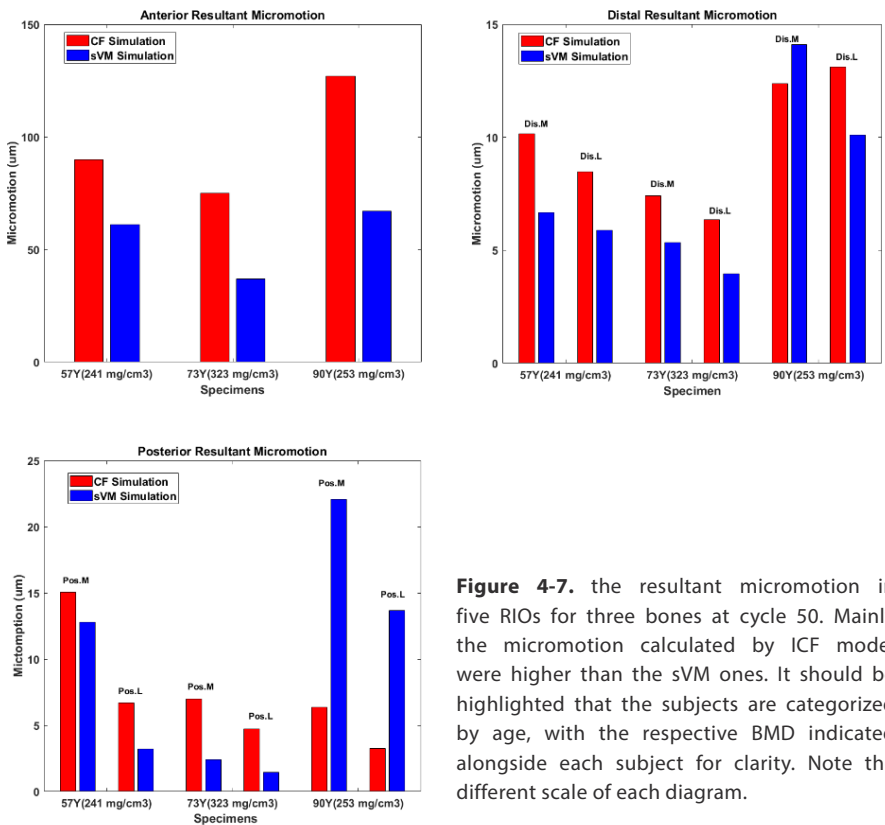
**Table 4-3** The TEPS distribution at bone-implant interface for the 73Y-old femoral subject with BMD of 323 mg/cm3. For data on other subjects, please refer to the supplementary materials (Figure S 4-6 - Figure S 4-8).



**Micromotion at the ROIs**

The ICF model generally predicted larger implant-bone micromotions than the sVM models. **Figure 4-7** provides an overview of the resultant micromotion within five RIOs for the three implanted femurs after 50 cycles. For both models, the largest micromotions were seen at the anterior flange (range 75 to 127µm in ICF, and 37 to 67µm in sVM). Distally, around the pegs, the lowest micromotions were found (6 to 13µm in ICF, 4 to 14 µm in sVM). To facilitate comparison with previous studies,

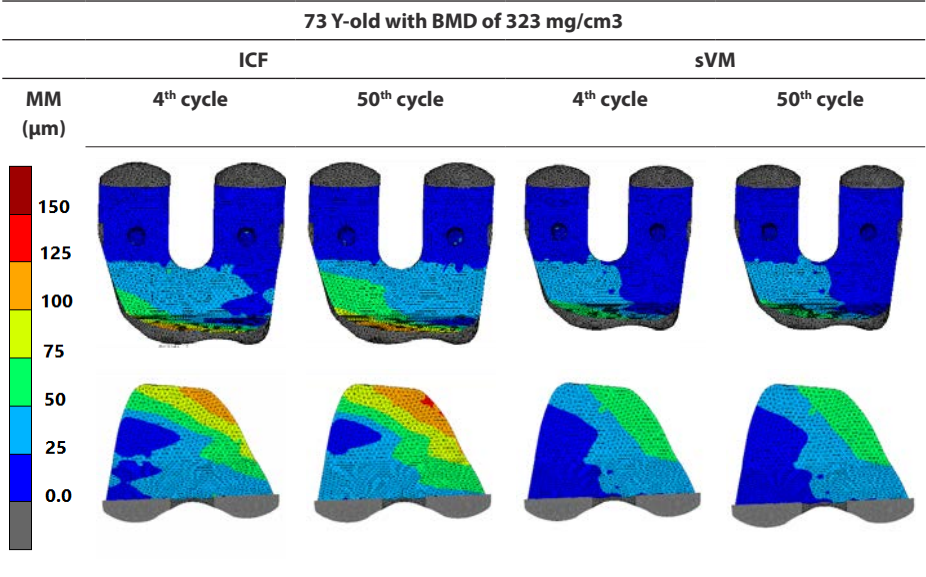
the average micromotions across the five ROIs for each subject are reported. The largest micromotions were found in the model of the 90-year-old subject (BMD  $253 \text{ mg/mm}^3$  - average micromotions of  $32\mu\text{m}$  in ICF and  $25\mu\text{m}$  in sVM), while the lowest micromotions were found in the model of the 73-year-old subject (BMD  $323 \text{ mg/mm}^3$  - average micromotion  $20\mu\text{m}$  in ICF and  $10\mu\text{m}$  in sVM).



**Figure 4-7.** the resultant micromotion in five ROIs for three bones at cycle 50. Mainly the micromotion calculated by ICF model were higher than the sVM ones. It should be highlighted that the subjects are categorized by age, with the respective BMD indicated alongside each subject for clarity. Note the different scale of each diagram.

When comparing the initial micromotions with those after 50 loading cycles, distinct differences were only found with the ICF model (**Table 4-4**). In the ICF models micromotion values increased with increasing loading cycles until 50 cycles, after which the micromotions stabilized. Among the subjects, the micromotions in the 57 and 73-year-old models remained below  $150 \mu\text{m}$ , while in the 90-year-old subject the  $150 \mu\text{m}$  threshold was exceeded (Please refer to the supplementary data for detailed micromotion distributions for the remaining subjects, Figure S 4-9). The low micromotion values ( $<20 \mu\text{m}$ ) around the pegs in all subjects and simulations indicated high stability in those regions.

**Table 4-4** Resulting micromotion distribution at the implant interface at 4th and 50th loading cycle. Note that only the micromotions in anterior regions demonstrating critical values (exceeding 50  $\mu\text{m}$ ) are reported. Micromotions in the distal and posterior regions were consistently low, with values below 20  $\mu\text{m}$  and well within the acceptable threshold of 50  $\mu\text{m}$ . These low values were not visible in the current countering format.



Discussion

In the current study we compared the effect of the sVM and ICF bone material model on the simulation of the primary fixation of femoral TKA reconstructions. We began by experimentally analyzing human femoral trabecular bone under cyclic loading and then compared the sVM and ICF models in FE simulations against experimental results. Subsequently the material models were incorporated into simulations of three TKA reconstructions of patients with different ages to evaluate their impact on predicting implant-bone interface micromotions.

Repetitive loading on femoral bone samples revealed a pattern of gradual energy dissipation, characterized by a progressive decline in reaction force with cyclic loading. The pattern observed in our research aligns with the energy dissipation patterns observed in previous studies [17]. The simulations with the sVM model did not show the gradual dissipation, but rather a large amount of plastic deformation after the first multiple loading cycles, that remained relatively constant during further cyclic loading. The ICF model was better able to replicate the gradual behavior observed in the experiments with a similar dissipation profile and comparable reaction forces.

The differences between the ICF and sVM models can be attributed to two principal factors. First, the yield strain in the sVM model is significantly lower than in the ICF model, which was also demonstrated in the previous studies [20, 29]. This difference results in premature yielding of the bone in the sVM model, while maintaining a similar maximal applied load. Secondly, the ICF model incorporates an evolving yield surface and pressure dependency, which is largely lacking in the sVM model. In the ICF model, each element has a unique yield surface that evolves with its BMD and local stress and strain conditions, allowing it to independently redistribute stresses and adjust its deformation behaviour during each loading increment, thereby mimicking the adaptive response of real bone. Such alterations are more perceptible in the cellular structure of cancellous bone, which undergoes complex deformations, while cortical bone, due to its more solid structure, demonstrates a simpler response [20, 30].

In the models of the femoral TKA reconstructions the locations of permanent bone deformations aligned with previous experimental findings with similar reconstructions. In the ICF model, the plastic strains concentrated around pegs and at the anterior and posterior condyles. The sVM model exhibited a similar distribution, but the regions of plastic deformations reached deeper into the bone. The study of Rapagna et al. [8] demonstrated permanent bone damage to be mainly localized near the bone-implant interface, similar to the patterns seen in the ICF models. Similarly, Kelly et al. reported that the plastic deformation predicted by the crushable foam model closely matches experimental observations during implantation [29].

The average micromotion for the three subjects was 27  $\mu\text{m}$  with the ICF model and 17  $\mu\text{m}$  with the sVM model. Berahmani et al. [1], using the sVM model, reported average micromotions of 43  $\mu\text{m}$  from experimental measurements for two femoral specimens with BMD values of 268 and 318  $\text{mg}/\text{cm}^3$ , and 20  $\mu\text{m}$  from numerical simulations for both specimens. While a direct point-to-point comparison between our numerical simulations and their experiments is challenging due to differences in the bone samples that were used, it is important to highlight that Berahmani et al. used the same implant and surgical technique as in our study. When considering both the experimental and computational results with the sVM model in Berahmani's study and the computational results with the ICF and sVM models in our study, the micromotion values simulated using the ICF model seem to approximate the experimental values more closely than those simulated using the sVM model. Sanchez et al. reported an average micromotion of 25  $\mu\text{m}$  for six femoral subjects with an average age of 55 (BMD was not reported), consistent with our findings for both the ICF and sVM model. While the micromotions simulated

here seem to be reasonably comparable with experimentally measured values, a specimen-specific comparison would be required to further validate the application of the two material models.

In line with previous findings [7, 26, 31], the micromotion distributions in both the ICF and sVM models consistently show the highest micromotion values occurring at the anterior flange. Low micromotions (less than 20  $\mu\text{m}$ ) were consistently observed around the pegs in all subjects and simulations in our study, which is similar to previous reports [7, 26], suggesting a minimal risk of loosening in the distal region under the current interference fit and loading conditions.

Among the subjects in our study, both the 57 and 73-year-old individuals maintained micromotion values below 150  $\mu\text{m}$  throughout the loading cycles in both simulations. However, the 90-year-old subject exceeded the 150  $\mu\text{m}$  threshold with the ICF model. While the BMD values of the 57-year-old subject (241  $\text{mg}/\text{cm}^3$ ) and the 90-year-old subject (253  $\text{mg}/\text{cm}^3$ ) were similar, it is important to note that computed micromotion values are influenced not only by BMD value, but also by BMD distribution, implantation method (which can be affected by bone shape and bone cuts) and the obtained interference fit of each bone. This phenomenon was also observed in the experimental study of Berahmi et al. [1], where a subject with a BMD of 121  $\text{mg}/\text{cm}^3$  exhibited lower micromotions compared to a subject with a higher BMD (141  $\text{mg}/\text{cm}^3$ ).

While cyclic loading had a distinct effect on the permanent deformation in the simulations with the trabecular bone specimens, its effect on micromotions in the TKA models was limited, both for the sVM and ICF models. In the sVM simulations the micromotion distribution remained more or less constant from the 4th to the 50th cycle, while the ICF simulations exhibited a slight change in distribution during the first 50 loading cycles, stabilizing thereafter. Although noticeable in the ICF model, this change in distribution remained smaller than 15  $\mu\text{m}$  throughout the entire loading cycles. This limited impact of cyclic plasticity can probably be attributed to the dominant role of the cortical bone in sustaining primary fixation. Previous studies [32-34] highlight the substantial contribution of the cortical bone in fixation of the femoral implant. However, in tibial TKA the difference between the ICF and sVM models may be more pronounced, as tibial fixation may be more dependent on the mechanical response of the trabecular bone.

Another difference between the ICF and sVM material models is their response to confined compression, which may partially occur in a femoral TKA situation where

trabecular bone is constrained by the stiffer cortical bone. Studies [10, 20, 35] have demonstrated that a non-linear plastic model lacking pressure dependency (such as the sVM model) is less suitable for such circumstances, while a pressure-dependent material model (such as the ICF model) is better capable of mimicking the mechanical response.

the parameters used in the sVM model, such as yield stress, softening modulus, and transition thresholds, could potentially influence micromotion predictions. While this study utilized sVM parameters based on Kaneko et al. (2003)[27], the applicability of these findings to other sVM definitions requires further investigation. However, capturing the cyclic response, including the energy dissipation pattern and plastic deformation behavior, remains governed by the constitutive formula, which is intrinsic to the model. Therefore, altering the mechanical parameters would not fundamentally change the response dictated by the constitutive law of the sVM.

This study has certain limitations that offer opportunities for further improvement. Firstly, we did not validate the results of the TKA models against specimen-specific experimental results. While our models produce micromotion patterns and magnitudes that are comparable to previous experimental and computational findings, a more detailed validation would provide more insights into the manner in which the material models influence the simulations of primary fixation. Similarly, it would be interesting to investigate the effect of the material models in a tibial TKA reconstruction, where the fixation principles are different as compared to femoral TKA. Another limitation is the use of a relatively simple frictional model and a low interference fit in our simulations. While these choices were made for the sake of consistency and based on previous experimental data [1, 7], future simulations could benefit from more sophisticated frictional models and actual press fit sizes for implantation. Additionally, while the micromotion distributions align with previous studies, it is important to note that the interference fit was modelled using a contact algorithm rather than a direct simulation of the press-fit process, which could provide additional detail on localized deformation. Further validation of this approach in future studies is warranted. Finally, the selected mesh size (1.0 mm) balanced computational efficiency and accuracy, as confirmed by convergence analysis. While sufficient for capturing the overall BMD/modulus distribution in the current study, finer details such as cortical thickness and material property gradients near the femoral cut surface may not be fully resolved, given the voxel size of  $0.4 \times 0.2 \times 0.2$  mm.



## Conclusion

This study investigated the capability of the ICF and sVM models of replicating the non-linear plastic response of femoral bone under cyclic loading conditions, and applied the two material models in simulations of primary fixation of femoral TKA. The ICF material model replicated the energy dissipation under cyclic loading more closely as compared to the experimental tests. This material model furthermore displayed more realistic plastic strain distributions and micromotion patterns.

### Ethical approval

Not required.

### Funding

This research did not receive any specific grant from funding agencies in the public, commercial, or not-for-profit sectors.

### Declaration of Competing Interest

Authors declare that they have no conflict of interest.

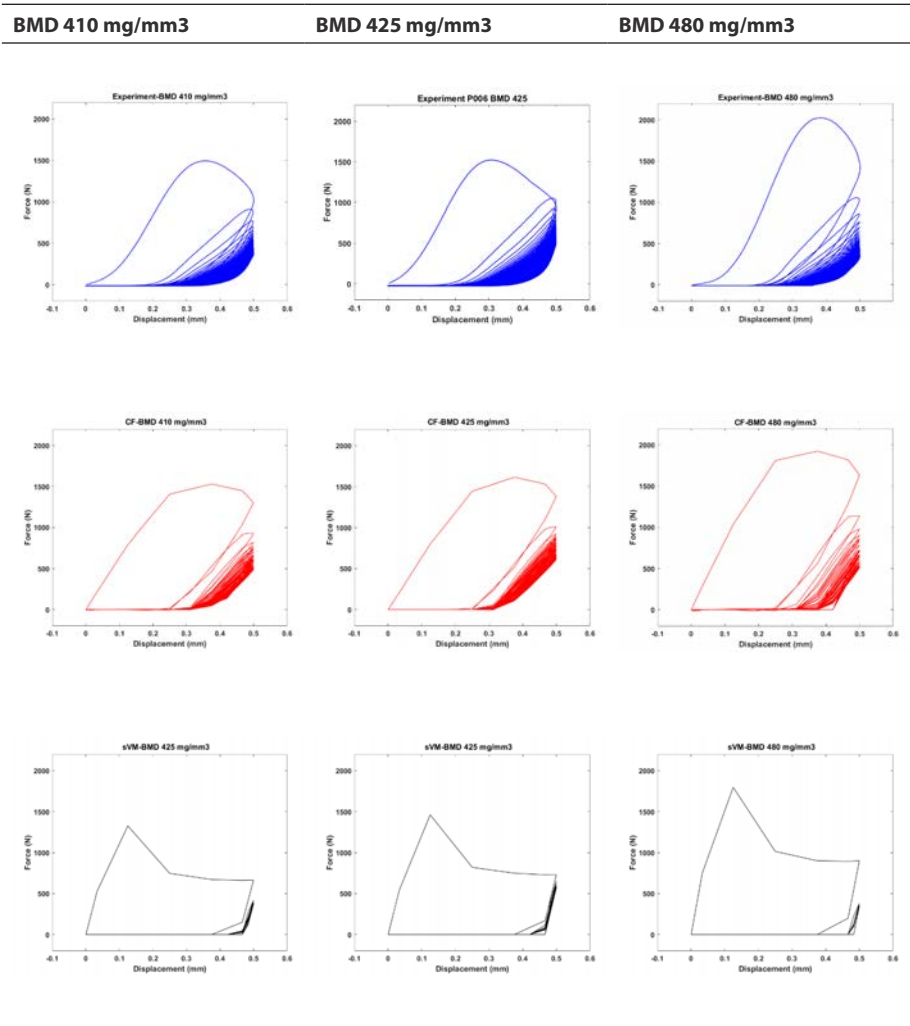
## References

1. Berahmani, S., D. Janssen, and N. Verdonchot, *Experimental and computational analysis of micromotions of an uncemented femoral knee implant using elastic and plastic bone material models*. Journal of biomechanics, 2017. **61**: p. 137-143.
2. Sánchez, E., et al., *The effect of different interference fits on the primary fixation of a cementless femoral component during experimental testing*. Journal of the mechanical behavior of biomedical materials, 2021. **113**: p. 104189.
3. Yang, H., et al., *Validation and sensitivity of model-predicted proximal tibial displacement and tray micromotion in cementless total knee arthroplasty under physiological loading conditions*. Journal of the Mechanical Behavior of Biomedical Materials, 2020. **109**: p. 103793.
4. Falkenberg, A., et al., *Determination of local micromotion at the stem-neck taper junction of a bi-modular total hip prosthesis design*. Medical engineering & physics, 2019. **65**: p. 31-38.
5. Engh, C.A., et al., *Quantification of implant micromotion, strain shielding, and bone resorption with porous-coated anatomic medullary locking femoral prostheses*. Clinical orthopaedics and related research, 1992(285): p. 13-29.
6. Kohli, N., J.C. Stoddart, and R.J. van Arkel, *The limit of tolerable micromotion for implant osseointegration: a systematic review*. Scientific Reports, 2021. **11**(1): p. 10797.
7. Berahmani, S., et al., *FE analysis of the effects of simplifications in experimental testing on micromotions of uncemented femoral knee implants*. Journal of Orthopaedic Research, 2016. **34**(5): p. 812-819.
8. Rapagna, S., et al., *Quantification of human bone microarchitecture damage in press-fit femoral knee implantation using HR-pQCT and digital volume correlation*. Journal of the mechanical behavior of biomedical materials, 2019. **97**: p. 278-287.
9. Kelly, N., et al., *An investigation of the inelastic behaviour of trabecular bone during the press-fit implantation of a tibial component in total knee arthroplasty*. Medical engineering & physics, 2013. **35**(11): p. 1599-1606.
10. Soltanihafshejani, N., et al., *Development of a crushable foam model for human trabecular bone*. Medical engineering & physics, 2021. **96**: p. 53-63.
11. Deshpande, V.S. and N.A. Fleck, *Isotropic constitutive models for metallic foams*. Journal of the Mechanics and Physics of Solids, 2000. **48**(6-7): p. 1253-1283.
12. Liu, Y.J. and B. Qiang. *A cyclic constitutive model for metallic foam*. in *Advanced Materials Research*. 2014. Trans Tech Publ.
13. Prime, M.B., *Anisotropic and pressure-dependent plasticity modeling for residual stress prediction*, in *Experimental and Applied Mechanics*, Volume 4. 2013, Springer. p. 415-427.
14. Skalomenos, K.A., G.D. Hatzigeorgiou, and D.E. Beskos, *Parameter identification of three hysteretic models for the simulation of the response of CFT columns to cyclic loading*. Engineering structures, 2014. **61**: p. 44-60.
15. Chong, D.Y., U.N. Hansen, and A.A. Amis, *Analysis of bone-prosthesis interface micromotion for cementless tibial prosthesis fixation and the influence of loading conditions*. Journal of biomechanics, 2010. **43**(6): p. 1074-1080.
16. Fitzpatrick, C.K., P. Hemelaar, and M. Taylor, *Computationally efficient prediction of bone-implant interface micromotion of a cementless tibial tray during gait*. Journal of biomechanics, 2014. **47**(7): p. 1718-1726.
17. Topoliński, T., et al., *Fatigue energy dissipation in trabecular bone samples with stepwise-increasing amplitude loading*. Materials Testing, 2011. **53**(6): p. 344-350.

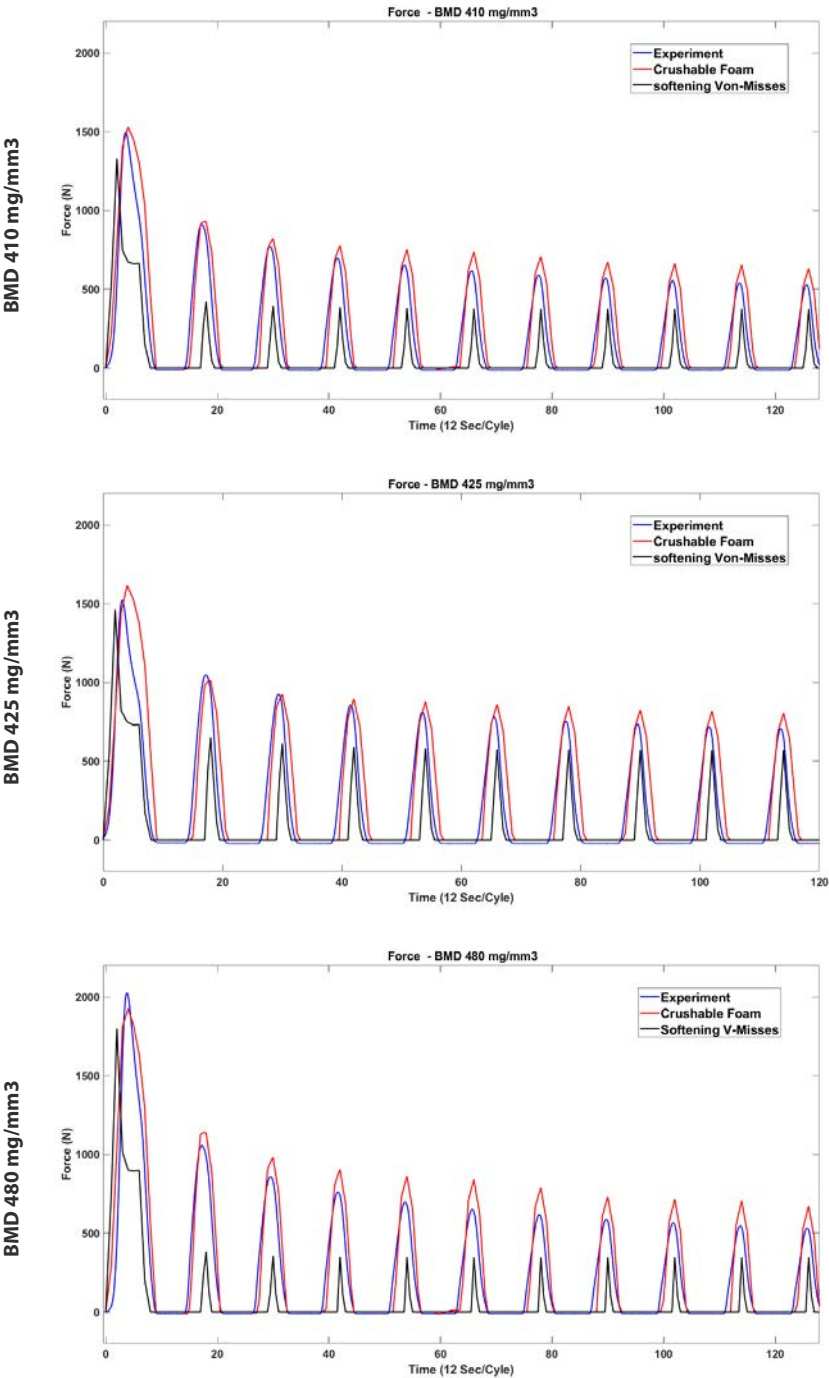
18. Pattin, C., W. Caler, and D. Carter, *Cyclic mechanical property degradation during fatigue loading of cortical bone*. Journal of biomechanics, 1996. **29**(1): p. 69-79.
19. Wolfram, U., H.-J. Wilke, and P.K. Zysset, *Damage accumulation in vertebral trabecular bone depends on loading mode and direction*. Journal of biomechanics, 2011. **44**(6): p. 1164-1169.
20. Soltanihafshejani, N., et al., *The application of an isotropic crushable foam model to predict the femoral fracture risk*. PLoS One, 2023. **18**(7): p. e0288776.
21. Eggermont, F., et al., *Effect of different CT scanners and settings on femoral failure loads calculated by finite element models*. Journal of Orthopaedic Research®, 2018. **36**(8): p. 2288-2295.
22. Caler, W.E. and D.R. Carter, *Bone creep-fatigue damage accumulation*. Journal of biomechanics, 1989. **22**(6-7): p. 625-635.
23. Xie, S., *Characterisation of time-dependent mechanical behaviour of trabecular bone and its constituents*. 2018.
24. Eggermont, F., et al., *Calibration with or without phantom for fracture risk prediction in cancer patients with femoral bone metastases using CT-based finite element models*. PLoS One, 2019. **14**(7): p. e0220564.
25. Kikinis, R., S.D. Pieper, and K.G. Vosburgh, *3D Slicer: a platform for subject-specific image analysis, visualization, and clinical support*, in *Intraoperative imaging and image-guided therapy*. 2013, Springer. p. 277-289.
26. Post, C.E., et al., *A FE study on the effect of interference fit and coefficient of friction on the micromotions and interface gaps of a cementless PEEK femoral component*. Journal of Biomechanics, 2022. **137**: p. 111057.
27. Kaneko, T.S., et al., *Relationships between material properties and CT scan data of cortical bone with and without metastatic lesions*. Medical engineering & physics, 2003. **25**(6): p. 445-454.
28. Soltanihafshejani, N., et al., *The Effect of Periprosthetic Bone Loss on The Failure Risk of Tibial Total Knee Arthroplasty*. Journal of Orthopaedic Research®, 2023.
29. Kelly, N., et al., *An experimental and computational investigation of the post-yield behaviour of trabecular bone during vertebral device subsidence*. Biomechanics and modeling in mechanobiology, 2013. **12**: p. 685-703.
30. Hamed, E., Y. Lee, and I. Jasiuk, *Multiscale modeling of elastic properties of cortical bone*. Acta mechanica, 2010. **213**(1-2): p. 131-154.
31. Wan, Q., et al., *The influence of body weight index on initial stability of uncemented femoral knee prostheses: A finite element study*. Heliyon, 2023. **9**(3).
32. Gundry, M., S. Hopkins, and K. Knapp, *A review on bone mineral density loss in total knee replacements leading to increased fracture risk*. Clinical Reviews in Bone and Mineral Metabolism, 2017. **15**: p. 162-174.
33. Jaroma, A., T. Soininvaara, and H. Kröger, *Periprosthetic tibial bone mineral density changes after total knee arthroplasty: a 7-year follow-up of 86 patients*. Acta orthopaedica, 2016. **87**(3): p. 268-273.
34. Shaw, C.N., et al., *Does the distribution and variation in cortical bone along lower limb diaphyses reflect selection for locomotor economy? Reconstructing mobility: Environmental, behavioral, and morphological determinants*, 2014: p. 49-66.
35. Kelly, N. and J.P. McGarry, *Experimental and numerical characterisation of the elasto-plastic properties of bovine trabecular bone and a trabecular bone analogue*. Journal of the mechanical behavior of biomedical materials, 2012. **9**: p. 184-197.

# Supplementary Data: The Effect of Bone Plasticity Models on Simulations of Primary Fixation in Total Knee Arthroplasty

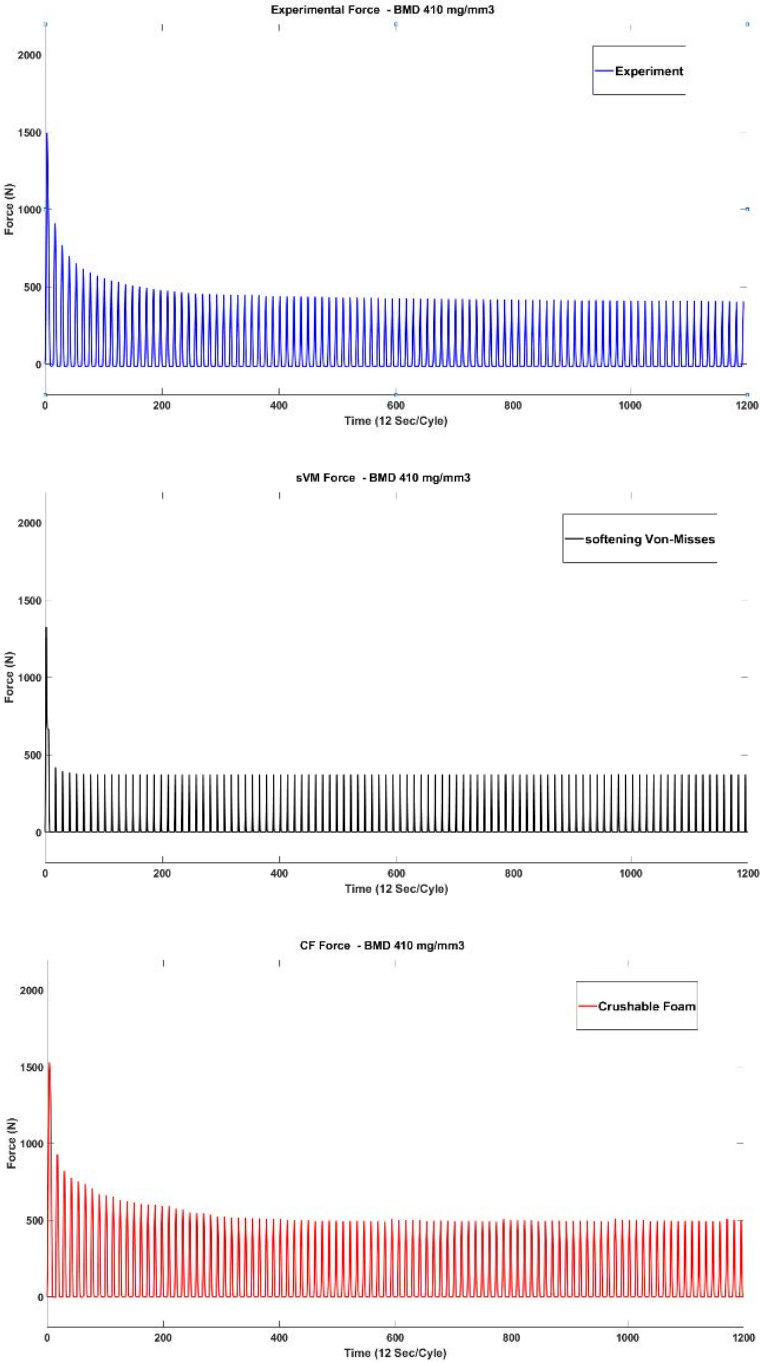
## Mechanical Degradation of Bone structure:



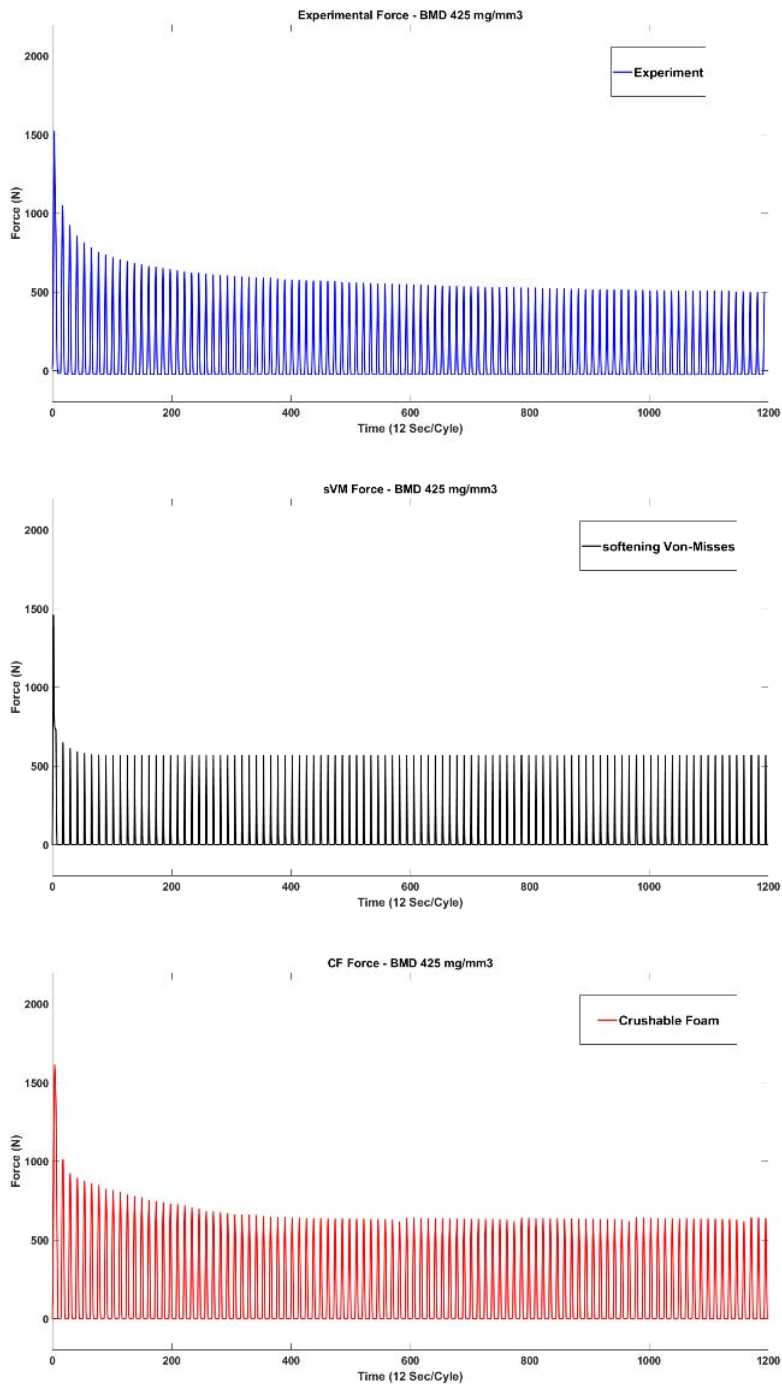
**Figure S 4-1** Force-displacement data of the three samples, both in experiment and in numerical simulations. The cyclic diagram of the work done by upper platen demonstrates a representation of the dissipated energy by bone samples.



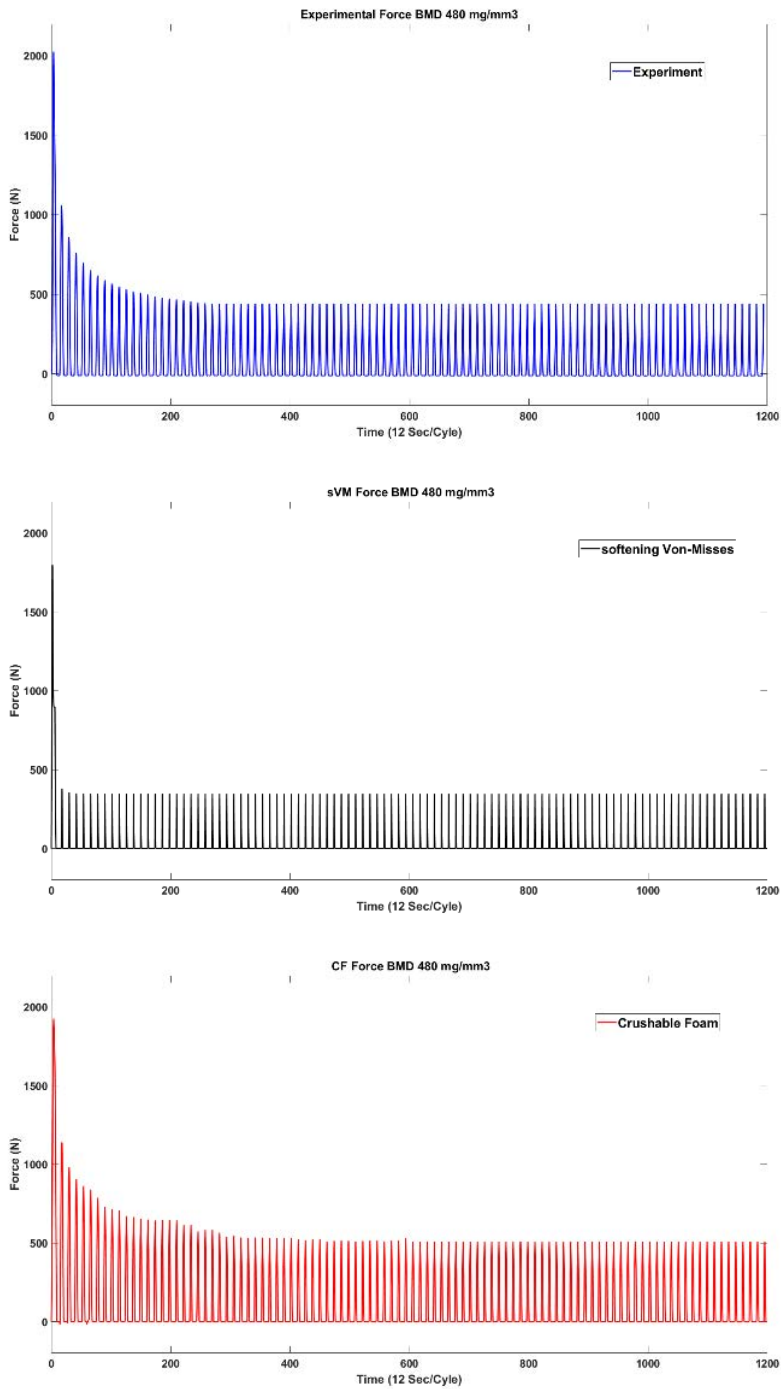
**Figure S 4-2** the first 10 cycle of Force-Time diagram for the three bone samples both in experiment and simulations.



**Figure S 4-3** Force-Time diagram illustrating 100 cycles for bone sample with BMD values of 410 mg/mm3 Force-Time diagram illustrating 100 cycles for bone sample with BMD values of 410 mg/mm3



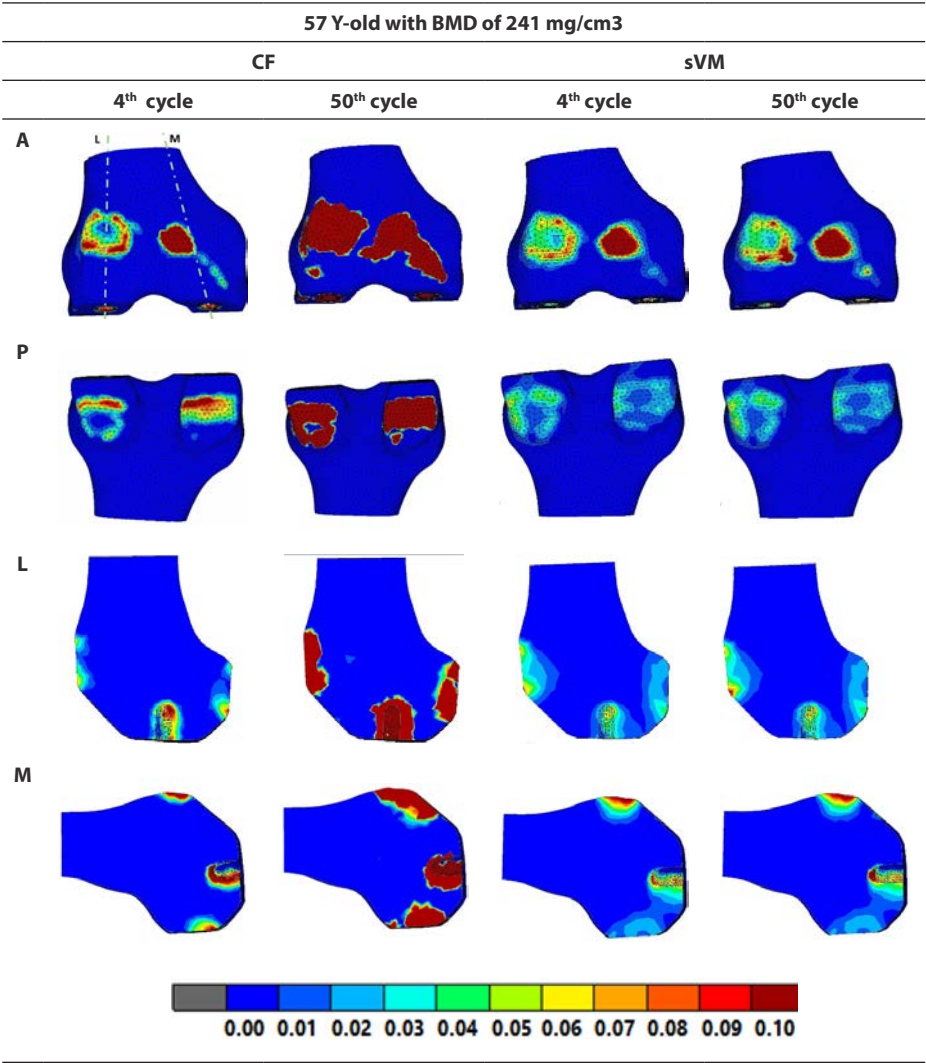
**Figure S 4-4** Force-Time diagram illustrating 100 cycles for bone sample with BMD values of 425 mg/mm<sup>3</sup>



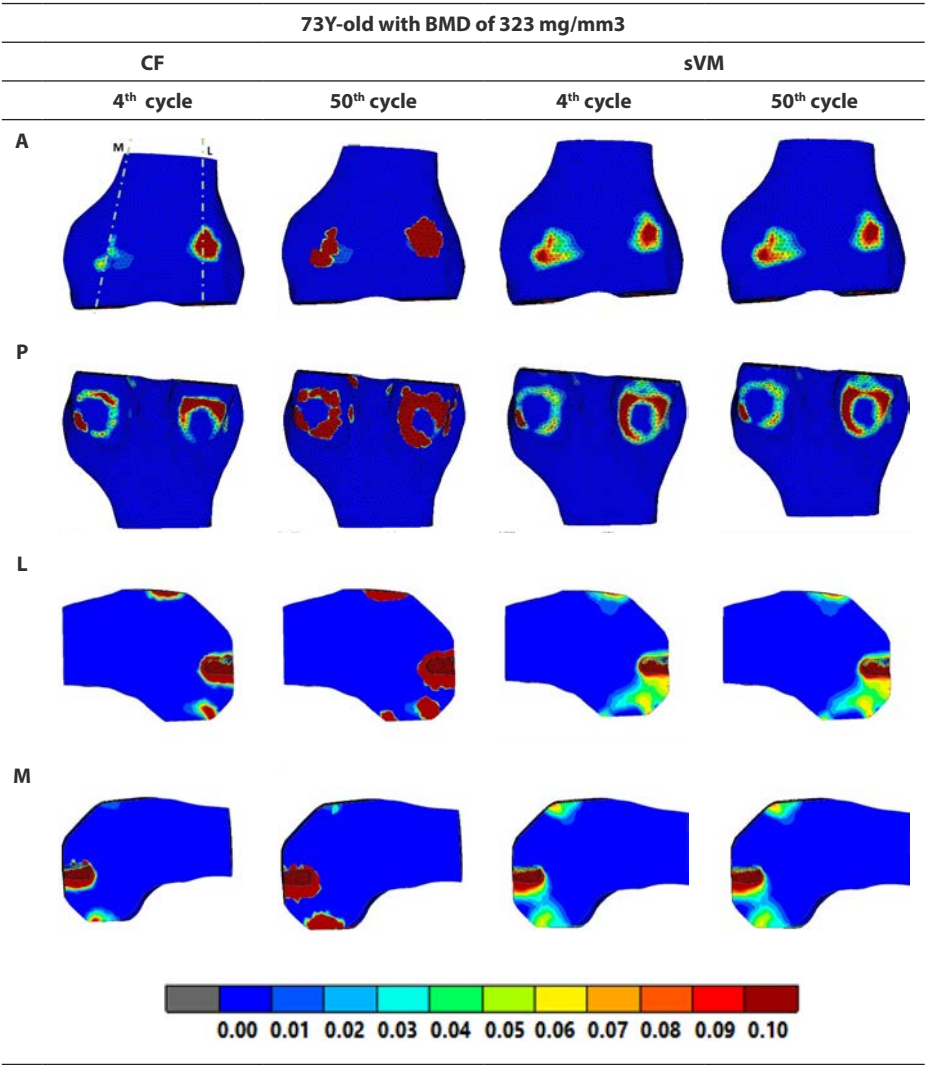
**Figure S 4-5** Force-Time diagram illustrating 100 cycles for bone sample with BMD values of 425 mg/mm<sup>3</sup>



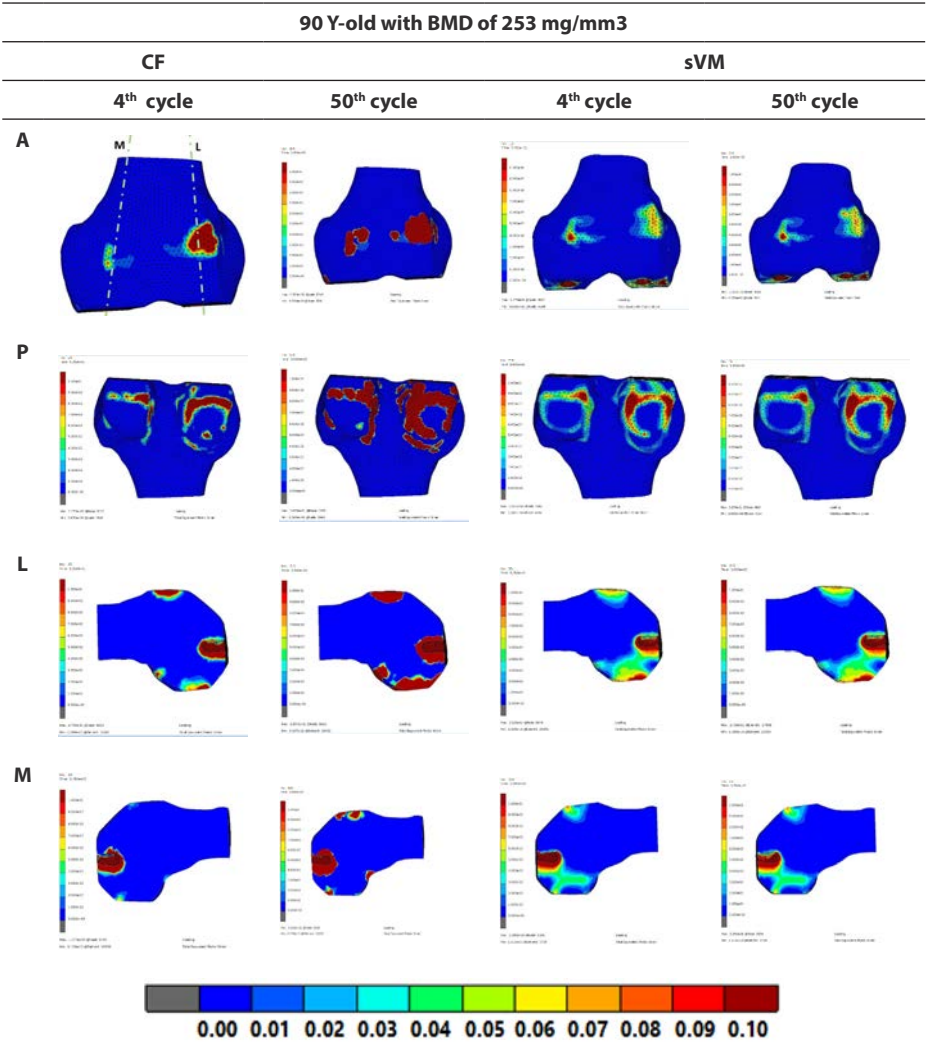
Distribution of Permanent deformation:



**Figure S 4-6.** The TEPS distribution at bone-implant interface for the 57Y-old femoral subject with BMD of 241 mg/cm3.

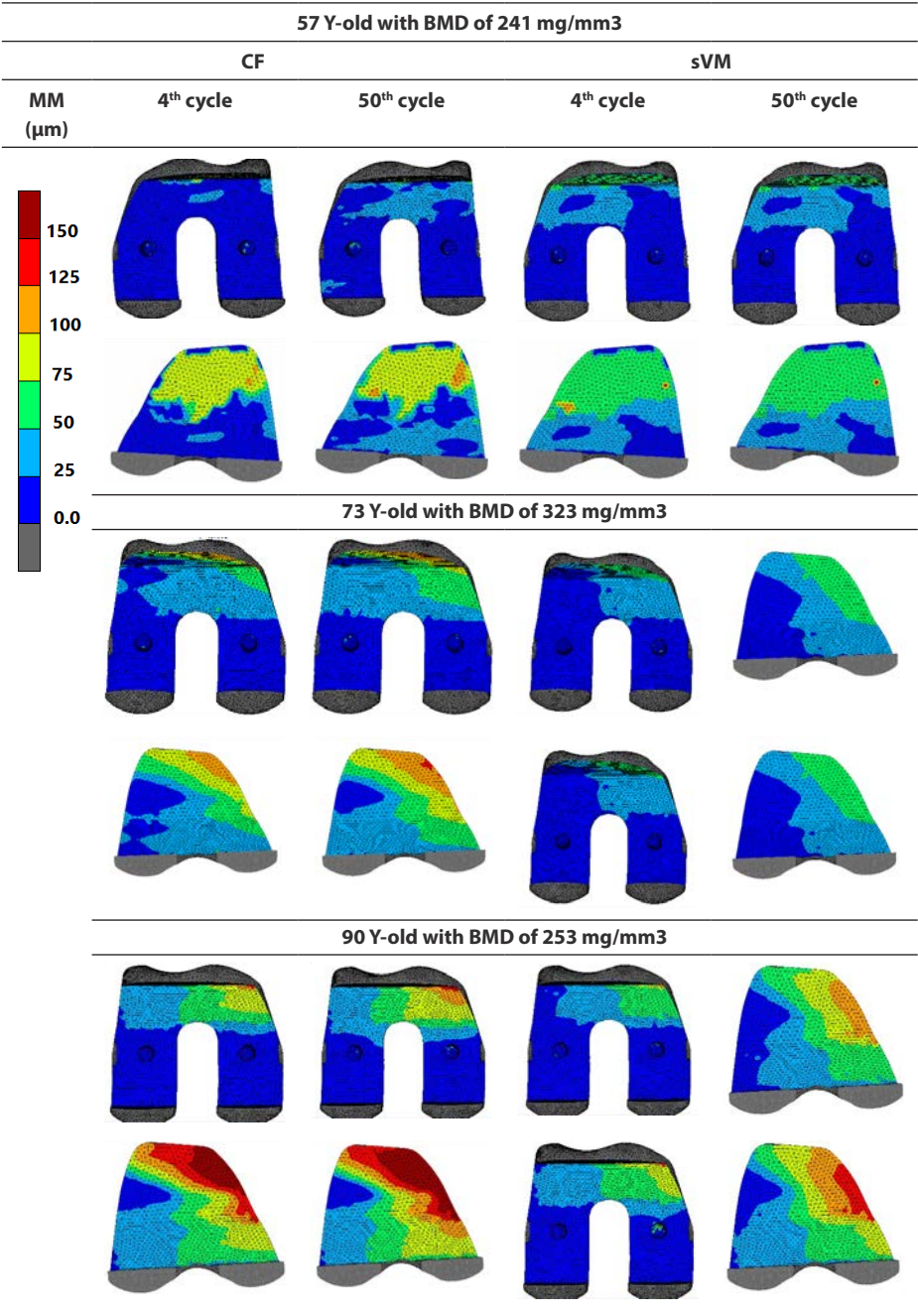


**Figure S 4-7** The TEPS distribution at bone-implant interface for the 73Y-old femoral subject with BMD of 323 mg/cm3.



**Figure S 4-8** The TEPS distribution at bone-implant interface for the 90Y-old femoral subject with BMD of 253 mg/cm3.

Distribution of Micromotion:



**Figure S 4-9** Resulting micromotion distribution at the implant interface at 4th and 50th loading cycle. Note that as the distribution of MM around pegs are less than 20 um it may not be visible in this contouring format.



## Chapter 5

# The Effect of Periprosthetic Bone Loss on The Failure Risk of Tibial Total Knee Arthroplasty

---

Navid Soltanihafshejani<sup>1,\*</sup>, Thom Bitter<sup>1</sup>, Nico Verdonschot<sup>1,2</sup>, Dennis Janssen<sup>1</sup>

<sup>1</sup> Radboud University Medical Center, Radboud Institute for Health Sciences, Orthopaedic Research Laboratory, 6500 HB Nijmegen, the Netherlands.

<sup>2</sup> University of Twente, Laboratory for Biomechanical Engineering, Faculty of Engineering Technology, 7500 AE Enschede, the Netherlands.

*Published in Journal of Orthopaedic Research on June 2023*

<https://doi.org/10.1002/jor.25642>



## Introduction

While total knee arthroplasty (TKA) is a popular and successful orthopaedic intervention, it does not provide a lifelong solution yet, particularly for younger patients, with aseptic loosening being one of the main reasons for revision[1]. Aseptic loosening is a complex multi-factorial process, in which loss of mechanical fixation plays an important role[2].

The mechanical integrity of the reconstruction is dependent on the quality of the periprosthetic bone supporting the implant. The bone quality can change after TKA due to changes in the bone stresses after placement of the metal components, resulting in changes in bone density, commonly referred to as bone remodeling [3]. Reports have shown that after TKA the bone mineral density (BMD) decreases underneath the tibial implant, particularly in the medial compartment [4-6]. Bone loss in this region may weaken the support of the tibial baseplate, which in extreme cases can lead to tibial collapse [7]. While the overall failure rate of TKA due to tibial collapse is low (0.3 - 0.6 %) [8-10], problems with bone loss may become more apparent with the expansion of the indication for surgery, with younger patients being operated on that will have their implant for a longer period of time.

Several studies examined the relation between bone quality (changes) and component migration (Sharkey et al., 2014, Gundry et al., 2017a, Linde et al., 2019, Linde et al., 2022). Linde et al. (2022) found minor changes in migration after an initial settling period as measured using RSA techniques, and a decreasing BMD after an initial phase of bone densification, as measured using DEXA. That study was unable to find a correlation between the maximum total point motion and the BMD changes. The potential impacts of periprosthetic bone loss on TKA failure have been recognized in previous literature (Berend et al., 2004, , Gundry et al., 2017, Ritter et al., 2014, Small et al., 2013) which illustrate that understanding of this relationship is crucial for improving the long-term success of TKA. Among the previous literature many studies have shown that the failure risk in the tibial implant following TKA is more associated with bone resorption than other factors and demonstrated that a decrease in BMD led to subsidence of the implant. Conversely, Ritter et al. (Ritter et al., 2014), Bergink et al. (Bergink et al., 2003) and (Arden et al., 1996) by studying more than 1500 fracture cases reported an increase in BMD prior to failure of TKA. This seems counterintuitive to be accounted for tibial implant failure, as it is more likely that a tibial implant would collapse due to weakened bone strength. This illustrates a need for clarification of the effect of bone resorption on TKA survival. The exact circumstances under which a tibial collapse occurs are largely unknown and

not well documented in the literature. While TKA reconstructions are perfectly able to withstand the forces acting on the knee joint during daily activities (e.g., gait, stair climbing, rising from a chair) [11], more excessive loads that occur during sudden impact events such as stumbling may lead to permanent damage and perhaps even a tibial collapse and subsequent gross failure of the reconstruction [10, 11].

Computational modeling using finite element analysis (FEA) can assist in assessing the failure risk of the reconstruction [12]. In designing and evaluating orthopedic implants, it is crucial to take into account the potential for plastic deformation of cancellous bone, which can result in implant migration and loosening. Understanding the bone response to both cyclic and static loading is important, as fatigue and large deformation effects both can contribute to implant failure [13-15]. However, this requires a suitable material model that realistically predicts the plastic failure processes occurring in the supporting bone. Our group recently developed an isotropic crushable foam (ICF) constitutive model capable of simulating the failure of tibial bone that can be used for such analyses.

The aim of this study was to investigate the relationship between bone resorption and the risk of failure of the tibial reconstruction in total knee arthroplasty (TKA), and to evaluate if finite element analysis (FEA) can simulate this relationship. Specifically, the study examined the effect of clinically relevant post-operative changes in bone mineral density (BMD) [16] on the risk of failure of tibial TKA, through the use of FEA models subjected to both physiological loading and a simulated stumbling event. The hypothesis of the study was that bone resorption following TKA increases the risk of tibial reconstruction failure, and that FEA with combination of using a proper material model can be used to predict this risk.

## Methods

### Three-dimensional models

Two proximal tibiae of a male (65 years, 85 kg) and female (90 years, 65 kg) subject representing cases with good and poor initial bone quality, respectively, were QCT scanned (Toshiba Medical Systems, Tokyo, Japan; voxel size 0.6×0.4×0.4 mm, 120 kV, 260 mA). The tibiae were scanned along with solid calibration phantoms (Image Analysis, Columbia, KY) to compute local BMD [17]. Three-dimensional models of the proximal tibiae were created in 3D Slicer (Open Source Software, [18]). Optical scans of various sizes of the Triathlon tibial component (manufactured by Stryker Orthopaedics) were provided. The appropriate size of the implant for each



patient was selected based on anthropometric measures, and a CAD model of the selected implant was created. A cement layer with a thickness of 2 mm was created underneath the tibial tray [19]. The geometry of the proximal tibia was resected following mechanical alignment surgical guidelines, to ensure the tibial component is implanted in a neutral position, meaning the resected plateau of the tibia was perpendicular to its mechanical axis (**Figure 5-1a**).

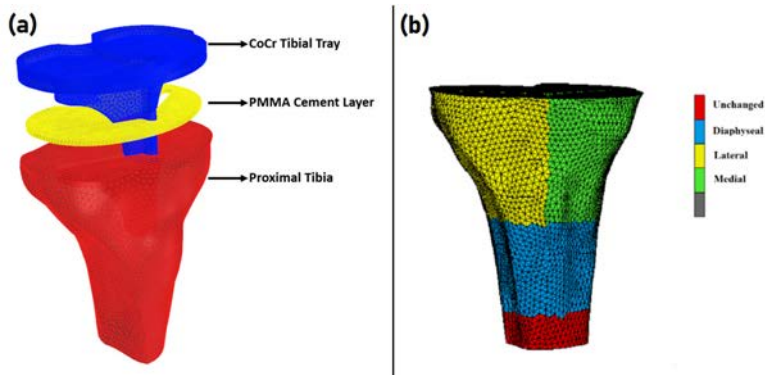
**Finite Element Model**

3D models of the implanted proximal tibias were meshed using 4-noded tetrahedral elements in Hypermesh (Altair Engineering, Troy, MI) and imported into the FEA software (Marc/Mentat 2021, MSC. Software Corporation, Santa Ana, CA). The bone was considered as a heterogeneous elastoplastic material in which the mechanical properties of each element were computed based on the calibrated BMD values. Elastic material properties were assigned to the Cobalt-Chromium (CoCr) tibial tray and the Polymethylmethacrylate (PMMA) cement layer (**Table 4-2**). A fully-bonded interaction was considered between bone and cement, and between the implant and cement, while a frictional touching contact with coefficient friction of 0.4 was assumed between the bone and keel of the tibial component [19]. A mesh convergence study was performed using the intact tibial bone with element sizes in the range of 4.5, 4, 3, 2.5 and 2 mm to define the appropriate element size. For element sizes smaller than 3mm, the difference in strain energy was less than 10 % [20] which was selected as the target size. Numerical simulations were performed using a nonlinear elastoplastic ICF model (**Table 4-2**; for detailed information about this ICF model see [12].

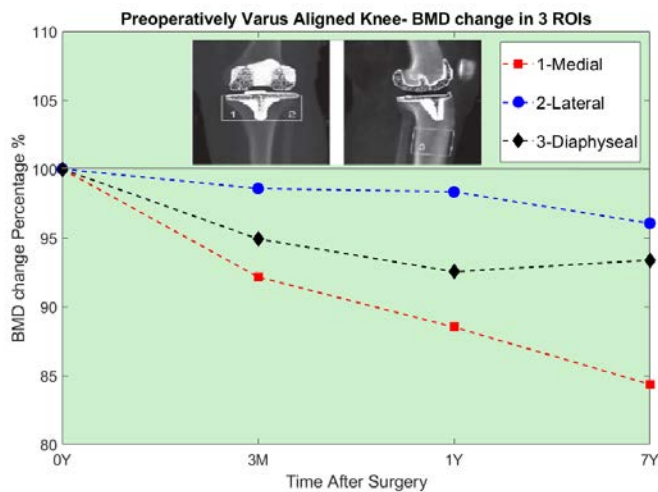
**Table 5-1** Mechanical properties of the materials used in the FEA models [12, 21]

Non-linear elastoplastic behavior dependent on BMD([mg/mm3])			
Material	ICF		
	Young's modulus	Yield Stress	<i>K</i> parameter (strength ratio)
			$K = 2.993, BMD \leq 0.08$
Trabecular bone ( $BMD \leq 0.95$ )	$5113\rho_{BMD}^{1.654}$	$79.36\rho_{BMD}^{1.553}$	$K = 1.361\rho_{BMD}^{-0.312},$ $0.08 < BMD \leq 0.95$
Cortical bone ( $BMD > 0.95$ )	$13750\rho_{BMD}^{2.429}$	$111.5\rho_{BMD}^{1.800}$	$K = 1.383, BMD > 0.95$
Linear elastic behavior			
Material	Young modulus (MPa)		Poisson's ratio
CoCr	210,000		0.3
PMMA	2,100		0.3

To simulate bone resorption in a medium-term follow up TKA, the equivalent BMD values of the tibiae were adjusted according to clinical follow-up data. The change in BMD of 69 pre-operatively varus aligned knees was reported by Jaroma et al. [16] during a 7 year follow-up period after TKA (**Figure 5-2**). The BMD values were reported for three regions of interests (ROIs) in the proximal tibia (medial, lateral and diaphyseal), at surgery (0 months), and 3 months, and 1 and 7 years after surgery. The change in BMD was applied accordingly to the trabecular regions of the QCT-based FEA models ( $\text{mg}/\text{mm}^3$ ). To represent the worst-case scenario the minimum density value at each time point was selected for analysis. **Figure 5-1b** shows the representation of the ROIs in the FEA model.



**Figure 5-1** A schematic view of the proximal tibia, cement layer and implant (a) and selection of the regions of interest in the computer model (b)

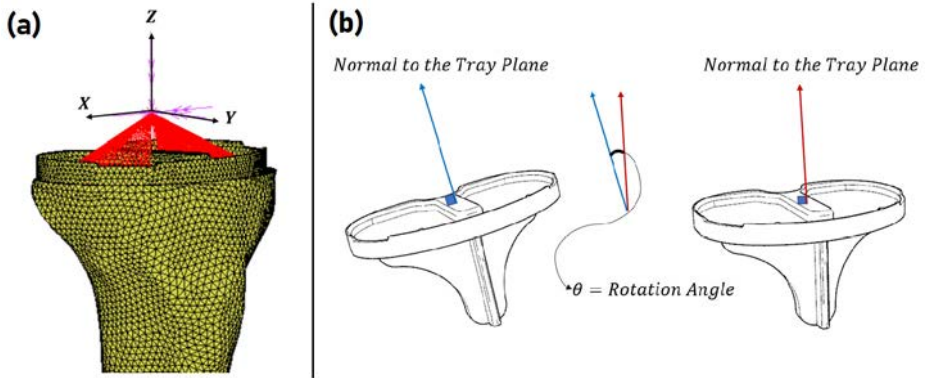


**Figure 5-2** percentage change in BMD in implanted proximal tibia, adapted from [16]

To simulate the permanent deformation of the tibiae due to a stumbling event, first the model was pre-conditioned through cyclic loading with a gait loading regime. The repetitive loading was continued until hysteresis in the model was minimized and a steady state of plastic deformation was reached [14, 22, 23]. To determine the number of cycles required to achieve a steady state, the load was repeated for 200 cycles. If change in the number of yielded integration points deviated less than one percent, the number of loading cycles was considered sufficient. After the pre-conditioning phase a stumble load (biased at the medial side) was applied to the model, representing an incident with excessive but still physiological loads. In order to confirm the model's ability to accurately account for deviations in incident loads, we adjusted the parameter for stumbling load from medial to lateral. This adjustment was made to represent the scenario where an unexpected event affects the lateral side. The gait and stumble loads were applied to a point located centrally at a level 10 mm above the tibial tray (**Figure 5-3a**), following the origin of the Orthoload dataset [24]. The central loaded point was linked to the tibial surface tray based on the projection of the distal femoral condyle onto the tibial tray. **Table 5-2** shows the force and moment components for both loading conditions. For gait, the peak load was taken based on standard loads acting on the knee [24], while for the stumbling load, these values were multiplied by a factor of 3.46, based on measurements of the hip joint during an actual stumbling event [11]. The distal part of the tibia was fixed in all directions. As a measure of failure of the tibial component, the angular deviation of the normal vector of the tibial tray from the initial orientation was calculated after unloading the model and taken as the tibial migration (**Figure 5-3b**). A threshold of 10° was considered a gross failure due to tibial collapse [10], while a rotation of the tibial component of less than 3° was assumed to be in the safe margin [8].

**Table 5-2** Applied loads to the center point above the tibial tray [11, 24].

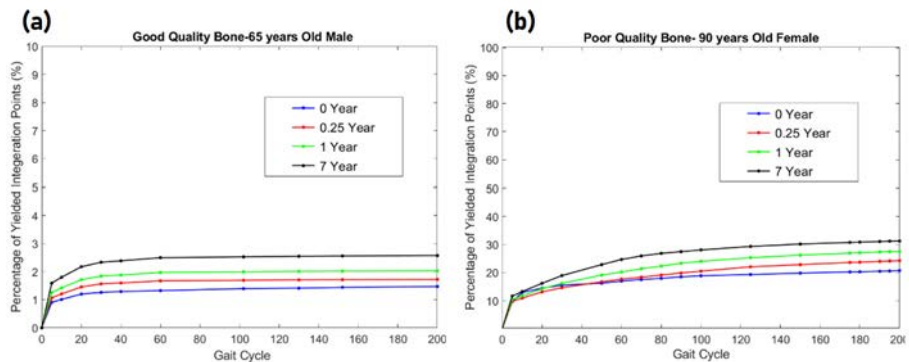
Applied Loads						
Load	Fx (BW)	Fy (BW)	Fz (BW)	Mx (BW.mm)	My (BW.mm)	Mz (BW.mm)
Gait	-0.1	-0.15	-2.61	19	-10	-5
Stumbling (Medial Biased)	-0.346	-0.519	-9.03	65.74	-34.6	-17.3
Stumbling (Lateral Biased)	-0.346	-0.519	-9.03	65.74	+34.6	-17.3



**Figure 5-3** a) Location of the center point above tibial tray in local coordinates, b) Rotation angle of the tibial tray

## Results

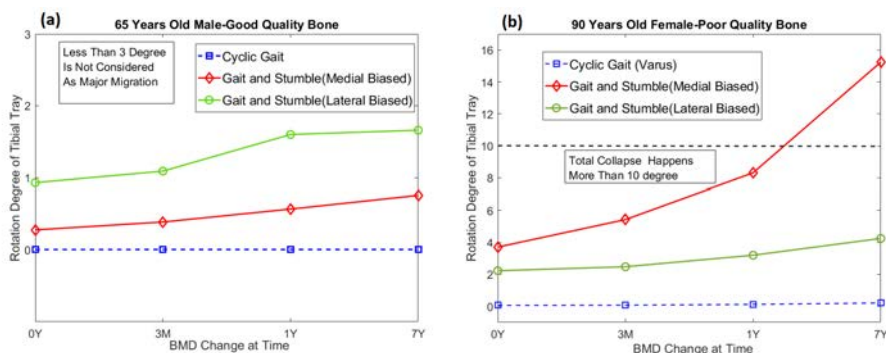
Applying the peak load for 200 cycles initially resulted in an increasing number of yielded nodes, followed by a steady state in which the percentage of yielded nodes increased only marginally. In the model with good quality bone (65y old, BMD 219 mg/mm<sup>3</sup>), after 10 cycles the increase of yielded nodes was less than 1%, which reduced to 0.1% after 60 cycles (**Figure 5-4 a**), which was similar for all post-operative time points (0, 3m, 1yr, 7yrs). In the model with weak bone (90y old, BMD 130 mg/mm<sup>3</sup>), a significant amount of plastic deformation was noticed. In this model, only after 150 cycles the incremental increase in yielded nodes was less than 1%, which was further reduced to 0.1% after 190 cycles for the weak bone (**Figure 5-4 b**).



**Figure 5-4** Percentage of yielded integration points for 200 cycles of gait peak load in a pre-aligned varus tibia of a 65-year-old male (a) and a 90-year-old female (b). Note the difference in the scale of the vertical axes.

Based on the initial results, both the strong and weak tibia models were pre-conditioned with 150 gait cycles to ensure a steady state of plastic deformation in both cases before applying the stumbling load.

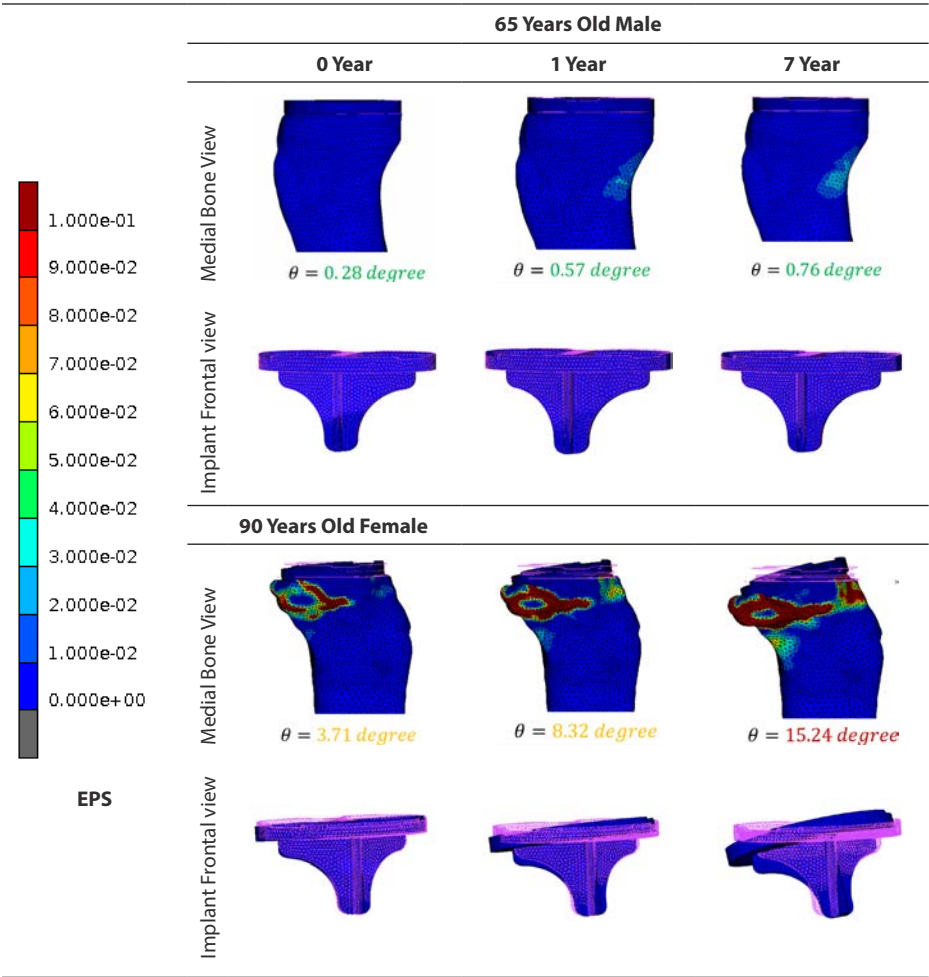
As shown in **Figure 5-5**, for both tibias no prominent migration occurred after the cyclic peak gait loading, at none of the simulated cases of post-operative bone loss. After application of the stumbling load biased toward medial side, for the strong bone, the rotational migration of the tibial component remained less than  $1^\circ$  for all post-operative time points. However, for the weak bone the tibial migration increased with post-operative BMD loss, ranging from  $3.7^\circ$  directly postoperatively to  $15.2^\circ$  at 7 years. To explore the effect of variations in the loading configuration, additional simulations were performed in which the stumbling load was biased towards the lateral side. In the model with the 65-year-old male implant migration was between  $1$  and  $2^\circ$  for this load, and remained below the major migration threshold of  $3^\circ$ . For the model of the 90-year-old female the rotational migration was between  $2$  and  $4.3^\circ$ , which was lower than for the medial load case and also below the threshold for total collapse ( $10^\circ$  - Figure 5).



**Figure 5-5** The rotation angle of tibial tray of **a)** 65 years old male (strong bone) and **b)** 90 years old female (weak bone). Note the difference in the scale of the vertical axes.

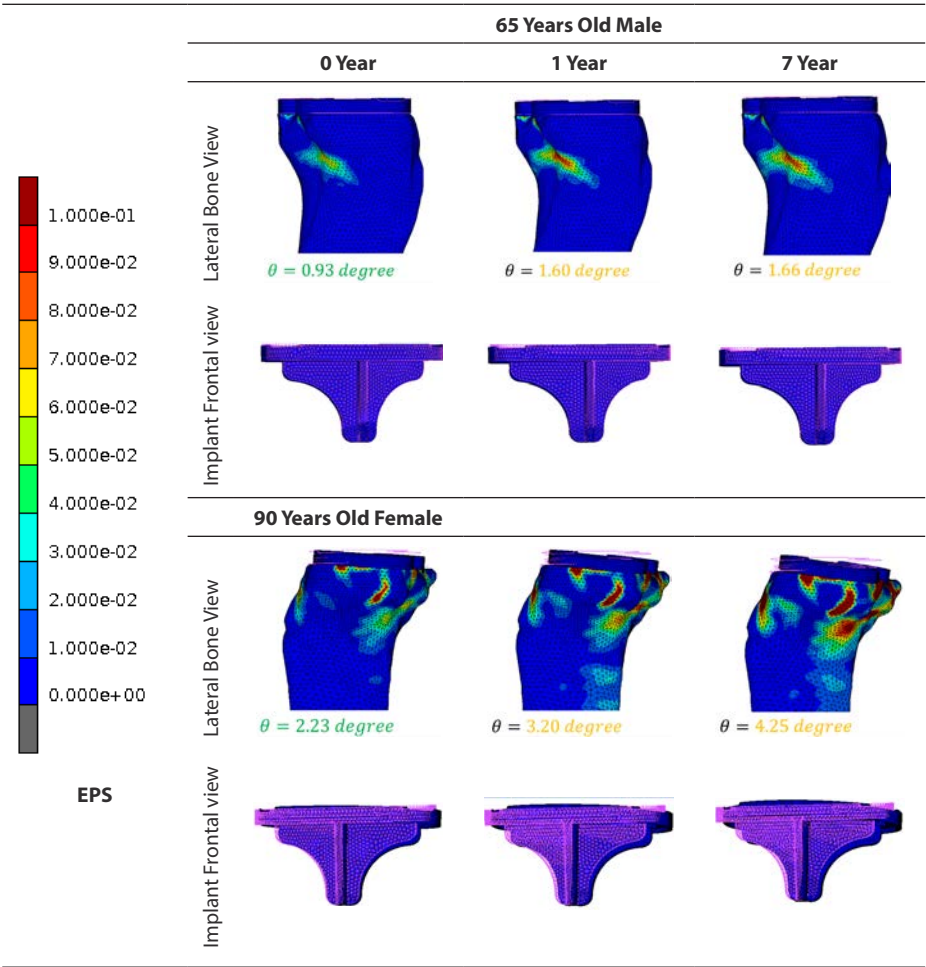
**Table 5-3** shows the distribution of Equivalent of Plastic Strain (EPS) after applying the tumble load, for both tibias with the simulated BMD loss at 0, 1 and 7 years. Peak plastic strains were mainly seen at the medial side. In the strong tibia (good quality bone) no plastic strain was seen directly postoperatively, while with a bone loss at 7 years post-operatively some plastic deformation was noticed in the medial cortex. For the weak bone, substantial plastic strains were seen already directly postoperatively, which increased significantly with the post-operative time (and decreasing BMD).

**Table 5-3** EPS distribution at the medial compartment of proximal tibiae as demonstration of the permanent deformation in stumbling load biased toward medial side.



**Table 5-4** illustrates the distribution of EPS resulting from the application of a lateral-biased stumbling load to both tibias with simulated BMD loss at 0, 1, and 7 years. The largest plastic strains were observed at the lateral side. For the strong tibia with good quality bone, some plastic strain was noticed right after the surgery, but there was no significant implant migration. In the case of weak bone, substantial plastic strains were observed directly after surgery, which increased as the post-operative time progressed (and BMD decreased). Although implant migration was seen, a total collapse (rotation larger than 10°) was not observed at any of the time points.

**Table 5-4** EPS distribution at the Lateral compartment of proximal tibiae as demonstration of the permanent deformation after stumbling load biased on lateral side.



Discussion

The aim of the current paper was to investigate the effect of bone resorption on the failure of the tibial reconstruction in TKA. Bone density changes representing the clinical situation between 0 and 7 years postoperatively were simulated in two FEA models with good and poor initial bone quality. While in a good quality bone the peri-prosthetic bone loss did not lead to a substantial increase in implant migration, initial poor bone quality and additional simulated post-operative bone loss had a substantial effect on the stability of the tibial implant.



The distribution of plastic strains at medially biased stumbling load, showed that in the poor bone quality model the deformations mainly occurred in the medial compartment, with a migration that clinically would be interpreted as a medial tibial collapse. On the lateral side, bone failure was less pronounced, which may have been related to the reduced bone loss that was simulated in that compartment based on the clinical data [16], and the reduced load on the lateral compartment. The stumbling load biased towards the lateral compartment compromised the reduced load on the lateral side. However, the results indicate that even if the loads are more biased towards the lateral side, total collapse may not occur laterally. This finding is consistent with tibial failure situations, which mostly occur on the medial side. The extent of tibial migration was maximal at 7 years postoperatively, in line with the progression of bone loss.

Periprosthetic changes to bone density after TKA have been investigated widely in clinical studies [4-6, 9, 25]. The study of Jaroma et al. [16] provided a detailed description of these changes, allowing to investigate bone changes at different time points postoperatively. Although in the simulations the BMD change was only applied to the trabecular regions, the actual change may also partially involve the cortical bone. Moreover, the measured bone density changes were applied to relatively large regions of interest, while the density changes may be distributed differently over the ROIs.

While the current study shows that failure of the tibial tray may be related to periprosthetic bone resorption, Ritter et al. [9] actually showed an increase in bone density in patients that experienced a medial tibial collapse, based on knee radiographs. Other studies have suggested that an increase in BMD may occur before the failure of total knee arthroplasty (TKA), independent of medial tibial collapse [26, 27]. Those findings are also in contradiction with numerous DEXA studies that reported decreasing values of BMD prior to the collapse [3, 4, 6, 8, 25, 28, 29]. This discrepancy may be due to differences between radiographs and DEXA scans in the ability to measure BMD changes. One potential explanation could be that the participants in the study conducted by Ritter et al. had already undergone a gradual collapse of the tibia, which could have stimulated localized fracture repair reactions and led to increased levels of osteoblast activity. Alternatively, other studies have specifically examined the effects of osteoarthritis and osteoporotic bone which could have potential impact on the results.

The current simulations used an ICF model to capture the post-yield behavior of the tibiae [12]. As the ICF model incorporates an updating yield criterion, to avoid



overestimation of the bone strength, a repetitive loading configuration was applied to model damage accumulation in the bone as a pre-conditioning treatment [30, 31]. To ensure model equilibrium prior to the analysis of the stumbling event, a steady state of yielded bone was defined after cyclic loading using repetitive gait cycles. This allowed us to capture progressive yielding of the tibiae behavior, resulting in accumulated damage and failure with large plastic strains[14, 32].

To determine the appropriate number of repetitive cycles, both tibiae were subjected to 200 cycles of normal gait loading. While decreasing the BMD resulted in larger yield areas for both models, the level of steady state plasticity remained almost unchanged for all the cases, both for the strong (around 10 cycles, **Figure 5-4a**) and the weak bone (150 cycles, **Figure 5-4b**). As the weak bone required 150 gait cycles to reach a steady state of plasticity, this number was used for both tibiae prior to applying the stumbling load. No distinct migration of the tibial tray was seen directly after the cyclic gait loading (for all post-operative time points), confirming the models predicted no risk of failure due to level walking [11].

Applying the stumbling load biased toward medial side resulted in tibial migration in both the strong ( $0.3^{\circ} - 0.8^{\circ}$ ) and weak bone ( $3.7^{\circ} - 15.2^{\circ}$ ) (**Table 5-3**). Hence, for the strong bone the subsidence remained below  $1^{\circ}$  for all cases with no risk of tibial collapse. For the weak bone, however, tibial migration exceeded the  $10^{\circ}$  threshold at 7 years postoperatively, indicating a tibial collapse. At earlier timepoints the tibial migration was already substantial, as rotations of more than  $3^{\circ}$  (low-level migration) are considered hazardous for vulnerable patients [8]. To investigate the effect of loading variations on bone failure and implant migration the models were also loaded with a stumbling load with a lateral bias. In both models the migration of the tibial tray did not exceed the  $10^{\circ}$  threshold, demonstrating the sensitivity of the results to the orientation of the applied loads. This stresses the importance of analyzing the effect of including variability to make the predictions more robust. This may also include the variations in muscle forces, as these may also significantly affect the joint loads. As early migration of the tibial implant can be an indication for increased risk of failure [19], pre-operative planning and selection of implant design based on bone quality is essential, and may be informed by a computational model.

Several clinical studies [33-35] have shown an early phase of implant migration, which levels off after 1 and 2 years. In contrast, our FEA study did not reflect this pattern in the low bone quality model. This discrepancy could be attributed to several factors. First, clinical measurements (e.g., radio stereometric analysis) provide a direct assessment of implant migration *in vivo*, including an initial

settling phase that may be influenced by factors such as level of activity, rehabilitation regime, or biological response to the surgery, which are not included in our mechanical model. Moreover, we simulated a case of extreme bone loss in a subject with an already poor baseline bone quality. As such, our model may be more representative of an individual case that has an elevated risk of failure, rather than a representative case of the majority of patients undergoing a TKA procedure. Therefore, broader investigations with a larger number of models reflecting the actual patient population (including its variability) are required to further explore the mechanisms underlying early migration of tibial implants and the role of bone quality.

Our study has several limitations that should be considered. First, the FEA models were not validated against experimental results. The material model used in our study, however, was previously validated against experimental findings of human trabecular bone [12] and now extended with the cortical bone data adapted from Kaneko et al. [21]. Second, the change in BMD applied to the models was not related to the implant used in the current study but was based on clinical data of 86 patients implanted with 4 different prostheses. Hence, BMD changes could be different for this particular implant and tibiae used in the current study. Third, we reported the angular deviation of the tibial components, which may not be fully representative of tibial migration. However, angular measurements in the anatomical planes are widely accepted in clinical studies [10]. Finally in this study, a constant percentage of bone mineral density (BMD) change was used for all regions of interest (RIOs) since the data source did not provide localized information. While this may not capture localized changes in BMD, the selected RIOs in the study of Jaroma et al. [16] were chosen as representative areas for a general overview of BMD changes. In future work, we intend to extend the simulations to a larger population of models to obtain more robust insights into the failure risk of tibial TKA.

## Conclusion

In conclusion, the current study investigated the effect of periprosthetic bone resorption on failure of a tibial TKA using a bone material model simulating progressive yielding. The study demonstrates the feasibility of simulating the collapse of the tibial reconstruction in TKA after long-term peri-prosthetic bone loss. A stumbling load triggered the failure process of the reconstruction in case of poor initial bone quality and was even more pronounced with additional simulated post-operative bone loss.

While the findings of our study cannot be directly extrapolated to other implant designs, the approach presented here can be used to evaluate TKA components. Our study provides insights into the potential failure mode of TKA implants due to periprosthetic bone loss, which can inform the implant design process and the selection of implants tailored to specific patient groups. From a clinical perspective, our study highlights the importance of monitoring and managing periprosthetic bone loss in TKA patients to ensure long-term implant survival. Ultimately, our research aims to improve clinical outcomes and enhance the quality of life of TKA patients.

**Conflict of interest statement**

All authors declare no conflict of interest.

**Acknowledgments**

The authors declare that the research was conducted in the absence of any commercial or financial relationships that could be construed as a potential conflict of interest.

## References

1. Association, A.O., *Australian Orthopaedic Association national joint replacement registry: annual report*. Adelaide: Australian Orthopaedic Association national joint replacement registry, 2016.
2. Mathis, D.T. and M.T. Hirschmann, *Why do knees after total knee arthroplasty fail in different parts of the world?* Journal of Orthopaedics, 2021. **23**: p. 52-59.
3. Completo, A., F. Fonseca, and J. Simoes, *Strain shielding in proximal tibia of stemmed knee prosthesis: experimental study*. Journal of biomechanics, 2008. **41**(3): p. 560-566.
4. Gundry, M., S. Hopkins, and K. Knapp, *A review on bone mineral density loss in total knee replacements leading to increased fracture risk*. Clinical reviews in bone and mineral metabolism, 2017. **15**(4): p. 162-174.
5. Levitz, C.L., P.A. Lotke, and J.S. Karp, *Long-term changes in bone mineral density following total knee replacement*. Clinical orthopaedics and related research, 1995(321): p. 68-72.
6. Small, S., et al., *Changes in tibial bone density measured from standard radiographs in cemented and uncemented total knee replacements after ten years' follow-up*. The bone & joint journal, 2013. **95**(7): p. 911-916.
7. Park, H.J., et al., *A three-dimensional finite element analysis on the effects of implant materials and designs on periprosthetic tibial bone resorption*. PLoS One, 2021. **16**(2): p. e0246866.
8. Berend, M.E., et al., *The Chetranjan Ranawat Award: Tibial Component Failure Mechanisms in Total Knee Arthroplasty*. Clinical Orthopaedics and Related Research (1976-2007), 2004. **428**: p. 26-34.
9. Ritter, M., et al., *Trabecular bone density of the proximal tibia as it relates to failure of a total knee replacement*. The bone & joint journal, 2014. **96**(11): p. 1503-1509.
10. Fehring, T.K., et al., *Catastrophic varus collapse of the tibia in obese total knee arthroplasty*. The Journal of arthroplasty, 2017. **32**(5): p. 1625-1629.
11. Zimmerman, W.F., et al., *Damage in total knee replacements from mechanical overload*. Journal of biomechanics, 2016. **49**(10): p. 2068-2075.
12. Soltanihafshejani, N., et al., *Development of a crushable foam model for human trabecular bone*. Medical engineering & physics, 2021. **96**: p. 53-63.
13. Taylor, M. and K. Tanner, *Fatigue failure of cancellous bone: a possible cause of implant migration and loosening*. The Journal of Bone and Joint Surgery. British volume, 1997. **79**(2): p. 181-182.
14. Hosseini, H.S., D.H. Pahr, and P.K. Zysset, *Modeling and experimental validation of trabecular bone damage, softening and densification under large compressive strains*. Journal of the mechanical behavior of biomedical materials, 2012. **15**: p. 93-102.
15. Zimmermann, E., B. Busse, and R. Ritchie, *The fracture mechanics of human bone: influence of disease and treatment*. Bonekey Rep. 2015; 4: 743. 2015.
16. Jaroma, A., T. Soininvaara, and H. Kröger, *Periprosthetic tibial bone mineral density changes after total knee arthroplasty: a 7-year follow-up of 86 patients*. Acta orthopaedica, 2016. **87**(3): p. 268-273.
17. Derikx, L.C., et al., *Implementation of asymmetric yielding in case-specific finite element models improves the prediction of femoral fractures*. Computer methods in biomechanics and biomedical engineering, 2011. **14**(02): p. 183-193.
18. Kikinis, R., S.D. Pieper, and K.G. Vosburgh, *3D Slicer: a platform for subject-specific image analysis, visualization, and clinical support*, in *Intraoperative imaging and image-guided therapy*. 2014, Springer. p. 277-289.

19. Wong, J., et al., *Predicting the effect of tray malalignment on risk for bone damage and implant subsidence after total knee arthroplasty*. Journal of Orthopaedic Research, 2011. **29**(3): p. 347-353.
20. Costa, M., et al., *Biomechanical assessment of vertebrae with lytic metastases with subject-specific finite element models*. Journal of the mechanical behavior of biomedical materials, 2019. **98**: p. 268-290.
21. Kaneko, T.S., et al., *Relationships between material properties and CT scan data of cortical bone with and without metastatic lesions*. Medical engineering & physics, 2003. **25**(6): p. 445-454.
22. Hosseini, H.S., A.L. Clouthier, and P.K. Zysset, *Experimental validation of finite element analysis of human vertebral collapse under large compressive strains*. Journal of biomechanical engineering, 2014. **136**(4).
23. Dong, X.N., et al., *Orientation dependence of progressive post-yield behavior of human cortical bone in compression*. Journal of biomechanics, 2012. **45**(16): p. 2829-2834.
24. Bergmann, G., et al., *Standardized loads acting in knee implants*. PloS one, 2014. **9**(1): p. e86035.
25. Georgeanu, V., T. Atasiei, and L. Gruionu, *Periprosthetic Bone Remodelling in Total Knee Arthroplasty*. Maedica, 2014. **9**(1): p. 56.
26. Arden, N., et al., *The association between osteoarthritis and osteoporotic fracture: the Chingford Study*. Rheumatology, 1996. **35**(12): p. 1299-1304.
27. Bergink, A.P., et al., *Osteoarthritis of the knee is associated with vertebral and nonvertebral fractures in the elderly: the Rotterdam Study*. Arthritis Care & Research: Official Journal of the American College of Rheumatology, 2003. **49**(5): p. 648-657.
28. Sharkey, P.F., et al., *Why are total knee arthroplasties failing today—has anything changed after 10 years?* The Journal of arthroplasty, 2014. **29**(9): p. 1774-1778.
29. Zhang, Q.-H., A. Cossey, and J. Tong, *Stress shielding in periprosthetic bone following a total knee replacement: effects of implant material, design and alignment*. Medical engineering & physics, 2016. **38**(12): p. 1481-1488.
30. Leng, H., X.N. Dong, and X. Wang, *Progressive post-yield behavior of human cortical bone in compression for middle-aged and elderly groups*. Journal of biomechanics, 2009. **42**(4): p. 491-497.
31. Topoliński, T., et al., *Study of the behavior of the trabecular bone under cyclic compression with stepwise increasing amplitude*. Journal of the mechanical behavior of biomedical materials, 2011. **4**(8): p. 1755-1763.
32. Wolfram, U., H.-J. Wilke, and P.K. Zysset, *Damage accumulation in vertebral trabecular bone depends on loading mode and direction*. Journal of biomechanics, 2011. **44**(6): p. 1164-1169.
33. Linde, K.N., et al., *Preoperative systemic bone quality does not affect tibial component migration in knee arthroplasty: A 2-year radiostereometric analysis of a hundred consecutive patients*. The Journal of arthroplasty, 2019. **34**(10): p. 2351-2359.
34. Linde, K.N., et al., *Component migration, bone mineral density changes, and bone turnover markers in cementless and cemented total knee arthroplasty: A prospective randomized RSA study in 53 patients with 2-year follow-up*. Knee Surgery, Sports Traumatology, Arthroscopy, 2022. **30**(9): p. 3100-3113.
35. Pijls, B.G., J.W. Plevier, and R.G. Nelissen, *RSA migration of total knee replacements: a systematic review and meta-analysis*. Acta orthopaedica, 2018. **89**(3): p. 320-328.





## General Discussion

---



This thesis delved into the intricate process of modeling the mechanical behavior of human bone using the ICF model. It was examined how the ICF model overcomes some of the limitations of traditional models and why it is beneficial for enhancing predictive accuracy in orthopedic applications. This discussion sets the stage for understanding the development, validation, and application of the ICF model, highlighting its strengths and limitations. Furthermore, BMD, as one of the key factors in predicting mechanical properties, is further discussed, ultimately emphasizing the potential of this modeling approach to improve personalized orthopedic care. Additionally, this chapter considers the broader implications of the model in clinical settings, particularly in reducing the risk of implant failures.

In this study, the ICF constitutive model based on common pressure-sensitive yield formulations, widely used in commercial FE packages, was specifically developed and characterized for bone mechanics. While the plastic behavior follows standard constitutive principles, the key advancements include the development of custom Fortran routines within the Marc–Mentat environment to define both the yield criterion and hardening behavior, and a novel methodology that directly links BMD to the hardening law and yield parameters, eliminating the need for extensive mechanical testing. By incorporating a density-dependent relationship, the model automatically updates critical material properties, such as the hardening slope, based on local BMD, enabling efficient, patient-specific simulations capturing both yield and post-yield responses.

## **Development and Validation of the ICF Model**

Chapter 2, with close links to Chapters 3 and 4, focused on the development and validation of the ICF model, addressed the limitations of earlier models such as the Drucker–Prager (DP) and softening Von Mises in simulating the post-yield behavior of human trabecular bone. The need for a more accurate predictive model arises from the critical role that biomechanical simulations play in orthopedic research, particularly in the context of implant fixation and risk assessments for bone fractures.

### **Development and advancements of ICF model in Bone-implant interactions**

The development of the Isotropic Crushable Foam (ICF) model marks a significant improvement over earlier models, such as the Drucker–Prager (DP) and softening Von Mises (sVM) models, which struggled to accurately simulate the post-yield behavior of human trabecular bone ([1-3] & Chapter 2). Both DP and sVM models

have inherent limitations in handling large volumetric compressions and cellular structure deformation, which are critical for predicting the realistic behavior of trabecular bone in orthopedic applications. Relative to DP and sVM, the ICF model offers a more realistic representation of trabecular bone mechanics, handling large volumetric compressions through its evolving elliptical yield surface.

The elliptical yield surface is defined by a shape factor "a" and a compression yield stress ratio "K", which can reflect state-dependent features of the bone density (Chapter 2 and 3). This feature is crucial in scenarios such as press-fit implant fixation, where bone density significantly affects implant outcomes and surgical success rates, as further explained below (4. Application of the ICF model). This dynamic approach sets it apart from DP and sVM models, providing a more accurate reflection of how trabecular bone behaves under stress. However, the extent to which this model resolves the limitations of its predecessors still warrants critical consideration.

A critical aspect of the development of the ICF model was deriving the mechanical properties of human bone, such as the Young's modulus, the yield stress in both uniaxial and confined situations, and the Poisson's ratio. These parameters were defined in this thesis based on BMD using power law relationships. The empirical equations for the ICF parameters were obtained from a limited set of bone samples—7 tibial and 8 femoral bones, totaling 100 cylindrical bone specimens. Although scientifically sufficient to determine mechanical properties, this sample set may not fully represent the variety of age-dependent bone qualities in different patients, suggesting that incorporating more cadaveric bone samples could enhance the model's robustness. Despite these limitations, the results of uniaxial simulations were promising, particularly in predicting yield, post-yield behavior, and quantifying plastic deformation (Chapters 2&3). However, the model still requires refinement in pure confinement scenarios, where it overestimated post-yield hardening behavior. Overall, the development of the ICF model represents a significant advancement in bone mechanics, particularly for simulating bone-implant interactions when bone is compressed beyond yield levels. This development may provide more reliable predictions in orthopedic research, although further work is needed to account for greater variability in bone properties across different populations.

## Validation of the ICF Model

The validation of the ICF model against experimental data showed promising results, particularly under compression loading. Simulations indicated 90% accuracy

in uniaxial conditions and 80% in confined compression scenarios. These figures highlight the model's strong predictive capability under compressive stress, especially up to 50% strain in uniaxial loading. However, an important consideration arose in confined compression simulations, where the model overestimated post-yield behavior beyond 15% strain, pointing to a potential flaw in the hardening-softening rule used for higher levels of confinement ([4], Chapter 2&3). This discrepancy suggests that while the ICF model excels in specific conditions, its application under large strain confined compression may require additional calibration.

Furthermore, comparisons with the SVM model underline the ICF model's improved accuracy in simulating hydrostatic stress. For instance, in confined compression tests, the ICF model predicted maximum stresses of 25 MPa compared to the SVM model's 280 MPa, with the ICF predictions closer to the experimental value of 14 MPa (Chapter 3). This demonstrates the ICF model's superior accuracy in scenarios involving high compressive forces, yet the overestimation in some cases indicates the need for refinement. Although the ICF model still operates under the limitation of pure confinement conditions (Chapters 2&3), this result demonstrates its ability to better capture hydrostatic stress effects, particularly in semi-confined compression scenarios, such as those encountered during procedures like press-fit implantation or tibial implant collapse in TKA. It should be noted that validation under other stress conditions, such as tensile strength (for example in bone bending scenario), remains less explored. Orthopedic applications may involve mixed loading conditions, suggesting the need for further model refinement and validation to extend its applicability.

### **Incorporation of Cortical Bone Parameters**

While the ICF model primarily targets trabecular bone behavior, it has also been extended to simulate cortical bone by integrating a constant strength ratio based on previous material studies (Chapter 3). The model's ability to simulate both trabecular and cortical bone presents a key advantage for orthopedic applications, as these two bone types exhibit significantly different mechanical properties. Trabecular bone, with its foam-like structure, absorbs stress and distributes forces, whereas cortical bone, which is more rigid, bears loads [5]. However, it is important to recognize that the ICF model's BMD-dependent parameter, "K", has a limited impact on cortical bone behavior, as cortical bone's response is less influenced by variations in BMD. Thus, while the model can simulate both bone types, its predictive power for cortical bone may not be as robust, warranting further investigation into how the model could better accommodate this bone's properties, particularly under mixed loading conditions.

## Performance Under Cyclic Loading and Fatigue

Another critical area where the ICF model demonstrates its utility is in simulating cyclic loading, which is essential for understanding long-term mechanical behavior of bone in various orthopedic applications. Cyclic loading simulations revealed that the ICF model could replicate the gradual energy dissipation and plastic deformation observed in experimental data, a feature that the sVM model failed to capture (Chapter 5). While the sVM model rapidly showed plastic deformation and failed to simulate further degradation beyond the initial cycles, the ICF model more accurately represented the gradual fatigue behavior typical of trabecular bone under repeated loads [6]. This finding is particularly important for predicting bone failure under fatigue conditions, which is a common concern in orthopedic procedures such as joint replacements. The model's ability to simulate progressive energy dissipation and plastic deformation over time makes it a valuable tool for long-term orthopedic planning. However, future work is needed to ensure that the ICF model can also accurately simulate other failure mechanisms, such as fracture under tensile or shear stresses, which remain less developed in the current framework. Obviously, it should be realized that the biological repair mechanism of bone under dynamic loading was not considered in the current thesis and is also an important topic to address when a realistic simulation of peri-prosthetic bone failure due to repetitive loading is analyzed.

## Application of the ICF model

In this thesis the ICF model was applied to various orthopaedic applications. Its accurate prediction of compressive stress and hydrostatic effects can ultimately lead to better implant designs and improved surgical outcomes, especially in procedures involving press-fit implantation where bone collapse is a realistic failure mechanism. By accounting for these effects, utilization of the ICF model has the potential to assist in developing implants with enhanced fixation stability and reduced likelihood of implant loosening or failure.

### Simulating Bone strength

The study in Chapter 3 demonstrates that the ICF model effectively simulates the nonlinear behavior of both trabecular and cortical bone, which is critical for predicting femoral fractures and validating results against experimental data and the sVM model. While the ICF model outperformed predicting bone strength with an accuracy of 90%, the sVM model also delivered competitive predictions, achieving 82% accuracy (Chapter 3). This suggests that in cases where cortical

bone plays a dominant role, the sVM model may still serve as a simpler and viable alternative due to its widespread use and computational efficiency.

In the simulation of femoral fractures, the ICF model's predictions for fracture locations closely matched experimental results, outperforming the sVM model, which predicted only sub-capital fractures. Nevertheless, and similarly to the sVM model, the ICF model still fell short in capturing the precise fracture pattern, which may be necessary for clinical applications. As mentioned in the development section, this may be due to the incompleteness of the ICF model under tensile loading conditions (apparent in some femoral fracture modes). Currently, it is assumed that the yield surface is asymmetric for compression and tension. By conducting tensile experiments, the tensile strength ratio can be determined, allowing for better calibration of the tensile behavior of the model leading to improved predictions under complex loading conditions. However, conducting tensile experiments on trabecular bone samples presents significant challenges. Additionally, besides from the tensile features, the anisotropy of bone structure, which is currently ignored in ICF model, may further contribute to the limitation for capturing the actual fracture pattern.

### **Simulating Initial Implant Stability**

In Chapter 4, both the ICF model and the sVM model were employed to simulate human femoral trabecular bone under cyclic loading conditions, with the simulation results compared to experimental data. Additionally, micromotion at the bone-implant interface was calculated to assess primary implant fixation, and the plastic deformation beneath the implant was evaluated for comparison.

The ability of the ICF model to more accurately capture the cyclic mechanical response compared to the sVM model (see Section 2.2 of this chapter) makes it particularly valuable for predicting long-term orthopedic outcomes, where evaluating bone failure under fatigue conditions is critical. Its effectiveness in reflecting micromotion patterns that closely align with experimental data highlights its potential in clinical applications, particularly in implant design, where minimizing cyclic motions at the bone-implant interface is crucial. Studies by Sanchez et al. and Berahmani et al. [7, 8] emphasize the importance of a detailed understanding of the implant-bone interface for optimizing the initial stability of cementless implants, a factor that can be better assessed using the ICF model.

While the ICF model results for micromotion have not been directly validated against experimental data to provide a conclusive justification, the average

micromotion predicted by the ICF model (27  $\mu\text{m}$ ) is comparable to values reported in previous studies, such as Berahmani's et al. and Sanchez et al., who noted 43  $\mu\text{m}$  and 25  $\mu\text{m}$  average, respectively. Although these comparisons do not constitute a point-to-point validation, they suggest a reasonable alignment. Furthermore, considering the ICF model's ability to replicate experimental observations, such as gradual energy dissipation and localized plastic deformation, its potential for providing an accurate response is supported. These factors collectively underscore the ICF model's theoretical validity in predicting micromotion at the implant-bone interface, despite the need for further experimental validation.

In the study presented in Chapter 5, a relatively simple frictional model and low interference fit were used in the simulations. However, if actual press-fit sizes were applied, the results for the sVM model could differ considerably. As discussed in Chapter 3, the sVM model—and more broadly, models commonly used for human bone simulation, such as the Drucker-Prager or Mohr-Coulomb models examined by Kelly et al. [2]—struggle to accurately capture large deformations in semi-confined simulations, potentially leading to invalid results. Therefore, in cases with high interference fit, where deformation around the implant (such as pegs) can be significant and resemble semi-confined conditions, the use of the ICF model may be more appropriate, though experimental validation is still needed.

### **Simulating Long-term TKA Failure**

In Chapter 5 we explored the critical issue of periprosthetic bone loss and its implications on the failure risk of tibial TKA components. The simulations using the ICF model demonstrated that poor initial bone quality, exacerbated by post-operative bone loss, significantly increased the risk of implant subsidence and failure, particularly in the medial tibial compartment. The ICF model was chosen over sVM model for predicting tibial implant failure due to its ability to simulate the complicated behavior of trabecular bone. As the mechanism of capturing localized deformation and energy dissipation was explained in chapter 3 and 4, ICF model demonstrates gradual deformation and pressure-dependent plasticity, aligning closely with experimental observations. Additionally, investigation in Chapter 3 revealed that the sVM model overestimated stiffness and strength in semi-confined situations. While in uniaxial loading (such as femoral fracture simulation) the overestimation may stem from the deviation in elastic regime, it shows the model has less capability capturing the correct stress states and plastic deformation patterns observed under high-pressure conditions. This limitation suggests that using sVM for simulations in such scenarios may offer limited added value, as it may not effectively identify implant subsidence.

The ICF model's findings align with clinical observations by Park et al. and Gundry et al. [9, 10], who reported higher failure rates in areas with significant bone loss, emphasizing the importance of managing bone quality to improve long-term TKA outcomes. However, studies by Ritter et al. [11] and Bergink et al. [12] noted an increase in BMD before TKA failure, challenging the conventional understanding of bone dynamics. This BMD increase can be explained biomechanically as a response to altered loading conditions, where bone initially becomes denser but more brittle, increasing the risk of implant failure under cyclic loads. These contrasting findings highlight the complexity of post-TKA bone remodeling and suggest that more sophisticated models, incorporating factors to account for brittleness, may be needed to better predict failure and understand long-term outcomes.

## Limitations

The research as described in this thesis faced several limitations across both the experimental and numerical phases, as well as in the practical challenges associated with clinical application. These limitations have important implications for the interpretation of our results and must be carefully considered when drawing conclusions from the various studies incorporated in this thesis.

First, the variability in cadaveric bone properties, influenced by factors such as age, sex, and overall bone health, presents a significant challenge to the reproducibility and generalizability of our findings. These inherent differences may lead to outcomes that do not fully capture the diversity of bone behavior across populations. Additionally, the use of dried bone samples may overlook critical visco-elastic-plastic properties important under real physiological conditions, potentially leading to an incomplete understanding of in vivo bone behavior. Furthermore, the accuracy of the experimental setup, including load cells, displacement sensors, and data acquisition systems, was constrained by their resolution and calibration, which may have led to measurement errors. Despite these experimental limitations, the errors in our results are consistent with acceptable ranges in the literature, and our findings align closely with other studies.

In the numerical phase, the main limitation is that isotropic material properties were assumed for bone, while bone typically displays an anisotropic response. This means the models may not accurately predict how bone behaves under different 3-dimensional stress states. Furthermore, the success of FEA depends heavily on accurate input data and realistic assumptions. However, the variability in BMD

measurements and the use of simplified loading conditions can lead to models that do not fully capture the complex interactions between bone and implants in real-life situations. For example, finite element models often assume idealized conditions, like perfect fixation of the implant, an exact fit, constant frictional conditions, or simplified (generalized) loading conditions without being able to adequately consider the variability for individual (patient) cases. To enhance knowledge about the effects of these variations, sensitivity studies might be helpful, thereby varying sequentially uncertain parameters within realistic ranges and assess how the outcome parameters (e.g. prosthetic failure) depend on these variations.

Another concern in the numerical sections is that the validation of FEA against experimental data often involves simplifications when transferring the experimental condition to the computer simulation. Also, our studies typically use scaled-down, simplified models that might not accurately represent real clinical conditions, especially when they overlook biological responses like healing and remodeling, which are vital for understanding interactions within a living system. Additionally, important long-term factors such as wear, fatigue, and actual bone remodeling after implantation are frequently not considered, even though they are crucial for evaluating the longevity and success of implants. To address these issues, it is essential to incorporate more realistic material properties, improve the accuracy of experimental setups and FEA, and expand model validation to include long-term and dynamic loading scenarios. Doing so would significantly enhance the predictive capacity and clinical relevance of these biomechanical models, which is crucial for optimizing implant designs, and ultimately improving patient outcomes in orthopedic treatments.

## Future Perspectives

Future research could focus on advancing computational bone models from isotropic to anisotropic to more accurately reflect the complex and varied nature of bone tissue. While current models like ICF, sVM, or DP are effective for certain applications, they often rely on assumptions of uniformity that may not fully represent the differential properties across individual bones and patients. Enhancing these models to capture the real-world complexity of bone properties can improve their accuracy and utility, particularly in clinical settings for investigating bone failure mechanisms and developing personalized treatment plans. Although these advancements are beneficial, simpler models in use today can still effectively support procedures like joint arthroplasty.



Additionally, integrating comprehensive patient-specific data, such as BMD mappings, could tailor local bone behavior. This can be achieved through a statistical BMD Model and deep learning-based image processing techniques, capturing bone anisotropy and assigning directional material properties. Future studies could also explore machine learning algorithms to predict outcomes from large datasets of patient scans and treatment results, refining bone preparation by the surgeons and post-operative care. By incorporating these databases into simulations and extending results from image processing, researchers can simultaneously predict failure and plan surgeries during radiological imaging, saving significant time.

Expanding the scope of FEA simulations to include broader and more variable conditions, such as different loading scenarios, patient anatomies, and pathological conditions is critical. These simulations should be validated against experimental data that more closely mimic the *in vivo* environment, considering factors like biological healing responses and long-term bone remodeling processes. This can be achieved by updating the BMD mapping used during simulation phases to reflect changes in material properties at different stages of healing. For example, bone material might initially be weaker and more compliant right after an injury, but gradually become stronger when local loading is relatively high. Also, implementing adaptive algorithms that modify the bone's material properties based on strain thresholds can enhance the simulations. This approach ensures that the ICF model is not only influenced by mechanical state but also by biological states.

Finally, to effectively create a detailed bone model that captures its complex characteristics and is simple enough for clinical use, we must integrate knowledge from biomechanics, materials science, and orthopedic surgery. Through such collaboration, we can enhance personalized orthopedic treatments, improving implant designs and surgical techniques specific to each patient's needs. This approach minimizes the risk of implant failures and the necessity for additional surgeries.

## Conclusion

In conclusion, this thesis developed a material model that enhances biomechanical bone modeling, particularly improving TKA simulations and investigating bone failure mechanisms in TKA. By calibrating the ICF model using bone-specific mechanical properties and failure data, the model accurately simulates bone behavior and improves predictions of bone failure in orthopedic applications (RQ1).

This enhanced simulation provides more precise assessments of bone strength and failure risk by modeling how bone tissue deforms and fails under stress (RQ2). The mechanical properties of bone significantly influence TKA implant stability by affecting the interface resistance between the bone and the implant. The ICF model impacts the prediction of this stability by providing accurate simulations of bone behavior, leading to a more realistic assessments of implant performance (RQ3). By simulating large deformations and progressive yielding, the ICF model can effectively assess how the mechanical properties of bone influence the long-term success of TKA, predicting how changes in bone density and strength under load may lead to implant loosening or failure (RQ4).

## References

1. Kelly, N., et al., *An experimental and computational investigation of the post-yield behaviour of trabecular bone during vertebral device subsidence*. Biomechanics and modeling in mechanobiology, 2013. **12**: p. 685-703.
2. Kelly, N. and J.P. McGarry, *Experimental and numerical characterisation of the elasto-plastic properties of bovine trabecular bone and a trabecular bone analogue*. Journal of the mechanical behavior of biomedical materials, 2012. **9**: p. 184-197.
3. Schulze, C., et al., *Calibration of crushable foam plasticity models for synthetic bone material for use in finite element analysis of acetabular cup deformation and primary stability*. Computer Methods in Biomechanics and Biomedical Engineering, 2019. **22**(1): p. 25-37.
4. Yu, T., et al., *Finite element modeling of confined concrete-I: Drucker–Prager type plasticity model*. Engineering structures, 2010. **32**(3): p. 665-679.
5. Safadi, F.F., et al., *Bone structure, development and bone biology*. Bone pathology, 2009: p. 1-50.
6. Topoliński, T., et al., *Fatigue energy dissipation in trabecular bone samples with stepwise-increasing amplitude loading*. Materials Testing, 2011. **53**(6): p. 344-350.
7. Berahmani, S., D. Janssen, and N. Verdonchot, *Experimental and computational analysis of micromotions of an uncemented femoral knee implant using elastic and plastic bone material models*. Journal of biomechanics, 2017. **61**: p. 137-143.
8. Sánchez, E., et al., *The effect of different interference fits on the primary fixation of a cementless femoral component during experimental testing*. Journal of the mechanical behavior of biomedical materials, 2021. **113**: p. 104189.
9. Gundry, M., S. Hopkins, and K. Knapp, *A review on bone mineral density loss in total knee replacements leading to increased fracture risk*. Clinical Reviews in Bone and Mineral Metabolism, 2017. **15**: p. 162-174.
10. Park, H.J., et al., *A three-dimensional finite element analysis on the effects of implant materials and designs on periprosthetic tibial bone resorption*. PLoS One, 2021. **16**(2): p. e0246866.
11. Ritter, M., et al., *Trabecular bone density of the proximal tibia as it relates to failure of a total knee replacement*. The bone & joint journal, 2014. **96**(11): p. 1503-1509.
12. Bergink, A.P., et al., *Osteoarthritis of the knee is associated with vertebral and nonvertebral fractures in the elderly: the Rotterdam Study*. Arthritis Care & Research: Official Journal of the American College of Rheumatology, 2003. **49**(5): p. 648-657.





## Chapter 7

### Summary

---

This dissertation applies the isotropic crushable foam (ICF) model to enhance understanding and predictability of the biomechanical behavior of bone around a TKA. In this chapter an integrated overview is provided of how chapters 2 through 5 of the thesis directly address each of the four research questions as posed in the Introduction, demonstrating the methodological approaches and findings that contribute to the field of orthopedic biomechanics.

## **Characterizing ICF model with Trabecular Bone Properties: Chapter 2**

*Research Question 1: How can the isotropic crushable foam model be characterized to improve the prediction of bone failure in orthopedic applications?*

The chapter presents the development and validation of an ICF model to characterize the mechanical behavior of human trabecular bone, aiming to improve the prediction of bone failure in orthopedic applications. FE simulations were conducted to evaluate the mechanical response of trabecular bone, with a special focus on post-yield behavior. Sixty-two cylindrical bone samples from human cadaveric tibias, ranging in BMD from 26 mg/cc to 207 mg/cc, were subjected to uniaxial and confined compression tests. Key material parameters, including Young's modulus, yield stress, and Poisson's ratio, were determined experimentally and used to develop the CF model.

Experimental data identified key material parameters correlated with BMD via power-law distributions, showing strong correlations:  $r = 0.748$  ( $p < 0.001$  and  $SEE = 72.17$ ) for Young's modulus,  $r = 0.883$  ( $p < 0.001$  and  $SEE = 0.951$ ) for uniaxial yield stress, and  $r = 0.921$  ( $p < 0.001$  and  $SEE = 0.872$ ) for confined yield stress. Experimentally derived parameters were implemented in FE simulations using the CF model with isotropic hardening. The FE model was validated against experimental stress-strain data for five specimens from each configuration, accurately replicating critical features like Young's modulus, yield stress, and ultimate yield stress, especially post-yield behavior under uniaxial compression. Simulated ultimate compressive stress values (0.53–7.59 MPa) closely matched experimental data with an error margin of less than 5%. For confined compression, the model predicted stress-strain behavior up to 15% strain accurately but overestimated hardening beyond this point. Experimental confined yield stress ranged from 0.16 to 9.02 MPa, with simulated results within this range but showing discrepancies at higher strains. Additionally, describing the differential changes in plastic strain based on the flow potential rule in ICF enabled realistic deformations of trabecular bone. Identifying plastic zones with maximum equivalent plastic

strain in simulations indicated the failure pattern of experimental specimens and served as a good predictor of bone damage.

The ICF model demonstrated potential for simulating bone collapse around orthopedic implants, although further refinement is needed to improve its accuracy in confined compression scenarios.

### **Extension of the ICF Model for the whole bone: Chapter 3**

*Research Question 2: Does the isotropic crushable foam model improve the prediction of human bone mechanical failure?*

This study investigates whether the ICF model improves the prediction of human bone mechanical failure, specifically for femoral fractures. Sixty-four human femoral trabecular cadaveric bone samples underwent mechanical testing to determine elastoplastic properties, which were combined with existing cortical bone data to develop continuous and discontinuous forms of the ICF model.

Continuous forms integrate bone properties in a smooth, uninterrupted manner, allowing for consistent material behavior across the bone structure, while discontinuous forms apply distinct transitions between trabecular and cortical bone types. These models were evaluated by simulating experimental femoral fractures and compared with the softening Von-Mises (sVM) material model.

Experimental data showed significant correlations between BMD and mechanical properties: Young's modulus ( $r = 0.768$ ,  $p < 0.001$ ,  $SEE = 46.76$ ), uniaxial yield stress ( $r = 0.836$ ,  $p < 0.001$ ,  $SEE = 0.742$ ), and confined yield stress ( $r = 0.894$ ,  $p < 0.001$ ,  $SEE = 0.873$ ). When applied to uniaxial compression of bone samples, the ICF model accurately replicated stress-strain curves seen in tibial bones (87% accuracy for ultimate stress, 95% for stiffness). However, the sVM model overestimated stiffness by 350% but achieved 92% accuracy for ultimate stress. In confined simulations, the ICF model's predictions were comparable to experimental values up to 10% strain, while the sVM model failed, showing a maximum stress of 280 MPa at 50% strain compared to 25 MPa for ICF and 14 MPa experimentally.

For femoral fractures, the ICF model predicted failure loads with 79% (continuous) and 90% (discontinuous) accuracy compared to experimental values, while the sVM model achieved 82%. The ICF model's predicted fracture locations matched experimental observations, whereas the sVM model consistently predicted sub-capital fractures.



The ICF model improves the prediction of human bone mechanical failure by accurately capturing the nonlinear mechanical response. The BMD-dependent ICF model showed enhanced accuracy in predicting failure loads and fracture locations, with up to 90% accuracy compared to experimental values. These findings indicate that the ICF model could be a promising tool for orthopedic applications, such as press-fit implant fixation, by providing a more reliable prediction of bone strength and fracture risk.

### **Analysis of Initial Stability in TKA: Chapter 4**

*Research Question 3: How do the mechanical properties of bone influence the initial stability of TKA implants, and how do different constitutive models impact the prediction of this stability?*

This study investigates the influence of human bone mechanical properties on the initial stability of TKA implants, focusing on the impact of two different constitutive models on predicting this stability. The study included experimental tests on human femoral trabecular bone under cyclic loading and FE simulations incorporating ICF and sVM models both to replicate the cyclic response of the bone and then quantify micromotions at the bone-implant interface during a daily activity and assess the efficacy of these bone material models in predicting these micromotions.

Human trabecular bone samples were cyclically loaded for 100 cycles with an axial displacement of 0.5 mm, measuring reaction force and permanent deformation. BMD values from scanned samples were used in specimen-specific FE models. The FE models, based on QCT scans of trabecular bone samples and femurs from cadaveric specimens aged 57, 73, and 90 were generated. The bone samples simulated cyclic uniaxial loading and femoral models simulated micromotions at the bone-implant interface under gait loads.

Experimental results showed gradual energy dissipation with the reaction force stabilizing at 700-800 N after initial cycles. The ICF model replicated this pattern closely, matching the maximum reaction force (experiment: 1580 N, ICF: 1630 N) and plastic deformation (experiment: 0.3 mm, ICF: 0.36 mm). In contrast, the sVM model showed significant initial plastic deformation, with the reaction force dropping to 650 N after the first cycle, while displacement was much lower in sVM (0.11 mm), indicating an overestimation of stiffness.

In FE simulations, the ICF model predicted average micromotions of 27  $\mu\text{m}$ , ranging from 6 to 127  $\mu\text{m}$  in different implant regions. The sVM model predicted lower

average micromotions of 17  $\mu\text{m}$ , ranging from 4 to 67  $\mu\text{m}$ . Both models identified the highest micromotions at the anterior flange, indicating a potential critical region for implant stability. The ICF model also showed plastic strains around pegs and at the anterior and posterior condyles, aligning with previous experimental findings. The sVM model had a similar distribution but with deeper and wider plastic deformations.

**Comparison of Models:** The ICF model better matched experimental data, especially in replicating the gradual increase and capturing localized plastic deformation. While previous studies showed sVM had lower micromotion compared to experiments, the ICF currently shows higher micromotion values. Further validation of the ICF against experimental findings is still required.

The mechanical properties of bone, represented differently by the ICF and sVM material models, can greatly impact the prediction of TKA implant stability. The pressure-dependent ICF model offered a more realistic simulation of bone plasticity, indicating its potential superiority in predicting micromotions at the bone-implant interface. This study highlighted the importance of selecting appropriate material models for accurate predictions in biomechanical simulations of TKA.

## Long-Term Predictions Using the ICF Model: Chapter 5

*Research Question 4: How can the isotropic crushable foam model assess the impact of bone mechanical properties on the long-term failure of TKA?*

In the last chapter, a study is described investigating the effect of long-term periprosthetic bone loss on the failure risk of tibial TKA, focusing on how bone mechanical properties influence long-term implant stability. Using an ICF model in FEA, the research simulated postoperative changes in BMD to assess the impact of bone resorption on tibial TKA failure.

FEA models were created from the scanned tibiae of a 65-year-old male (good bone quality) and a 90-year-old female (poor bone quality). The models included the Triathlon tibial component and a 2 mm cement layer. Loading conditions simulated standard walking and traumatic stumble events, with the latter to mimic a trauma. Bone material properties were derived from clinical BMD data over a seven-year postoperative period.

Under repeated walking loads, neither tibia model exhibited failure. The good quality bone model reached a steady state of plastic deformation after 60 cycles,

while the poor-quality bone model required 190 cycles. Application of the stumble load resulted in significant rotational migration in the poor-quality bone model, increasing from 3.7° immediately postoperative to 15.2° at seven years, indicating high failure risk. The good quality bone model showed minimal migration (<1°) under the same conditions.

Peak plastic strains were observed mainly in the medial compartment. For the good quality bone, strains were minimal immediately postoperative but increased slightly over time. In contrast, the poor-quality bone exhibited substantial plastic deformation from the outset, worsening with ongoing bone loss.

Quantitative analysis underscored that postoperative bone loss substantially elevates the risk of TKA failure in poor quality bone, evidenced by significant tibial component subsidence. These findings emphasize the critical role of bone quality in TKA longevity. The ICF model effectively predicts the impact of bone mechanical properties on implant stability, offering valuable insights for preoperative planning and postoperative management to enhance clinical outcomes in TKA patient.

# Research Data Management

## 1. Ethics and Privacy

For this thesis, no human subject data were used. The research primarily involved cadaveric bone samples to assess mechanical properties. The data obtained from these samples are fully anonymized, as the cadavers used in the research were handled without any identifying information. The research also utilized Finite Element Analysis (FEA) and computer simulations.

## 2. Data Collection and Storage

The data related to this thesis were stored and analyzed on a secure network drive dedicated to the Orthopedic Research Lab under data protection policy of Radboudumc, that was accessible only to PhD candidate and the direct supervisors. This secure storage solution ensures the availability, integrity, and confidentiality of the data throughout the research process.

## 3. Data Sharing According to FAIR Principles

All research findings associated with this thesis have been published in open access journals, promoting transparency and widespread dissemination. The datasets used in this thesis are openly accessible without restrictions, and they have been published in a Data Sharing Collection (DSC) in the Radboud Data Repository (<https://data.ru.nl>). The Co-promotor of this dissertation, Dennis Janssen (Dennis.janssen@radboudumc.nl), as the Principal Investigator (PI) is the owner of the DSC, ensuring compliance with Radboudumc's Research Data Management policies.



## Samenvatting

---

In dit proefschrift is een isotropic crushable foam (ICF) model ontwikkeld om biomechanische modellen van bot en orthopedische reconstructies te verbeteren. In dit hoofdstuk wordt een samenvatting gegeven van hoe hoofdstukken 2 tot en met 5 de vier onderzoeksvragen uit de Inleiding behandelen, waarbij de methodologische benaderingen en bevindingen uiteen worden gezet.

## **Kenmerken van het ICF-model met eigenschappen van trabeculair bot: Hoofdstuk 2**

*Onderzoeksvraag 1: Hoe kan het isotropic crushable foam model worden gekarakteriseerd om de voorspelling van botfalen in orthopedische toepassingen te verbeteren?*

Dit hoofdstuk presenteert de ontwikkeling en validatie van een ICF-model om het mechanische gedrag van menselijk trabeculair bot te karakteriseren, met als doel de voorspelling van botfalen in orthopedische toepassingen te verbeteren. FE-simulaties werden uitgevoerd om de mechanische respons van trabeculair bot te evalueren, met speciale aandacht voor het post-falen gedrag. Tweeënzestig cilindrische botsamples van menselijke kadavertibia's, met een BMD variërend van 26 mg/cc tot 207 mg/cc, werden belast in uniaxiale en alzijdige compressietesten. Belangrijke materiaaleigenschappen, waaronder de elasticiteitsmodulus (Young's modulus), vloeigrens en Poisson's ratio, werden experimenteel bepaald en gebruikt om het ICF-model te ontwikkelen.

Uit experimentele gegevens werden belangrijke parameters geïdentificeerd die gecorreleerd waren met BMD. Sterke correlaties werden aangetoond:  $r = 0,748$  ( $p < 0,001$  en  $SEE = 72,17$ ) voor de elasticiteitsmodulus,  $r = 0,883$  ( $p < 0,001$  en  $SEE = 0,951$ ) voor uniaxiale vloeigrens, en  $r = 0,921$  ( $p < 0,001$  en  $SEE = 0,872$ ) voor alzijdige compressie vloeigrens. Experimenteel afgeleide parameters werden geïmplementeerd in FE-simulaties met het CF-model met isotrope versteviging. Het FE-model werd gevalideerd aan de hand van experimentele spanning-rek gegevens voor vijf samples van elke configuratie, waarbij kritieke kenmerken zoals Young's modulus, vloeigrens en het post-falen gedrag nauwkeurig werden gesimuleerd. Modelwaarden voor de uiteindelijke druksterkte (0,53–7,59 MPa) kwamen nauw overeen met experimentele gegevens met een foutmarge van minder dan 5%. Voor alzijdige compressie voorspelde het model de spanning-rek respons tot 15% rek nauwkeurig, maar overschatte de versteviging na dit punt. De experimentele alzijdige compressie vloeigrens varieerde van 0,16 tot 9,02 MPa, waarbij de gesimuleerde resultaten binnen dit bereik lagen, maar afwijkingen vertoonden bij hogere rekwaarden. Bovendien maakte het beschrijven van de differentiële veranderingen in plastische rek op basis van de stroompotentiaalregel

in ICF realistische vervormingen van trabeculair bot mogelijk. Het identificeren van plastische zones met maximale equivalente plastische rek in simulaties gaf het faalpatroon van experimentele monsters aan en fungeerde als een goede voorspeller van botschade.

Het ICF-model toonde potentieel voor het simuleren van botfalen rond orthopedische implantaten, hoewel verdere ontwikkeling nodig is om de nauwkeurigheid bij alzijdige compressie te verbeteren. Deze bevindingen wijzen erop dat het model de voorspelling van botfalen in orthopedische toepassingen kan verbeteren door de niet-lineaire mechanische respons van trabeculair bot te kunnen simuleren.

### **Uitbreiding van het ICF-model voor het gehele bot: Hoofdstuk 3**

*Onderzoeksvraag 2: Verbetert het isotrope samendrukbare schuim model de voorspelling van mechanisch botfalen bij mensen?*

Deze studie onderzoekt of het ICF-model de voorspelling van mechanisch botfalen bij mensen verbetert, met name voor femorale fracturen. Vierenzestig trabeculaire botsamples van menselijke femora ondergingen mechanische tests om elastoplastische eigenschappen te bepalen, die werden gecombineerd met bestaande gegevens over corticaal bot om continue en discontinue vormen van het ICF-model te ontwikkelen. Experimentele gegevens toonden significante correlaties tussen BMD en mechanische eigenschappen: elasticiteitsmodulus ( $r = 0,768$ ,  $p < 0,001$ ,  $SEE = 46,76$ ), uniaxiale vloeigrens ( $r = 0,836$ ,  $p < 0,001$ ,  $SEE = 0,742$ ), en alzijdige compressie vloeigrens ( $r = 0,894$ ,  $p < 0,001$ ,  $SEE = 0,873$ ). Bij toepassing op uniaxiale compressie van botsamples simuleerde het ICF-model nauwkeurig spanning-rek curven zoals gemeten in tibiale botten (87% nauwkeurigheid voor uiteindelijke spanning, 95% voor stijfheid). Het sVM-model overschatte echter de stijfheid met 350%, maar behaalde een nauwkeurigheid van 92% voor de uiteindelijke spanning. In simulaties van alzijdige compressie waren de voorspellingen van het ICF-model vergelijkbaar met experimentele waarden tot 10% rek, terwijl het sVM-model faalde, met een maximale spanning van 280 MPa bij 50% rek vergeleken met 25 MPa voor ICF en 14 MPa experimenteel.

Voor femorale botfracturen voorspelde het ICF-model faalbelastingen met 79% (continu) en 90% (discontinu) nauwkeurigheid vergeleken met experimentele waarden, terwijl het sVM-model 82% behaalde. De door het ICF-model voorspelde fractuurlocaties kwamen overeen met experimentele observaties, terwijl het sVM-model consequent sub-capitale fracturen voorspelde.



Het ICF-model verbetert de voorspelling van mechanisch botfalen bij mensen door de niet-lineaire mechanische respons nauwkeurig te simuleren. Het BMD-afhankelijke ICF-model toonde een verbeterde nauwkeurigheid bij het voorspellen van faallasten en fractuurlocaties, met een nauwkeurigheid tot 90% vergeleken met experimentele waarden.

### **Analyse van Initiële Stabiliteit bij TKA: Hoofdstuk 4**

*Onderzoeksvraag 3: Hoe beïnvloeden de mechanische eigenschappen van bot de initiële stabiliteit van TKA-implantaten, en hoe beïnvloeden verschillende constitutieve modellen de voorspelling van deze stabiliteit?*

Deze studie onderzoekt de invloed van de mechanische eigenschappen van menselijk bot op de initiële stabiliteit van TKA-implantaten, waarbij de impact van twee verschillende constitutieve modellen op de voorspelling van deze stabiliteit centraal staat. Het onderzoek omvatte experimentele tests op trabeculair bot van de menselijke femur onder cyclische belasting en FE-simulaties met zowel ICF- als SVM-modellen. Het doel was om de cyclische respons van het bot na te bootsen en om vervolgens de microbewegingen op het de interface tussen bot en implantaat te kwantificeren. Hiermee werd de effectiviteit van deze botmateriaalmodellen geëvalueerd in het voorspellen van deze microbewegingen. Humane trabeculaire botsamples werden cyclisch belast voor 100 cycli met een axiale verplaatsing van 0,5 mm, waarbij reactiekracht en permanente vervorming werden gemeten. BMD-waarden van gescande monsters werden gebruikt in specimen-specifieke FE-modellen. De FE-modellen, gebaseerd op QCT-scans van trabeculair bot van donoren van 57, 73 en 90 jaar oud, werden gegenereerd. De botsamples simuleerden cyclische uniaxiale belasting, en femorale modellen simuleerden microbewegingen op het bot-implantaatoppervlak onder loopbelasting.

De experimentele resultaten toonden aan dat er geleidelijk energie gedissipeerd werd, waarbij de reactiekracht stabiliseerde op 700-800 N na de eerste cycli. Het ICF-model simuleerde dit patroon nauwkeurig, met een overeenkomstige maximale reactiekracht (experiment: 1580 N, ICF: 1630 N) en plastische vervorming (experiment: 0,3 mm, ICF: 0,36 mm). Daarentegen vertoonde het SVM-model aanzienlijke initiële plastische vervorming, waarbij de reactiekracht daalde tot 650 N na de eerste cyclus, terwijl de verplaatsing veel lager was bij SVM (0,11 mm), wat wijst op een overschatting van de stijfheid.

In FE-simulaties voorspelde het ICF-model gemiddelde microbewegingen van 27  $\mu\text{m}$ , variërend van 6 tot 127  $\mu\text{m}$  in verschillende implantaatregio's. Het SVM-

model voorspelde lagere gemiddelde micromoties van 17  $\mu\text{m}$ , variërend van 4 tot 67  $\mu\text{m}$ . Beide modellen identificeerden de hoogste micromoties in de anterieure regio, wat een mogelijke kritieke regio voor implantaatstabiliteit kan zijn. Het ICF-model toonde ook plastische vervormingen rond de pegs en bij de anterieure en posterieure condylen, wat overeenkomt met eerdere experimentele bevindingen. Het sVM-model had een vergelijkbare verdeling, maar met diepere en bredere plastische vervormingen.

Vergelijking van Modellen: Het ICF-model kwam beter overeen met experimentele gegevens, met name in het repliceren van de geleidelijke toename en het vastleggen van gelokaliseerde plastische vervorming. Terwijl eerdere studies aantoonde dat het sVM-model lagere microbewegingen vertoonde in vergelijking met experimenten, laat het ICF-model hogere waarden zien. Verdere validatie van het ICF-model aan de hand van experimentele bevindingen is nog steeds vereist.

De mechanische eigenschappen van bot, verschillend weergegeven door de ICF- en sVM-materiaalmodellen, kunnen een grote invloed hebben op de voorspelling van TKA-implantaatstabiliteit. Het drukafhankelijke ICF-model bood een realistischer simulatie van botplasticiteit, wat erop wijst dat het model beter geschikt kan zijn voor het voorspellen van microbewegingen op het bot-implantaatoppervlak. Deze studie benadrukte het belang van geschikte materiaalmodellen voor nauwkeurige voorspellingen in biomechanische simulaties van TKA.

## Langetermijnvoorspellingen met het ICF-model: Hoofdstuk 5

*Onderzoeksvraag 4: Hoe kan het isotrope samendrukbare schuimmodel de impact van mechanische bot eigenschappen op het langetermijnfalen van TKA beoordelen?*

In het laatste hoofdstuk wordt een studie beschreven die het effect van botverlies rondom de prothese op het faalisico van tibiale TKA onderzoekt, met een focus op hoe de mechanische eigenschappen van bot de langetermijnstabiliteit van implantaten beïnvloeden. Door gebruik te maken van een ICF-model in FEA, simuleerde het onderzoek postoperatieve veranderingen in BMD om de impact van botresorptie op tibiaal TKA-falen te beoordelen.

FEA-modellen werden gemaakt van tibiae van een 65-jarige man (goede bot kwaliteit) en een 90-jarige vrouw (slechte botkwaliteit), met een Triathlon tibiaal implantaat. Als belasting zijn normaal lopen en een struikelincident gesimuleerd. Botmateriaal eigenschappen werden afgeleid van klinische BMD-gegevens over een periode van zeven jaar na de operatie.

Onder de loopbelasting vertoonde geen van beide tibiamodellen tekenen van falen. Het model met goede botkwaliteit bereikte een stabiele staat van plastische vervorming na 60 cycli, terwijl het model met slechte botkwaliteit 190 cycli nodig had. Het simuleren van struikelen resulteerde in aanzienlijke rotatie-migratie in het model met slechte botkwaliteit, van  $3,7^\circ$  direct na de operatie tot  $15,2^\circ$  na zeven jaar, wat wijst op een hoog faalrisico. Het model met goede botkwaliteit vertoonde minimale migratie ( $<1^\circ$ ) onder dezelfde omstandigheden.

Plastische vervormingen werden voornamelijk waargenomen in het mediale compartiment. Voor het botmodel met een goede botkwaliteit waren de vervormingen minimaal direct na de operatie, maar namen ze licht toe in de loop van de tijd. Daarentegen vertoonde het model met slechte botkwaliteit aanzienlijke plastische vervorming vanaf het begin, wat verergerde met voortgaand botverlies.

Kwantitatieve analyse benadrukte dat postoperatief botverlies het risico op TKA-falen aanzienlijk groter was bij slechte botkwaliteit, zoals blijkt uit aanzienlijke verzakking van het tibiale component. Deze bevindingen ondersteunen de cruciale rol van botkwaliteit in de levensduur van TKA. Het ICF-model voorspelde effectief de impact van mechanische bot eigenschappen op implantaatstabiliteit en biedt waardevolle inzichten voor preoperatieve planning en postoperatief management om de klinische resultaten bij TKA-patiënten te verbeteren.





## Chapter 9

خلاصه  
فارسی

---

## چکیده

این رساله با استفاده از مدل «فوم فشردنی همسانگرد (ICF)»، درک و قابلیت پیش‌بینی رفتار بیومکانیکی استخوان در اطراف ایمپلنت کامل زانو (TKA) را بهبود می‌دهد. در این فصل، یک مرور جامع ارائه می‌شود که نشان می‌دهد چگونه فصول دوم تا پنجم پایان‌نامه به‌طور مستقیم به چهار پرسش تحقیقاتی مطرح‌شده در مقدمه پاسخ می‌دهند و روش‌شناسی و یافته‌هایی را شرح می‌دهد که به پیشرفت حوزه بیومکانیک ارتوپدی کمک می‌کنند.

## توصیف مدل ICF بر اساس خواص استخوان اسفنجی؛ فصل دوم

### پرسش تحقیقاتی ۱: چگونه می‌توان مدل فوم فشردنی همسانگرد را برای پیش‌بینی بهتر شکست استخوان در کاربردهای

#### ارتوپدی مشخصه‌یابی کرد؟

این فصل توسعه و اعتبارسنجی مدل ICF برای توصیف رفتار مکانیکی استخوان اسفنجی انسانی را ارائه می‌دهد تا دقت پیش‌بینی شکست استخوان در کاربردهای ارتوپدی را بهبود بخشد. برای این هدف، شبیه‌سازی‌های المان محدود (FE) به منظور بررسی پاسخ مکانیکی استخوان اسفنجی، به‌ویژه رفتار پس از نقطه‌ی تسلیم، انجام گرفت. ۶۲ نمونه‌ی استخوانی استوانه‌ای شکل از تیبیاهای انسانی با تراکم معدنی استخوان (BMD) در محدوده‌ی ۲۶ تا ۲۰۷ میلی‌گرم بر سانتی‌متر مکعب تحت آزمایش‌های فشار تک‌محوره و محصورشده قرار گرفتند. پارامترهای کلیدی ماده، شامل مدول یانگ، تنش تسلیم و نسبت پواسون، به‌صورت تجربی اندازه‌گیری و در توسعه‌ی مدل فوم فشردنی (CF) استفاده شدند.

داده‌های آزمایشگاهی نشان دادند که پارامترهای ماده از طریق توابع توانی با BMD همبستگی قوی دارند: برای مدول یانگ ( $r = 0.748, p < 0.001$ ) و  $SEE = 72.17$ ، برای تنش تسلیم تک‌محوره ( $r = 0.883, p < 0.001$  و  $SEE = 0.951$ ) و برای تنش تسلیم محصورشده ( $r = 0.921, p < 0.001$  و  $SEE = 0.872$ ). سپس این پارامترهای تجربی در شبیه‌سازی‌های FE با مدل CF و سخت‌شوندگی همسانگرد به‌کار رفتند. اعتبارسنجی مدل FE با داده‌های آزمایشگاهی تنش-کرنش برای پنج نمونه از هر حالت بارگذاری انجام شد. این مدل توانست ویژگی‌های اصلی نظیر مدول یانگ، تنش تسلیم و تنش نهایی، به‌ویژه رفتار بعد از تسلیم در حالت فشار تک‌محوره را با دقت خوبی بازتولید کند. مقادیر شبیه‌سازی‌شده برای تنش فشاری نهایی (در بازه‌ی ۰.۵۳ تا ۷.۵۹ مگاپاسکال) با خطایی کمتر از ۵ درصد، با داده‌های تجربی تطابق بالایی داشتند.

در بارگذاری محصورشده، مدل تا کرنش ۱۵ درصد رفتار تنش-کرنش را دقیق پیش‌بینی کرد، اما در کرنش‌های بالاتر سخت‌شوندگی را بیش از حد واقعی برآورد نمود. مقادیر تجربی تنش تسلیم محصور در بازه‌ی ۰.۱۶ تا ۹.۰۲ مگاپاسکال بود و نتایج

شبیه‌سازی در همین محدوده قرار داشت؛ هرچند در کرنش‌های بالا تفاوت‌هایی مشاهده شد. همچنین با توصیف تغییرات کرنش پلاستیک بر اساس قانون پتانسیل جریان در مدل ICF، تغییر شکل‌های واقعی‌تری در استخوان اسفنجی بازتولید شد. تعیین مناطق پلاستیکی دارای حداکثر کرنش پلاستیک معادل در شبیه‌سازی‌ها، الگوی شکست نمونه‌های آزمایشگاهی را به خوبی منعکس کرد و شاخص مناسبی برای پیش‌بینی آسیب استخوانی بود.

در مجموع، مدل ICF قابلیت بالایی در شبیه‌سازی فروپاشی استخوان در اطراف ایمپلنت‌های ارتوپدی از خود نشان داد؛ با این حال، برای افزایش دقت پیش‌بینی در حالت فشار محصورشده، اصلاحات بیشتری نیاز است.

### توسعه مدل ICF برای استخوان کامل: فصل سوم

#### پرسش تحقیقاتی ۲: آیا مدل فوم فشردنی همسانگرد (ICF) می‌تواند پیش‌بینی فروپاشی استخوان انسان را بهبود دهد؟

این مطالعه بررسی می‌کند که آیا مدل ICF پیش‌بینی فروپاشی استخوان انسان را، به‌ویژه در نارسایی‌های استخوان ران، بهبود می‌دهد یا خیر. برای این هدف، ۶۴ نمونه استخوان اسفنجی ران انسانی از اجساد تحت آزمایش‌های مکانیکی قرار گرفتند تا خواص الاستوپلاستیک آن‌ها مشخص شود. این داده‌ها به همراه داده‌های موجود از استخوان فشرده، برای توسعه دو شکل پیوسته و ناپیوسته از مدل ICF استفاده شدند.

شکل پیوسته‌ی مدل، خواص استخوان را به‌صورت یکپارچه و بدون انقطاع توصیف می‌کند و رفتار ماده را در کل ساختار استخوان بصورت توانی یکنواخت در نظر می‌گیرد. در مقابل، شکل ناپیوسته، گذار مشخصی بین خواص استخوان اسفنجی و فشرده ایجاد می‌کند. این مدل‌ها با شبیه‌سازی شکستگی‌های آزمایشگاهی استخوان ران ارزیابی شده و نتایج آن‌ها با مدل ماده «فون میزس با نرم‌شوندگی (sVM)» مقایسه گردید.

داده‌های آزمایشگاهی نشان دادند که بین تراکم معدنی استخوان (BMD) و خواص مکانیکی استخوان همبستگی قوی وجود دارد: برای مدول یانگ ( $r = 0.768$ ,  $p < 0.001$ )،  $SEE = 46.76$ ، برای تنش تسلیم تک‌محوره ( $r = 0.836$ ,  $p < 0.001$ ) و  $SEE = 0.742$  و برای تنش تسلیم محصورشده ( $r = 0.894$ ,  $p < 0.001$ )،  $SEE = 0.873$ .

در شبیه‌سازی‌های فشاری تک‌محوره روی نمونه‌های استخوانی، مدل ICF توانست به‌طور دقیقی منحنی‌های تنش-کرنش نمونه‌های استخوان تبیین را بازتولید کند (دقت ۸۷ درصد برای تنش نهایی و ۹۵ درصد برای سختی). در حالی که مدل sVM سختی را تا ۳۵۰ درصد بیش از حد واقعی برآورد نمود ولی برای تنش نهایی به دقت ۹۲ درصد دست یافت. در شبیه‌سازی فشاری محصور، پیش‌بینی‌های مدل ICF تا کرنش ۱۰ درصد کاملاً مطابق با نتایج تجربی بود، اما مدل sVM ناموفق بود و در کرنش ۵۰



درصد، تنش حداکثری ۲۸۰ مگاپاسکال را پیش‌بینی کرد؛ این در حالی بود که تنش پیش‌بینی‌شده توسط ICF معادل ۲۵ مگاپاسکال و داده تجربی ۱۴ مگاپاسکال بود.

در پیش‌بینی شکستگی استخوان ران، مدل ICF با فرم پیوسته و ناپیوسته به ترتیب با دقت ۷۹٪ و ۹۰٪ توانستند بار شکستگی را نسبت به مقادیر آزمایشگاهی پیش‌بینی کنند، درحالی‌که مدل SVM به دقت ۸۲٪ رسید. همچنین موقعیت شکست پیش‌بینی‌شده توسط مدل ICF با محل شکست تجربی مطابقت خوبی داشت؛ اما مدل SVM به‌طور پیوسته شکستگی‌هایی در زیر سر استخوان ران (ساب‌کاپیتال) را پیش‌بینی نمود.

مدل ICF با در نظر گرفتن دقیق پاسخ مکانیکی غیرخطی استخوان، پیش‌بینی شکست مکانیکی استخوان انسان را بهبود می‌دهد. مدل ICF وابسته به BMD توانست بار شکست و محل دقیق شکستگی را تا ۹۰٪ با دقت بیشتری نسبت به داده‌های آزمایشگاهی پیش‌بینی کند. نتایج این مطالعه نشان می‌دهد مدل ICF می‌تواند ابزاری مؤثر در کاربردهای ارتوپدی، از جمله تثبیت ایمپلنت‌های پرس‌فیت باشد و پیش‌بینی قابل اعتمادتری از استحکام استخوان و خطر شکستگی ارائه دهد.

### تحلیل پایداری اولیه در ایمپلنت زانو: (TKA) فصل چهارم

**پرسش تحقیقاتی ۳: خواص مکانیکی استخوان چگونه بر پایداری اولیه ایمپلنت‌های TKA تأثیر می‌گذارند و مدل‌های رفتاری**

**مختلف ماده چه تأثیری در پیش‌بینی این پایداری دارند؟**

این مطالعه تأثیر خواص مکانیکی استخوان انسان را بر پایداری اولیه ایمپلنت‌های TKA بررسی می‌کند و تمرکز ویژه‌ای دارد بر اینکه دو مدل رفتاری مختلف (ICF) و (SVM) چگونه بر پیش‌بینی این پایداری اثر می‌گذارند. در این تحقیق آزمایش‌هایی بر روی استخوان اسفنجی ران انسان تحت بارگذاری چرخه‌ای انجام شد و سپس این آزمایش‌ها با شبیه‌سازی المان محدود (FE) با استفاده از هر دو مدل ماده‌ی ICF و SVM تکمیل شدند. هدف شبیه‌سازی‌ها، بازتولید پاسخ استخوان به بارگذاری چرخه‌ای و تعیین مقادیر ریزجابجایی (micromotion) در فصل مشترک استخوان و ایمپلنت در حین فعالیت‌های روزانه بود. در نهایت، کارایی این مدل‌ها در پیش‌بینی ریزجابجایی‌ها بررسی شد.

نمونه‌های استخوانی اسفنجی انسان تحت ۱۰۰ چرخه بارگذاری محوری با جابه‌جایی ۰.۵ میلی‌متر قرار گرفتند و در طی این آزمایش‌ها نیروی واکنش و تغییر شکل دائمی استخوان اندازه‌گیری شد. مقادیر BMD نمونه‌ها از اسکن‌ها استخراج و در مدل‌های FE اختصاصی هر نمونه استفاده شدند. این مدل‌ها بر اساس اسکن‌های QCT از نمونه‌های اسفنجی و استخوان‌های ران اجساد با

سنین ۵۷، ۷۳ و ۹۰ سال ساخته شدند. نمونه‌های استخوانی، بارگذاری چرخه‌ای تک‌محوره و مدل‌های استخوان ران، ریزجایی‌ها را در محل اتصال ایمپلنت و استخوان در حین بارگذاری‌های راه‌رفتن شبیه‌سازی کردند.

نتایج تجربی نشان دادند که انرژی به‌تدریج طی چرخه‌ها تلف می‌شود و نیروی واکنش پس از چند چرخه‌ی ابتدایی در محدوده ۷۰۰ تا ۸۰۰ نیوتن تثبیت می‌گردد. مدل ICF به خوبی این رفتار را بازتولید کرد؛ بیشینه نیروی واکنش به‌دست‌آمده در آزمایش ۱۵۸۰ نیوتن و در مدل ICF برابر با ۱۶۳۰ نیوتن بود و تغییر شکل پلاستیک دائمی نیز به مقدار تجربی (۰.۳ میلی‌متر در آزمایش و ۰.۳۶ میلی‌متر در ICF) نزدیک بود. در مقابل، مدل SVM تغییر شکل پلاستیک اولیه‌ی بسیار شدیدی را نشان داد؛ نیروی واکنش پس از اولین چرخه به ۶۵۰ نیوتن کاهش یافت و میزان جابه‌جایی (۰.۱۱ میلی‌متر) کمتر از مقادیر واقعی بود، که بیانگر برآورد بیش از حد سختی توسط این مدل است.

در شبیه‌سازی FE برای پیش‌بینی ریزجایی‌ها، مدل ICF به‌طور میانگین ریزجایی ۲۷ میکرومتر را پیش‌بینی کرد که در نواحی مختلف اتصال ایمپلنت از ۶ تا ۱۲۷ میکرومتر متغیر بود. در مقابل، مدل SVM مقادیر کمتری (به‌طور میانگین ۱۷ میکرومتر، بازه‌ی ۴ تا ۶۷ میکرومتر) را ارائه داد. هر دو مدل بیشترین ریزجایی را در ناحیه فلنج قدامی (Anterior flange) شناسایی کردند که نشان‌دهنده منطقه‌ای حساس برای پایداری ایمپلنت است. همچنین، مدل ICF کرنش‌های پلاستیک قابل‌توجهی را در اطراف پین‌های ایمپلنت و کندیل‌های قدامی و خلفی پیش‌بینی کرد که با یافته‌های پیشین آزمایشگاهی مطابقت داشت. مدل SVM نیز توزیع مشابهی داشت، اما مناطق پلاستیکی عمیق‌تر و وسیع‌تری را نشان داد.

**مقایسه مدل‌ها:** مدل ICF تطابق بهتری با داده‌های آزمایشگاهی داشت و به‌ویژه در بازتولید افزایش تدریجی نیرو و تغییر شکل‌های پلاستیک موضعی موفق‌تر عمل کرد. در حالی که مطالعات قبلی نشان داده بودند که مدل SVM در مقایسه با داده‌های تجربی ریزجایی را کمتر پیش‌بینی می‌کند، مدل ICF مقادیر بالاتری از ریزجایی را نشان داد. با این حال، برای اعتبارسنجی کامل‌تر مدل ICF، داده‌های تجربی بیشتری نیاز است.

در مجموع، خواص مکانیکی استخوان که توسط مدل‌های رفتاری متفاوت (ICF و SVM) توصیف می‌شوند، می‌توانند به‌طور قابل‌توجهی پیش‌بینی پایداری اولیه ایمپلنت‌های TKA را تحت تأثیر قرار دهند. مدل ICF به دلیل وابستگی به فشار و توانایی شبیه‌سازی دقیق‌تر تغییرشکل پلاستیک استخوان، شبیه‌سازی واقع‌بینانه‌تری ارائه می‌دهد و احتمالاً در پیش‌بینی دقیق‌تر ریزجایی‌ها در سطح تماس استخوان و ایمپلنت برتری دارد. این مطالعه بر اهمیت انتخاب مدل ماده‌ی مناسب برای دستیابی به پیش‌بینی‌های دقیق در شبیه‌سازی‌های بیومکانیکی ایمپلنت زانو تأکید می‌کند.

### پیش‌بینی پایداری بلندمدت تعویض مفصل با استفاده از مدل ICF فصل پنجم

پرسش تحقیقاتی ۴: مدل قوم فشردنی همسانگرد (ICF) چگونه می‌تواند تأثیر خواص مکانیکی استخوان را بر نارسایی بلندمدت

ایمپلنت زانو (TKA) ارزیابی کند؟

در این فصل، مطالعه‌ای توصیف شده است که به بررسی تأثیر کاهش تراکم استخوان پیرامون پروتز (periprosthetic bone loss) بر ریسک نارسایی ایمپلنت تیبیا در TKA می‌پردازد. تمرکز این مطالعه بر تأثیر خواص مکانیکی استخوان بر پایداری طولانی‌مدت ایمپلنت بوده است. برای این منظور، با استفاده از مدل ICF و روش المان محدود (FEA)، تغییرات تراکم معدنی استخوان (BMD) پس از جراحی شبیه‌سازی شد تا تأثیر بازجذب استخوان بر احتمال شکست TKA در درازمدت بررسی شود. مدل‌های FEA بر اساس سی تی اسکن استخوان تیبیا از دو فرد با کیفیت استخوانی متفاوت ایجاد شدند: مردی ۶۵ ساله با کیفیت خوب استخوان و زنی ۹۰ ساله با کیفیت ضعیف استخوان. در این مدل‌ها، مؤلفه تیبیا از نوع Triathlon و یک لایه سیمان استخوانی ۲ میلی‌متری در نظر گرفته شد. شرایط بارگذاری در این مدل‌ها، بارگذاری استاندارد راه‌رفتن و همچنین بارگذاری شدید ناشی از لغزش ناگهانی (stumble) بود، که دومی برای شبیه‌سازی شرایط تروما به کار رفت. خواص مکانیکی استخوان بر اساس داده‌های بالینی BMD طی یک دوره هفت‌ساله پس از جراحی تعیین شد.

در شرایط مکرر راه رفتن، هیچ‌یک از مدل‌های تیبیا دچار شکست نشدند. در مدل استخوان با کیفیت خوب، تغییر شکل پلاستیک پس از ۶۰ چرخه به حالت پایدار رسید، در حالی که برای مدل استخوان با کیفیت ضعیف این حالت پس از ۱۹۰ چرخه رخ داد. در بارگذاری ناشی از لغزش، مدل استخوان با کیفیت ضعیف جابجایی چرخشی قابل‌توجهی نشان داد که از ۳.۷ درجه بلافاصله پس از جراحی به ۱۵.۲ درجه پس از گذشت هفت سال افزایش یافت که بیانگر ریسک بسیار بالای شکست بود. در همین شرایط، مدل استخوان با کیفیت خوب، جابجایی بسیار اندکی (کمتر از ۱ درجه) نشان داد.

حداکثر کرنش‌های پلاستیک بیشتر در بخش داخلی مفصل مشاهده شد. برای استخوان با کیفیت خوب، این کرنش‌ها بلافاصله پس از جراحی حداقل بودند ولی به مرور زمان اندکی افزایش یافتند. در مقابل، استخوان با کیفیت ضعیف از همان ابتدا کرنش پلاستیک زیادی را تجربه کرد که با گذشت زمان و تحلیل بیشتر استخوان تشدید شد.

ارزیابی عددی انجام‌شده به‌وضوح نشان داد که کاهش تراکم استخوان پس از جراحی، ریسک شکست TKA را در استخوان‌هایی با کیفیت ضعیف به‌طور قابل‌توجهی افزایش می‌دهد. این افزایش ریسک به‌ویژه از طریق نشست شدید ایمپلنت تیبیا قابل مشاهده است. نتایج این مطالعه، نقش کلیدی کیفیت استخوان در دوام و طول عمر TKA را برجسته می‌سازد. مدل ICF به‌طور مؤثری

می‌تواند تأثیر خواص مکانیکی استخوان را بر پایداری بلندمدت ایمپلنت پیش‌بینی کند و دیدگاه‌های ارزشمندی را برای برنامه‌ریزی پیش از عمل و مدیریت پس از جراحی فراهم می‌کند تا نتایج بالینی بیمار TKA بهبود یابد.

### نتیجه‌گیری

در این رساله، مدلی برای رفتار ماده استخوان توسعه یافت که مدلسازی بیومکانیکی استخوان را ارتقا داده و به‌ویژه باعث بهبود شبیه‌سازی‌های مربوط به ایمپلنت کامل زانو (TKA) و بررسی مکانیزم‌های فروپاشی استخوان در اطراف این ایمپلنت‌ها می‌شود. با هم‌ترازی مدل فوم فشردنی همسانگرد (ICF) بر اساس خواص مکانیکی منحصربه‌فرد استخوان و داده‌های شکست استخوانی، این مدل توانست رفتار استخوان را با دقت بالایی شبیه‌سازی کرده و پیش‌بینی فروپاشی استخوان را در کاربردهای ارتوپدی بهبود دهد.

### (پرسش تحقیقاتی ۱).

این شبیه‌سازی بهبودیافته، ارزیابی دقیق‌تری از استحکام استخوان و ریسک شکست ارائه می‌کند، چرا که تغییرشکل‌ها و مکانیزم‌های شکست استخوان تحت بارگذاری را با جزئیات بیشتری مدلسازی میکند (پرسش تحقیقاتی ۱). همچنین، خواص مکانیکی استخوان با تأثیر بر مقاومت سطح تماس بین استخوان و ایمپلنت، نقش چشمگیری در پایداری اولیه ایمپلنت‌های TKA ایفا می‌کنند. مدل ICF به دلیل دقت بالایی که در شبیه‌سازی رفتار استخوان دارد، بر پیش‌بینی این پایداری تأثیرگذار بوده و ارزیابی‌های واقع‌گرایانه‌تری از عملکرد ایمپلنت ارائه می‌دهد (پرسش تحقیقاتی ۱).

علاوه بر این، مدل ICF با قابلیت شبیه‌سازی تغییرشکل‌های بزرگ و گسیختگی تدریجی، می‌تواند به‌طور مؤثری تأثیر خواص مکانیکی استخوان را بر موفقیت طولانی‌مدت TKA بررسی کند. این مدل نشان می‌دهد که چگونه تغییرات تراکم و استحکام استخوان در طول زمان می‌توانند منجر به شل‌شدگی یا نارسایی ایمپلنت شوند و به‌این ترتیب، ارزیابی دقیقی از ریسک گسیختگی در درازمدت ارائه می‌کند (پرسش تحقیقاتی ۱).



## Chapter 10

Acknowledgments

PhD portfolio

List of publications

Curriculum Vitae

## Acknowledgments

I am profoundly grateful to God for providing me with strength, guidance, and perseverance throughout my PhD journey.

It is with great gratitude and humility that I reflect on the journey that has led to the completion of this PhD. This achievement is not mine alone; it is the product of continuous support, guidance, and inspiration from numerous individuals, to whom I extend my deepest thanks.

First and foremost, I would like to express my profound appreciation to my promotor, Professor **Nico Verdonshot**. His visionary guidance, encouragement, and unwavering belief in my work made this PhD possible. Professor Verdonshot not only opened the door to this opportunity but also provided the academic environment in which I could thrive. His ability to challenge and support at the same time was instrumental in shaping both my research and my growth as a scientist. I am deeply thankful for his mentorship and the trust he placed in me throughout this journey.

I am equally indebted to my daily supervisor, **Dr. Dennis Janssen**, whose dedication, expertise, and steady support guided me through every stage of this research. Dennis was always available with insightful advice, practical solutions, and a calm, reassuring presence, even during the most stressful times. His ability to translate complex problems into actionable steps, combined with his warm personality, made working with him an exceptional experience. I learned not only how to be a better researcher, but also how to stay resilient and focused, thanks to his mentorship.

I extend my sincere gratitude to the esteemed members of my manuscript committee: **Professor Noël Keijzers**, **Professor Ton van den Boogaard** from Twente University, and **Dr. Bert van Rietbergen** from Eindhoven University of Technology. Their valuable insights, constructive feedback, and rigorous evaluation significantly enhanced the quality of this dissertation. Their expertise and time invested in reviewing my work are deeply appreciated.

I am also profoundly grateful to **Professor Sander Leeuwenburgh**, whose initial support was instrumental in establishing the foundational relationships with my supervisors.

I would also like to extend heartfelt thanks to **Thom Bitter**, who was always there to lend his technical expertise and thoughtful advice. Whether it was troubleshooting simulation issues, setting up training, or simply providing a second opinion, Thom's support was vital to the success of my research. His approachable demeanor and depth of knowledge made him an invaluable resource and a true pillar of the team.

Special thanks to **Richard van Swam**, the brilliant engineer and the soul of our biomechanical laboratory. With his unique combination of technical precision and medical insight, he played a pivotal role in making the experimental aspects of my work feasible. His enthusiasm for innovation and hands-on problem-solving created an environment where science met creativity.

I would also like to thank **Max Bakker**, our MATLAB maestro, who turned complex analyses into enjoyable, almost artistic challenges. His coding support and sharp insights made the analytical parts of my research not only possible but enjoyable.

I am grateful to my friends and colleague **Ali Ataei** and **Fazael**, who stood by me as both a fellow researcher and a true friend. Their companionship went beyond academic collaboration—we shared unforgettable moments of joy, from volleyball games to singing sessions, from focused research discussions to laughter-filled evenings. Their support, both emotionally and intellectually, left a lasting impression on my PhD years.

My sincere thanks go to my friend and colleague **Esther Sanchez**, who was always there during tough simulation problems, offering both technical help and emotional support. Our shared conversations, laughter, and friendship were a source of strength and motivation throughout the years.

I also wish to acknowledge **Corine Post**, **Martijn Kuijpers**, **Thomas Gersie**, **Hans Dunning** and **Thomas Anijs**, with whom I shared the highs and lows of academic life. The discussions we had, the ideas we exchanged, and the mutual support we provided one another helped us all grow as researchers.

Heartfelt thanks to **Erwin Haukes** for his warm discussions and engaging conversations about life in the Netherlands. Our interactions during free moments in the lab enriched my understanding of Dutch culture and made my time here more enjoyable.



A special thank-you to all staffs of Othopeadic Research Lab (**ORL**), the master's students and medical interns I had the privilege to work with. Their efforts, insights, and engagement contributed not only to the success of this dissertation but also to my development as an independent, yet collaborative, scientist. Their enthusiasm was contagious, and their curiosity reminded me daily of the joy of discovery and learning.

Beyond academia, I am grateful to our best friends **Abbas and Sana** and their beloved son, **Mohammad Hasan** whose companionship enriched the time my family and I spent in the Netherlands. Their presence brought warmth and joy into our lives and made our time abroad even more memorable and meaningful.

I would also like to extend my heartfelt gratitude to my dear friends, **Sayed Ebrahim and Peyman**, along with their families. Their friendship and support made our life in the Netherlands more enjoyable and fulfilling. The moments we shared together, both in academic settings and during our leisure time, added a richness to our experience that I will always cherish.

A very special thanks to the **Rezaei family**—Siamak, Mehri, Anahita, and Pouya. Although we met later in our journey, it felt as though we had known them forever. Their kindness, generosity, and warmth made us feel truly at home. They supported us like family, shared joyful and meaningful moments with us, and brought a deep sense of belonging that enriched our time in the Netherlands immeasurably. I am deeply grateful for their presence in our lives.

Most importantly where words cannot truly capture the gratitude I feel for my beloved wife, **Somayeh**. She has been by my side every step of this long journey—not only as my life partner but also as a fellow researcher and academic companion. From our early days of studying together during our bachelor and master's degrees, to late nights conducting experiments during our PhDs, she has been my rock, my support, and my inspiration. Her love, resilience, and sacrifices have been the foundation of every success I have achieved. Without her, none of this would have been possible. Also, to the most beautiful gift of all—our daughter **Mahrokh**, who came into our lives near the end of this PhD journey and filled it with even more purpose, joy, and motivation. Her smile reminded me each day of the greater future ahead and inspired me to persevere, even in the toughest moments. Her presence colored my life and gave me the strength to write that one more paper, one more line, one more idea.

در پایان، بر خود واجب می‌دانم که از خانواده‌ام با تمام وجود قدردانی کنم؛ خانواده‌ای که پشتوانه تمام لحظات سخت و شیرین این مسیر بوده‌اند:

**پدر و مادر عزیزم**، که هر آن‌چه هستم از برکت وجود و تربیت آن‌هاست؛ کسانی که با عشق بی‌کران، ایمان استوار، و دعای همیشگی‌شان، نیروی حرکت من بودند. حتی زمانی که هزاران کیلومتر دور از آن‌ها بودم، قلبشان همیشه در کنارم می‌تپید و حضور روحی‌شان لحظه‌ای مرا تنها نگذاشت. از دوران کودکی، آن‌ها نه تنها حامی من در مسیر علم بودند بلکه با تشویق‌های مداومشان رؤیای گرفتن مدرک دکتری را در من زنده نگه داشتند. این موفقیت، بازتابی از آرزوهای آن‌ها و تلاش‌های بی‌وقفه‌شان است. دست بوس همیشگی شما خواهم بود عزیزان من.

از **خواهر عزیزم ندا** و همسر گران‌قدرش **علی جان** نیز صمیمانه سپاسگزارم. حضور پرمحبت و حمایت بی‌دریغ آن‌ها، به‌ویژه در دوران‌های سخت، پشتوانه بزرگی برای من بود. پسر نازنین‌شان، **کیان‌جون**، که هم‌زمان با مراحل رشد پایان‌نامه‌ام بزرگ شد، با لبخندها و انرژی کودکانه‌اش، نور امید را در روزهای خستگی به زندگی‌مان بخشید. آرزو دارم شاهد تک‌تک روزهای موفقیت و پیشرفت او باشم.

سپاس و قدردانی ویژه از **پدر و مادر همسر** که با مهربانی، درک بالا، و حمایت‌های صمیمانه‌شان، فضای امن و دلگرم‌کننده‌ای برای ادامه راه ما فراهم کردند. همچنین، از خانواده برادر همسر، **حمید و عاطفه عزیز**، که همیشه با ما بوده‌اند و حضورشان موجب دلگرمی ما بوده است، صمیمانه تشکر می‌کنم. اکنون با آمدن دختر زیبایشان، **آیسان**، زندگی ما رنگ تازه‌ای یافته و او همراهی خواهد بود برای دختر کوچک ما، ماه‌رخ، تا در کنار هم دنیایی پر از شادی و دوستی بسازند.

همچنین بر خود لازم می‌دانم که از **عموی بزرگوارم، جمشید**، صمیمانه تشکر کنم؛ کسی که در مسیر پذیرش برای دوره دکتری و فراهم کردن شرایط ورود به کشور هلند، با دلسوزی، وقت و سرمایه خود را در اختیار من قرار داد.

# PhD portfolio of Navid Soltani Hafshejani

**Department:** Orthopaedic Research Lab  
**PhD period:** 16/10/2018 – 16/10/2024  
**PhD Supervisor(s):** Prof. Dr. ir. N. Verdonshot  
**PhD Co-supervisor(s):** Dr. ir. D. Janssen

Training activities	Hours	EC points
<b>Courses</b>		
• Radboudumc - Introduction day (2019)	6.00	0.3
• RIHS - Introduction course for PhD candidates (2019)	15.00	0.6
• Statistics with JASP for PhD candidate (2019)	24.00	0.9
• Scientific writing for PhD candidates (2019)	84.00	3
• How to sell your science (2019)	8.00	0.3
• RU - University Teaching Qualification - Hoor- en responsiecolleges: activeren en reflecteren (2020)	28.00	1
• Data Analytics with MATLAB (2020)	2.00	0.1
• RU - Statistics for PhD's by using SPSS (2020)	60.00	2.2
• Digital Tools in educational progress (2020)	4.00	0.3
• Radboudumc - Scientific integrity (2024)	20.00	0.8
<b>Seminars</b>		
• Workshop on finite element simulation in Hypermesh (2019)	7.00	0.3
• Workshop on "Literature review: how to search & where to publish (2019)	4.00	0.3
• Workshop on Writing a Rebuttal (2021)	1.00	0.1
• Orthopaedic research laboratory FEA meetings (2022)	30.00	1.1
• Spiegeluur ORL on advances in science (2022)	78.00	2.8
• Orthopaedic research laboratory scientific meetings (2022)	175.00	6.3
• PhD Retreat (2023)	24.00	0.9
• Research Integrity Round (2024)	1.75	0.1
• Research Integrity Round (2024)	1.75	0.1
<b>Conferences</b>		
• ISTA New Early-career Webinar Series (2020)- Oral Presentation	24.00	0.9
• 27th National and 5th International Iranian Conference on Biomedical Engineering (ICBME) (2020) - Oral Presentation	24.00	0.9
• ORS Annual Meeting (2021)- Poster Presentation	16.00	0.6
• ORS Annual conference 2022 (2022)- Poster Presentation	24.00	0.9
• ORS Annual conference 2022 (2022)- Poster Presentation	8.00	0.3
• ORS Annual conference 2022 (2022)- Oral Presentation	8.00	0.3
• Annual progress of the International Society for Technology in Arthroplasty (ISTA) (2022)- Oral Presentation	24	0.9
• Annual progress of the International Society for Technology in Arthroplasty (ISTA) (2022)- Oral Presentation	8	0.3

Training activities	Hours	EC points
<b>Lecturing</b>		
• Finite element Analysis in biomechanics (2019)	16.00	0.6
• Coaching a student internship of 12 weeks (2021)	30.00	1.1
<b>Supervision of internships / other</b>		
• Supervision of Master Student (2020) - MSc Thesis- S. Stocco, Total Knee Fixation: Rhine-Waal University of Applied Sciences-Radboudumc.	65.00	2.4
• Supervision of Master Student (2021) - MSc Thesis- B. Ranjkesh, Design and Fabrication of leg motion simulator: Shahrood University Of Technology	96.00	3.5
• 3rd year Medical Student, Research Group 60-T. Bonekamp (2021)	7.5	0.3
• 3rd year Medical Student, Research Group 60-T. Breeuwsma (2021)	7.5	0.3
• 3rd year Medical Student, Research Group 60-P. Colen (2021)	7.5	0.3
• 3rd year Medical Student, Research Group 60-S. Kokabi (2021)	7.5	0.3
• 3rd year Medical Student, Research Group 60-J. Van Den Ven (2021)	7.5	0.3
• 3rd year Medical Student, Research Group 60-T. Van Garderen (2021)	7.5	0.3
• Supervision of Master Student (2021)- -MSc Thesis- S. Toniutti, Mechanical behavior of human femoral bone: Polytechnic University of Milan- Radboudumc	52	1.9
• Supervision of Master Student (2021)- -MSc Thesis- F. Perroni, Mechanical behavior of human femoral bone: Polytechnic University of Milan-Radboudumc	52	1.9
<b>Total</b>	<b>1,065.50</b>	<b>38.1</b>

## List of publications during PhD

### Refereed journal papers

1. **N. Soltanihafshejani**, T. Bitter, D. Janssen, and N. Verdonschot, "Development of a crushable foam model for human trabecular bone," *Medical Engineering & Physics*, vol. 96, pp. 53-63, 2021.
2. **Soltanihafshejani N**, Peroni F, Toniutti S, Bitter T, Tanck E, Eggermont F, Verdonschot N, Janssen D. The application of an isotropic crushable foam model to predict the femoral fracture risk. *PLoS One*. 2023 Jul 27;18(7):e0288776.
3. **Soltanihafshejani N**, Bitter T, Verdonschot N, Janssen D. The effect of periprosthetic bone loss on the failure risk of tibial total knee arthroplasty. *Journal of Orthopaedic Research®*. 2024 Jan;42(1):90-9.
4. **Soltanihafshejani N**, Bitter T, Verdonschot N, Janssen D. The Effect of Bone Plasticity Models on Simulations of Primary Fixation in Total Knee Arthroplasty. *Medical Engineering & Physics*. 2025 Mar 9:104329.

### Conference Presentations with Refereed Published Abstracts

1. **N. Soltanihafshejani**, T. Bitter, D. Janssen, and N. Verdonschot, "Experimental and Numerical Identification of Crushable Foam Model of Human Trabecular Bone," in *Orthopaedic Proceedings (ISTA Meetings)*, 2021, vol. 103, no. SUPP\_1: The British Editorial Society of Bone & Joint Surgery, pp. 9-9.
2. **N. Soltani**, Z. Rezasoltani and N. Jamshidi, "The Effect of Stem on The Knee Joint Prosthesis Flexion Considering Natural Gait Forces," *2020 27th National and 5th International Iranian Conference on Biomedical Engineering (ICBME)*, 2020, pp. 173-176, doi: 10.1109/ICBME51989.2020.9319430.

### Refereed Papers in Conference Proceedings with oral presentation and poster

1. **Soltanihafshejani N**, Bitter T, Janssen D, Verdonschot N. Experimental and Numerical Identification of Crushable Foam Model of Human Trabecular Bone. In *Orthopaedic Research Society, ORS Annual meeting*, February 12-16, 2021.
2. **Soltanihafshejani N**, Bitter T, Janssen D, Verdonschot N, Femoral Fracture Risk Prediction Using A Crushable Foam Material Model, *Orthopaedic Research Society (ORS)2022*, Tempa, Florida, February 2022.
3. Stoco S, **Soltanihafshejani N**, Janssen D Design Comparison Of Implants For Revision Total Knee Arthroplasty: A Finite Element Analysis, *Orthopaedic Research Society (ORS)2022*, Tempa, Florida, February 2022.

4. **Soltanihafshejani, N.**, Peroni, F., Toniutti, S., Bitter, T., Verdonschot, N., Janssen, D. Characterization Of A Crushable Foam Model For Human Distal Femur And Application For Total Knee Arthroplasty, Orthopaedic Research Society (ORS)2022, Tempa, Florida, February 2022.
5. **Soltanihafshejani N**, Bitter T, Janssen D, Verdonschot N., "The Effect of Periprosthetic Bone Loss on the Failure Risk of Tibial Total Knee Arthroplasty", Annual progress of the International Society for Technology in Arthroplasty (ISTA), Annual Congress Maui, 30 Agus -03 Sep 2022.
6. **Soltanihafshejani N**, Bitter T, Janssen D, Verdonschot N., "The Influence of Plasticity Models on the Micromotion Predictions in Total Knee Arthroplasty", Annual progress of the International Society for Technology in Arthroplasty (ISTA), Annual Congress Maui, 30 Agus -03 Sep 2022.

#### **Journal Papers in Preparation**

1. **Soltanihafshejani N**, Grijs T, Janssen D, Verdonschot N, "Initial stability of Tibial Tray Implant: A validation study of Crushable foam model".

## Curriculum Vitae



**Navid Soltani** was born in Iran and pursued his academic studies in Biomedical Engineering, beginning with a B.Sc. in Biomechanical Engineering from Isfahan University in 2013. He then completed his M.Sc. in Biomedical Engineering at Amirkabir University of Technology in Tehran, specializing in orthopedic and dental biomechanics. His research during this time focused on the finite element analysis of disc implants.

Between 2015 and 2018, following his master's degree, Navid gained valuable professional experience in the orthopedic medical device industry in Iran. He worked as a technical supervisor and R&D consultant in trauma and spinal implant manufacturing companies, contributing to product design, regulatory documentation, and quality assurance processes. During this period, he was also appointed as an external consultant for the Iranian Ministry of Health's National Medical Device Directorate, where he evaluated technical files and audited orthopedic device manufacturers.

In 2018, Navid commenced his Ph.D. studies at the Orthopaedic Research Laboratory, Radboud University Medical Center (Radboudumc), Nijmegen, the Netherlands. Under the supervision of Prof. dr. Nico Verdonschot and dr. Dennis Janssen, his research focused on the failure mechanisms of total knee replacements using both experimental methods and numerical simulations. His thesis involved developing a crushable foam model for trabecular bone and validating micromotion predictions through biomechanical experiments.

In addition to his doctoral research, Navid was actively involved in collaborative projects with master and medical students, contributing to the scientific community through multiple journal articles, conference presentations, and book publications.

Following the completion of his Ph.D. research in 2022, Navid continued working as a postdoctoral researcher at Radboudumc, focusing on computational modeling in orthopedics. In parallel, he has been serving as a Medical Device Lead Auditor at a Notified Body in Europe, combining his academic expertise with regulatory responsibilities in medical device compliance.

Navid's broad expertise spans orthopedic biomechanics, medical device design and regulation, and computational modeling. His passion for translational research and healthcare innovation continues to drive his career both in academia and industry.



